The Dissertation Committee for Peter Ojo Olapade Certifies that this is the approved version of the following dissertation:

Simulation, Analysis, and Mass-Transport Optimization in PEMFCs

Committee:

Jeremy P. Meyers, Supervisor

Arumugam Manthiram

Thomas F. Edgar

Carlos H. Hidrovo

Dongmei Chen

Simulation, Analysis, and Mass-Transport Optimization in PEMFCs

by

Peter Ojo Olapade, B.Sc.; M.Sc.

Dissertation

Presented to the Faculty of the Graduate School of

The University of Texas at Austin

in Partial Fulfillment

of the Requirements

for the Degree of

Doctor of Philosophy

The University of Texas at Austin

December 2011

Dedication

This dissertation is dedicated to God Almighty for seeing me through the toughest period in the PhD program. He is always there for me.

Acknowledgements

My deepest appreciation goes to my advisor Dr. Jeremy Meyers. It is really a great opportunity for me to have him as my dissertation advisor. I am very grateful for his patience, support and encouragement. I am also thankful for his valuable advice on career planning. I also want to thank all my committee members for their helpful suggestions. I want to thank my colleagues: Preethi Matthew, Katherine Harrison, Seok Koo Kim, Kevin O'Neil, Babar Koraishy, Brent Bennett, Joshua Garvin, David McCleary and Robert Fares for their valuable input. I will also like to thank Dr. Rodney L. Borup, Dr. Rangachary Mukundan, Dr. Dusan Spernjak and Dr. Joseph Fairweather for their guidance and useful suggestions while at Los Alamos National Laboratory. They made my internship at Los Alamos National Laboratory a productive and a memorable one.

I cannot but appreciate the support of my entire family. They all stood by me throughout the entire program. I want to thank my wife, Yewande Olapade who has always stood me during challenging times and also my daughter, Oluwaseun Olapade for knowing when to pull me from computer to have some fresh air. She is truly amazing. I also want to thank my brother, Folu Olapade, who has been like a father to me. I am really honored to have him as brother. My appreciation will be incomplete without mentioning my parents: my dad who has always been the source of inspiration to me, and my mother, who is like a pillar of our family. We are all where we are today because of their sacrifices.

I would like to thank my friends, above all Dr. Rotimi Ojifinni, Dr. Femi Job, Michael Asoro, Tosin Asoro, Abiola Oladapo, Ayoade Oladapo, Affiong Eyo, Gbenga Alabi, Ola Owoputi, Femi Ogunyomi, Bode Ijasan, Dr. Chimaobi Onwuchekwa, Azom

Prince and Dr. Saheed Aderinto for their moral support and also for making my program here in UT-Austin enjoyable.

Finally, I want to thank God Almighty, the source of all good things, for giving me wisdom and strength to successfully complete the PhD program.

Simulation, Analysis, and Mass-Transport Optimization in PEMFCs

Peter Ojo Olapade, PhD

The University of Texas at Austin, 2011

Supervisor: Jeremy P. Meyers

In this dissertation, we present two major lines of numerical investigation based on a control-volume approach to solve coupled, nonlinear differential equations. The first model is developed to provide better understanding of the water management in PEMFC operating at less than 100ºC, under transient conditions. The model provides explanations for the observed differences between hydration and dehydration time constants during load change. When there is liquid water at the cathode catalyst layer, the time constant of the water content in the membrane is closely tied to that of liquid water saturation in the cathode catalyst layer, as the vapor is already saturated. The water content in the membrane will not reach steady state as long as the liquid water flow in the cathode catalyst layer is not at steady state.

The second model is to optimize the morphological properties of HT-PEMFCs components so as to keep water generated as close as possible to the membrane to help reduce ionic resistance and thereby increase cell performance. Humidification of the feed gas at room temperature is shown to have minimal effects on the ionic resistance of the membrane used in the HT-PEMFC. Feed gases must be humidified at higher temperature to have effects on the ionic resistance. However, humidification at such higher temperatures will require complex system design and additional power consumption. It is, therefore, important to keep the water generated by the electrochemical reaction as

close as possible to the membrane to hydration the membrane so as to reduce the ionic resistance and thereby increase cell performance.

The use of cathode MPL helps keep the water generated close to the membrane and decreasing the MPL porosity and pore size will increase the effectiveness of the MPL in keep the water generated close to the membrane. The optimum value of the MPL porosity depends on the operating conditions of the cell. Similarly, decreasing the GDL porosity helps keep water close to the membrane and the optimum value of the GDL porosity depends on the operating conditions of the cell.

Table of Contents

List of Tables xii

List of Figures xiii

Chapter 1: Introduction 1

1.1 Background 1

1.1.1 Brief History and Major Breakthroughs in PEMFCs 2

1.1.2 Potential Applications and Current Challenges in PEMFCs 4

1.2 PEMFC Basics 7

1.2.1 Proton-Exchange Membrane 7

1.2.2 Catalyst Layer 9

1.2.3 Gas Diffusion Medium 9

1.2.4 Bipolar Plates 10

1.3 PEMFC Performance 10

1.4 Thermodynamics 12

1.5 Kinetics 13

1.6 Literature Review 15

1.6.1 Water Transport in the Low-Temperature PEMFC 15

1.6.2 Effects of MPL on the Transient Response of Low-Temperature PEMFC 18

1.6.3 Optimization of High-Temperature PEMFC 20

1.7 Scope of Research and Objective 22

Chapter 2: Model Development 23

2.1 Governing Equations for the Transient Response of Proton-Exchange Membrane Fuel Cell Subjected to Load Change 23

2.1.1 Transport of electric charges 24

2.1.2 Transport of water in membrane phase 26

2.1.3 Transport of gas species 29

2.1.4 Transport of liquid water 31

2.1.5 Boundary Conditions 36

2.2 Model Development for the Effects of MPL on Transient Response of PEMFC to Load Change 37
2.2.1 Transport of gas species 38
2.2.2 The boundary conditions 39
2.3 Model Development for Parametric Study of the Morphological Proprieties of HT-PEMFC Components for Effective Membrane Hydration 40
2.3.1 Transport of electric charges 41
2.3.2 Transport of gas species 42
2.3.3 Transport of Energy 44
2.3.4 Transport of Electric Charge 45
2.3.5 Boundary Conditions 50
2.6 Numerical Implementation 51

Chapter 3: Result and Discussions Part 1: Modeling Transient Response of Proton-Exchange Membrane Fuel Cell under Load Change 54
3.1 The Effects of Different CL Capillary Pressure 67
3.2 The Effects of Different Load Changes 70
3.3 The effects of different saturation at gas channel and cathode GDL interface 73
3.4 The Effects of Cathode Side Relative Humidity 75
3.5 Conclusion 79

Chapter 4: Result and Discussions Part II: the Effects of MPL on the Transient Response of PEMFC under load change 81
4.1 Effects of MPL Absolute Permeability 87
4.2 Effects of MPL capillary pressure 89
4.3 Conclusion 92

Chapter 5: Results and Discussions Part III: Optimization of the Morphological Proprieties of HT-PEMFC Components for Effective Membrane Hydration 93
5.1 Inlet Relative Humidity 94
5.2 Effects of Including MPL 96
5.3 Effects of MPL pore sizes 99
5.4 Effects of MPL Porosity 101

5.5 Effects of GDL porosity.....104
5.6 Effects of Mass-Transport in the Agglomerate of the CL on the Optimization of HT-PEMFC for Effective Membrane Hydration 108
5.7 Conclusion.....111
Chapter 6: Summary and Future Works.....113
Appendix.....116
Appendix A: Polynomials Fitted to the Experimentally Measured Capillary Pressure of Compressed Toray 120C.....116
Appendix B: Nomenclatures Used in the Dissertation.....117
References.....123

List of Tables

Table I: Electrochemical and physical relationships..... 35

Table II: Parameters used in the model 36

Table III: Summary of boundary conditions. 37

Table IV: Parameters used in the model 39

Table V: Summary of boundary conditions 40

Table VI: Electrochemical and physical relationships..... 49

Table VII: Parameters used in the model 50

Table VIII: Summary of the boundary conditions 51

List of Figures

Figure 1.1: Schematic Diagram of Proton-Exchange Membrane Fuel Cell. 3

Figure 1.2: Typical Polarization Curve for PEMFC..... 11

Figure 1.3: Phase Equilibrium Representation of PEMFCs..... 13

Figure 2.1. Capillary pressures of compressed Toray 120C..... 34

Figure 2.2: Schematic diagram illustrating the numerical implementation..... 52

Figure 3.1: Current density in Nafion® 112, 115 117 for step change in voltage (T = $80\,^{o}C$, P = 1bar, RH_a/RH_c = 100%/100%, 0.5V to 0.8V from t = 0 to 800s and 0.8V to 0.5V from 800s to 1600s)..... 54

Figure 3.2: The effect of the hysteresis observed in the capillary pressure-saturation relation (a) ionic resistance in the bulk membrane during step change in voltage, (b) water content at aCL/membrane interface during step change in voltage, (c) water content at membrane/cCL interface during step change in voltage, (d) liquid water saturation at membrane/cCL interface during step change in voltage. (T = $80\,^{o}C$, P = 1bar, RH_a/RH_c = 100%/100%, 0.5V to 0.8V from t = 0 to 800s and 0.8V to 0.5V from 800s to 1600s, Nafion® 112)..... 56

Figure 3.3: MEA High-Frequency Resistance (18 μm thick GORE-SELECT® membrane, aCL/cCL thickness = 4.5μm/9μm, GDL thickness = 200μm macro-GDL and 50μm MPL, T = $80\,^{\circ}$C). 57

Figure 3.4: The plot of water content of Nafion® 112 for when voltage is stepped up from 0.5V to 0.8V and vice versa (T = $80\,^{o}C$, P = 1bar, RHa/RHc = 100%/100%). 59

Figure 3.5: The plot of water content of Nafion® 112 for when voltage is stepped up from 0.5V to 0.8V and vice versa (T = 80 ^{o}C, P = 1bar, RH_a/RH_c = 100%/100%). 60

Figure 3.6: Comparison of ionic resistance, water content and saturation for Nafion® 112, 115 and 117 (a) ionic resistance in the bulk membrane during step change in voltage, (b) water content at aCL/membrane interface during step change in voltage, (c) water content at cCL/cGDL interface during step change in voltage, (d) liquid water saturation at membrane/cCL interface during step change in voltage (T = 80 ^{o}C, P = 1bar, RH_a/RH_c = 100%/100%, 0.5V to 0.8V from t = 0 to 800s and 0.8V to 0.5V from 800s to 1600s). 62

Figure 3.7: Comparison of various water phases at membrane interface (T = 80 ^{o}C, P = 1bar, RH_a/RH_c = 100%/100%, 0.5V to 0.8V from t = 0 to 800s and 0.8V to 0.5V from 800s to 1600s, Nafion® 112). 66

Figure 3.8: Comparison of ionic resistance, water content and saturation for different CL capillary pressure (a) ionic resistance in the bulk membrane during step change in voltage, (b) water content at aCL/membrane interface during step change in voltage, (c) water content at membrane/cCL interface during step change in voltage, (d) liquid water saturation at membrane/cCL interface during step change in voltage. (T = 80 ^{o}C, P = 1bar, RH_a/RH_c = 100%/100%, 0.5V to 0.8V from t = 0 to 800s and 0.8V to 0.5V from 800s to 1600s, Nafion® 112). 68

Figure 3.9: Current density profiles for different CL capillary pressure during step change in voltage. (T = 80 ^{o}C, P = 1bar, RH_a/RH_c = 100%/100%, 0.5V to 0.8V from t = 0 to 800s and 0.8V to 0.5V from 800s to 1600s).. 69

Figure 3.10: The effects of different load changes (a) ionic resistance in the bulk membrane during step change in voltage, (b) water content at aCL/membrane interface during step change in voltage, (c) water content at membrane/cCL interface during step change in voltage, (d) liquid water saturation at membrane/cCL interface during step change in voltage. (T = $80^{o}C$, P = 1bar, RH_a/RH_c = 100%/100%, Nafion® 112). 71

Figure 3.11: Current density profiles for different load changes (T = $80^{o}C$, P = 1bar, RH_a/RH_c = 100%/100%, Nafion® 112). 72

Figure 3.12: The effect of different value of saturation at cGDL/cGC interface (a) ionic resistance in the bulk membrane during step change in voltage, (b) water content at aCL/membrane interface during step change in voltage, (c) water content at membrane/cCL interface during step change in voltage, (d) liquid water saturation at membrane/cCL interface during step change in voltage. (T = 80ºC, P = 1bar, RH_a/RH_c = 100%/100%, 0.5V to 0.8V from t = 0 to 800s and 0.8V to 0.5V from 800s to 1600s, Nafion® 112). 74

Figure 3.13: Current density profiles for different saturation at gas channel and cathode GDL interface during step change in voltage. (T = 80ºC, P = 1bar, RH_a/RH_c = 100%/100%, 0.5V to 0.8V from t = 0 to 800s and 0.8V to 0.5V from 800s to 1600s, Nafion® 112)..... 75

Figure 3.14: The effects of different cathode side relative humidity (T = $80^{o}C$, P = 1bar, RH_a = 100%, 0.5V to 0.8V from t = 0 to 800s and 0.8V to 0.5V from 800s to 1600s, Nafion® 112). 76

Figure 3.15: Current density profiles for different cathode side relative humidity during step change in voltage. (T = $80^{o}C$, P=1bar, RH_a = 100%, 0.5V to 0.8V from t = 0 to 800s and 0.8V to 0.5V from 800s to 1600s, Nafion® 112). 78

Figure 4.1: Experimentally measured capillary pressure of compressed Toray 120C, CL capillary pressure and based case MPL capillary pressure. 81

Figure 4.2: The plot of ionic resistance and the current density in the bulk membrane for when there is cMPL and no MPL is used (Nafion 112 membrane, T = 80 °C, P = 1bar, RH_a/RH_c = 100%/100%, 0.5V to 0.8V from t = 0 to 1000s and 0.8V to 0.5V from 1000s to 2000s). 82

Figure 4.3: The plot of water content at anode side and cathode side membrane interfaces and liquid water saturation at cathode side membrane and cGDL interfaces for when cMPL is used and when no MPL is used (Nafion 112 membrane, T = 80 °C, P = 1bar, RH_a/RH_c = 100%/100%, 0.5V to 0.8V from t = 0 to 1000s and 0.8V to 0.5V from 1000s to 2000s). 83

Figure 4.4: The plot of ionic resistance, water content and saturation at the cathode side of the membrane and the saturation at the interface between the cMPL and the cGDL for cases with different MPL absolute permeabillity (Nafion 112 membrane, T = 80 °C, P = 1bar, RH_a/RH_c = 100%/100%, 0.5V to 0.8V from t = 0 to 1000s and 0.8V to 0.5V from 1000s to 2000s). 88

Figure 4.5: The plot of ionic resistance, water content and saturation at the cathode side of the membrane and the saturation at the interface between the cMPL and the cGDL for cases with different MPL capillary pressure (Nafion 112 membrane, T = 80 °C, P = 1bar, RH_a/RH_c = 100%/100%, 0.5V to 0.8V from t = 0 to 1000s and 0.8V to 0.5V from 1000s to 2000s). 90

Figure 5.1: Comparison between the model prediction and experimental data[100] (operating temperature is 150℃, cell operates with hydrogen and air at 0.38% relative humidity and operating pressure of 1atm, acid doping level is 5.6). 93

Figure 5.2: Effects of relative humidity on current density and the ionic resistance in the membrane (operating temperature is 190℃, the cell operates with hydrogen and oxygen 2 bar with an acid doping level of 6). 95

Figure 5.3: The plot of ionic resistance in the cell with and without MPL (operating temperature is 190℃, the cell operates with hydrogen and oxygen at 3.8% relative humidity and operating pressure of 2 bar, acid doping level of 6)..... 97

Figure 5.4: The plot of water vapor partial pressure in a cell with and without MPL (a) vapor pressure at aCL/membrane interface, (b) vapor pressure at membrane/cCL interface. (Operating temperature is 190℃, the cell operates with hydrogen and oxygen at 3.8% relative humidity and operating pressure of 2 bar, acid doping level of 6)..... 98

Figure 5.5: The plot of ionic resistance for cells with different MPL pore radius (operating temperature is 190℃, the cell operates with hydrogen and oxygen at 3.8% relative humidity and operating pressure of 2bar, acid doping level of 6). 100
101

Figure 5.6: The plot of water vapor partial pressure for cells with different MPL pore radius (a) vapor pressure at aCL/membrane interface, (b) vapor pressure at membrane/cCL interface. (Operating temperature is 190℃, the cell operates with hydrogen and oxygen at 3.8% relative humidity and operating pressure of 2bar, an acid doping level of 6). 101

Figure 5.7: The plot of ionic resistance for cells with different MPL porosity (operating temperature is 190℃, the cell operates with hydrogen and oxygen at 3.8% relative humidity and 2 bar and acid doping level of 6). 102

Figure 5.8: The plot partial vapor pressure for cells with different MPL porosity (a) vapor pressure at aCL/membrane interface, (b) vapor pressure at membrane/cCL interface. (operating temperature is 190℃, the cell operates with hydrogen and oxygen at 3.8% relative humidity and operating pressure of 2bar, an acid doping level of 6). 103

Figure 5.9: The plot of current density for varying MPL porosity at different operating pressure (operating temperature is 190℃, the cell operates with hydrogen and oxygen at 3.8% relative humidity and acid doping level of 6).....104

Figure 5.10: The plot of ionic resistance for cells with different GDL porosity (operating temperature is 190℃, the cell operates with hydrogen and oxygen at 3.8% relative humidity and operating pressure of 2bar, an acid doping level of 6).....105
Figure 5.11: The plot partial vapor pressure for cells with different GDL porosity (a) vapor pressure at aCL/membrane interface, (b) vapor pressure at membrane/cCL interface. (operating temperature is 190℃, the cell operates with hydrogen and oxygen at 3.8% relative humidity and operating pressure of 2bar, an acid doping level of 6).....106
Figure 5.12: The plot of current density for varying GDL porosity at different operating pressure (operating temperature is 190℃, the cell operates with hydrogen and oxygen at 3.8% relative humidity, an acid doping level of 6).....107
Figure 5.13: The plot of current density for cases with agglomerate and that without agglomerate for various MPL and GDL porosity (operating temperature is 190℃, the cell operates with hydrogen and oxygen at 3.8% relative humidity and operating pressure of 2bar, an acid doping level of 6).109
Figure 5.14: The plot of current density when agglomerate model is used for two different total gas pressure and varying GDL porosity (operating temperature is 190℃, the cell operates with hydrogen and oxygen at 3.8% relative humidity, acid doping level of 6). 110

Chapter 1: Introduction

1.1 BACKGROUND

US oil production peaked around 1970s at about nine million barrels per day, and it has since been declining steady. Today, the US extracts about six million barrels of oil daily [1]. Similarly, the production of petroleum and natural gas worldwide is expected to peak between 2015 and 2020, and then begin to decrease [2]. At the moment, about 80% of the world energy demand is met by fossil fuels, which face inevitable decline in production, but at the same time, worldwide energy demand is on the rise, because of the increasing energy demand of the developing nations such as India and China. The world, therefore, faces the prospect of economic disruption that would be caused by such a projected gap in oil production and consumption. In addition to the decline in oil production, fossil fuels are known to cause serious environmental problems like global warming, depletion of ozone layer, oil spills, melting of ice caps and rising sea levels [2]. The prospect of the decline in worldwide oil production, ever-increasing energy demand, and the serious environmental problems caused by fossil fuels are pushing the demands for energy sources that are environmental friendly. One technology that has shown great promise as a possible power source for automobile, residential, and battery replacement applications is proton exchange membrane fuel cells (PEMFCs) [3]. The PEMFC is an environmental friendly, highly efficient energy conversion device that produces electricity, plus heat and water as by-products. If hydrogen is used as fuel, PEMFCs produce no pollutant emission; if the hydrogen comes from renewable energy sources, the electrical power produced can be truly sustainable [4].

1.1.1 Brief History and Major Breakthroughs in PEMFCs

The fuel cell was first demonstrated by Sir William Grove in 1839 [5]. However, Grove's first fuel cell was not practical, due to the corrosion of the electrodes, instability of the materials, and very low power densities [4]. Grove's apparatus consisted of separate vessels containing electrodes immersed in sulfuric acid solution, but the fuel cell has evolved since that time to resemble a more standard cell configuration. A schematic diagram of a typical fuel cell with acid-based electrolyte is shown in Figure 1.1. In an operating fuel cell, the fuel (either hydrogen or reformate) is supplied to the anode gas channel where it travels through the gas-diffusion layer (GDL) to the catalyst layer where it is oxidized to hydrogen ion. The hydrogen ion moves through the proton-exchange membrane while the electron goes through the external circuit in form of electric current. The anode reaction is

$$2H_2 \rightarrow 4H^+ + 4e^- \tag{1.1}$$

On the cathode side, oxidant (oxygen or air) is supplied to the cathode gas channel, where is travels through the GDL to the cathode catalyst layer. At the cathode catalyst layer, oxygen is reduced according to the following reaction

$$4H^+ + 4e^- + O_2 \rightarrow 2H_2O \tag{1.2}$$

Water in form of either vapor or liquid is produced as the by-product in addition to heat. The overall reaction in the PEMFC, given by the addition of equation 1.1 and 1.2, is as follows

$$2H_2 + O_2 \rightarrow 2H_2O \tag{1.3}$$

More technical detail about the materials of construction and the processes that dictate fuel cell performance is provided in Section 1.3.

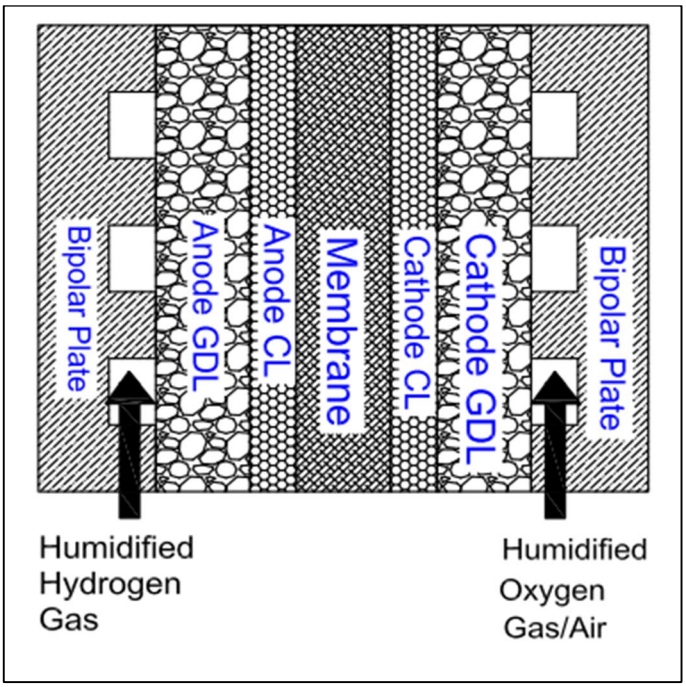

Figure 1.1: Schematic Diagram of Proton-Exchange Membrane Fuel Cell.

The technology remained little more than a curiosity until the space race helped to accelerate the pace of fuel cell development. Fuel cells provided both electricity and drinking water for the astronauts during Apollo 11 in 1969 [4, 6]. However, while appropriate for space applications which put a premium on weight and in which both fuel and oxidant had to be carried on the mission, the high cost and short life of the early fuel cell systems prevented their use in the mass market [7]. Since the early 1980s, DOE has funded research and development programs in fuel cell and this has led to a tremendous growth in the research efforts in fuel cell programs [7]. Some of the major research breakthroughs in fuel cells include: a significant reduction in catalyst layer precious-

metal loading demonstrated by Ian Raistrick at Los Alamos National Laboratory (LANL) [8], which is key in cost reduction, the development of Nafion membrane DuPont in 1968, which has shown considerably greater resistance to degradation in fuel cell environment compared to the sulfonated polystyrene divinylbenzene copolymer membrane used in early PEMFC developed by General Electric (GE) in the 1960s[4, 7], and the development of methods to limit poisoning of the catalyst due to the presence of trace impurities in the hydrogen fuel [4].

1.1.2 Potential Applications and Current Challenges in PEMFCs

Some fuel cell applications that are currently commercially viable or expected to be viable in the near-term include: specialty vehicles such as airport ground support vehicles, backup power, combined heat and power systems, and portable power [9]. Continuing research effort is needed to allow fuel cells to compete favorably in the marketplace with incumbent technologies in applications such as automotive, that have more stringent requirements in terms of cost, durability and performance [9]. The high cost of the fuel cell is due in part to the high cost of the precious metals used as catalysts in the cell, but at low production volumes, the manufacturing the cell elements dwarfs material costs[10]. As such, improvements in cell performance can reduce the total number of cells and total quantity of material required to build a device capable of delivering the specified power.

Maintaining and extending the durability of the fuel cell system is critical to ensure that the maintenance costs of applications that depend on fuel cells are comparable to those that are powered by traditional power sources. For example, in automotive applications, where there are many start-up, shut-down and transient (acceleration/deceleration) cycles, it is imperative that cars and buses run for extended

periods without stack replacement, as it would be prohibitively costly to replace the fuel cell stack after every few thousand miles. While the focus of this dissertation is not fuel cell durability, the transient model developed and many of the processes considered in the model are related to the durability of the fuel cell.

Improving the fuel cell performance is another important aspect that demands attention. One issue that is directly tied to the fuel cell performance is water management; this is especially true in low temperature PEMFC where Nafion is commonly used as membrane. It is widely reported that the conductivity of Nafion® increases as the water in the membrane phase increases. The need for a hydrated membrane necessitates operation below the boiling point of water. This leads to the accumulation of liquid water in the porous media, namely catalyst layers (CL) and gas diffusion layers (GDL); the liquid water blocks the pathway to catalyst sites [11, 12]. The accumulation of excess liquid water reduces cell performance and presents a reliability problem under dynamic load conditions and high current densities [13]. Clearly, for optimum performance water management balancing is critical in the PEMFC. This dissertation will focus more on water management and

Understanding water transport in the PEMFC will help develop new materials, designs, and operational schemes that will help remove excess liquid water in the porous media. While imaging techniques, namely magnetic resonance imaging (MRI), neutron radiography (NR) and X-ray tomography allow for direct visualization of water transport in the PEMFC, optimization of fuel cell materials for enhanced water management still requires additional understanding [14, 15]. X-ray tomography has good spatial resolution but is limited in its penetration depth through the sample. Furthermore, this technique requires that the fuel cell be rotated relative to the detection equipment, which restricts its use to steady-state investigations [16]. NR has shown good temporal resolution but the

current spatial resolution does not allow for precise quantification of water in the PEMFC sandwich [16]. There is therefore a need for numerical modeling in order to understand not only water transport but also the various electrochemical and other transport processes taking place in fuel cells. However, a model that will best explain these processes must represent as closely as possible the underlying physics of the processes.

To avoid excessive liquid water accumulation in the pores of GDL and CL as discussed above and other issues associated with low temperature operation, there is a need to develop PEMFCs that can be operated at a temperature higher than 100°C [17, 18]. When the PEMFC is operated above 100°C at near atmospheric pressure, water only exists in the vapor phase in the pores of the gas-diffusion layer and catalyst layer, and the potential problems associated with cathode flooding are avoided [17, 18]. Also, a higher operating temperature will result in faster electrochemical kinetics, enhanced heat dissipation capability because of the greater temperature difference between the cell and the surrounding environment, and higher tolerance of Pt-based anode catalysts to CO poisoning [18]. However, because the saturation pressure of water increases sharply at high temperature, operating PEMFC at a temperature above 100°C makes membrane hydration considerably more difficult [19]. High vapor pressure is required in the feed-gas stream to ensure that the membrane is well hydrated in a high temperature operation, but this would require a high total gas pressure; otherwise, a low reactant-gas pressure will lead to unacceptably high concentration overpotentials [20].

There is on-going research to develop membranes whose ionic conductivity is not strongly dependent on membrane hydration. One of the promising candidates for HT-PEMFC is phosphoric-acid-doped polybenzamidazole (PBI) membranes. PBI has shown thermal stability[21], lower permeability to hydrogen and methanol than Nafion® [21, 22], higher mechanical strength than Nafion® [21] and negligibly small electro-osmotic

drag, which alleviates anode dry-out at high current densities [23]. Even though the proton conductivity of PBI membrane increases with increasing relative humidity, the dependence is much weaker than that of Nafion® [20]. The proton conductivity of the PBI membranes depends on the phosphoric acid doping level, relative humidity, and temperature [18]. The protonic conductivity of the PBI-based membrane also improves as relative humidity increases, especially at high temperature and high doping levels [20, 22]. Li et al. [20] found that, at 200°C, an increase in relative humidity from 0.15 to 5% resulted in an increase in the conductivity from 0.038 to 0.068 Scm^{-1}. Ma et al. [22] found that at high doping levels, the conductivity increases significantly with relative humidity. At a given temperature, an increase in the relative humidity increases the water content in the membrane; this increased water content is assumed to lower the viscosity within the membrane, leading to higher mobility and conductivity [22, 24].

By finding optimum morphological properties such as porosity and pore-size distributions of the PEMFCs components, namely: gas diffusion layer (GDL), microporous layer (MPL) and catalyst layer (CL) that helps keep the water produced by electrochemical reaction in the CL, membrane can be kept more hydrated even when the external flow fields have low relative humidities.

1.2 PEMFC BASICS

We start by looking at the some of the properties of the ideal PEMFCs components that will give an optimum performance.

1.2.1 Proton-Exchange Membrane

The proton-exchange membrane resides at the heart of PEMFC. It separates the anode and cathode compartments of the fuel cell. It must have low gas permeability to prevent cross-over of reactant gases that would otherwise lead to mixed potential and loss

of performance as a result of both oxidation and reduction taking place at the same electrode surface. On the other hand, reactant gases must be able to diffuse through the ionomer in the CL to reduce mass transport limitation. There must therefore be a balance between the desired low gas permeability and the diffusion of reactant gases through the ionomer. The membrane must possess good proton conductivity to allow the proton at the anode to move to the cathode with the least resistance but must also possess poor electron conductivity to prevent electrons from travelling from the anode to the cathode through the membrane instead of through the external circuit where it is needed to perform useful work. The proton conductivity of the Nafion membrane typically used in low-temperature PEMFC increases with the water content in the membrane. This is why it is important that the Nafion membrane be sufficiently hydrated to prevent increased ionic resistance. The durability of the membrane is also important. The membrane must have high chemical and thermal stability in fuel cell environment. The Nafion membrane belongs to a class of polyperfluorosulfonic acids which consists of a hydrophobic tetrafluoroethylene backbone with pendant side chains of perfluoronated vinyl-ethers terminated by sulfonic acid groups [25]. The strong bonds between the fluorine and the carbon make Nafion durable and resistant to chemical attack [5].

For high-temperature operation, a membrane whose proton conductivity is not strongly dependent on water as that of Nafion is needed. The proton conductivity of phosporic acid doped polybenzimidazole, high temperature PEMFC used in this dissertation depends more strongly on the doping level of the membrane than on water [22, 26]. Detailed information about the proton conductivity of acid doped PBI membrane is given in the background section of this dissertation.

1.2.2 Catalyst Layer

The catalyst layer is the thinnest layer in PEMFC sandwich, and it is placed between the GDL and the proton-exchange membrane. This layer is made up of nano-sized platinum particles supported by carbon, and ionomer binder that are combined to form an agglomerate structure. The catalyst layer is a three-dimensional porous structure where the most complex multiphase transport processes take place in the fuel cell. All the three phases of water (liquid, vapor and dissolved water in the membrane) may present of once depending on the level of water saturation. It is where the electrochemical reaction takes place. The catalyst layer must be good ionic and electronic conductor. The Pt particles and carbon supports serve as electronic conductors; the ionomer is an ionic conductor. The combined structure allows both protons and electrons to access catalyst sites throughout the thickness of the catalyst layer structure. Diffusion of reactant gases through the ionomer is necessary to increase the utilization of the Pt catalyst otherwise the electrochemical reaction will be limited to those Pt particles on the surface of the agglomerates. Currently, only very expensive metals such as Pt or Pt alloy are used as catalyst in the catalyst layer. Research is underway to develop non-precious metal to replace expensive catalyst currently used in PEMFC [27].

1.2.3 Gas Diffusion Medium

In most fuel cells, the gas diffusion medium is made up of two different layers: the traditional GDL and the microporous layer, or MPL. The GDL is usually a carbon paper or carbon cloths possibly treated with Teflon to make the GDL hydrophobic. Teflon treatment is important in reducing the liquid water saturation in the GDL thereby allowing the reactant gases to reach the reacting site in the catalyst layer. The thickness of GDL is typically between 200μm and 300μm. The gas diffusion medium provides structural support for the CL. It distributes reactant gases to CL. It also provides pathway

for water to move towards or away from the CL. GDL also provides conduction pathway for the electrons from the CL to the bipolar plates. MPL is usually added to the traditional GDL to improve fuel cell performance. It is more hydrophobic and has smaller pore sizes compared to the traditional GDL. It has been observed that the use of MPL provides more intimate electrical contacts between fuel cell components and thus helps reduce contact resistance [28].

1.2.4 Bipolar Plates

The bipolar plates collect and conduct the electrical current, and also act as a separator to prevent gas mixing between adjacent cells in fuel cell stacks. Channels for the flow of the reactant gases are usually machined onto the bipolar plates, to distribute the gases over the face of the cell. Three types of channel designs commonly used in fuel cells are parallel channels, serpentine channels and interdigitated channels. The ratio of channel area to land area is very important in any flow field. Channel areas should be as large as possible to allow sufficient reactant gases to travel through the channels; this requirement must be balanced against the requirement for sufficient land area to maintain the electrical connection between the bipolar plates and the GDL, to minimize the contact resistance of the cell. Bipolar plates also provide structural integrity for the fuel cell.

1.3 PEMFC PERFORMANCE

The polarization curve is one of the most important indicators for measuring fuel cell performance. It is a plot of cell voltage vs. current density. Figure 1.2 shows a schematic diagram of a typical polarization curve for PEMFC. In an ideal fuel cell, the cell voltage will remain at reversible cell voltage, ϕ_{rev} regardless of the quantity of the current drawn from the cell. However, in any practical fuel cell, the cell voltage decreases as current is drawn from the cell due to irreversible voltage losses, also known as

overpotentials. The three different regions identified in Figure 1.2 are: activation region, ohmic region and the mass transport region. It is important to recognize that while activation overpotential dominates in activation region, ohmic overpotential dominates in ohmic region and mass transport overpotential dominates in mass transport region, all the three losses are present in all the regions.

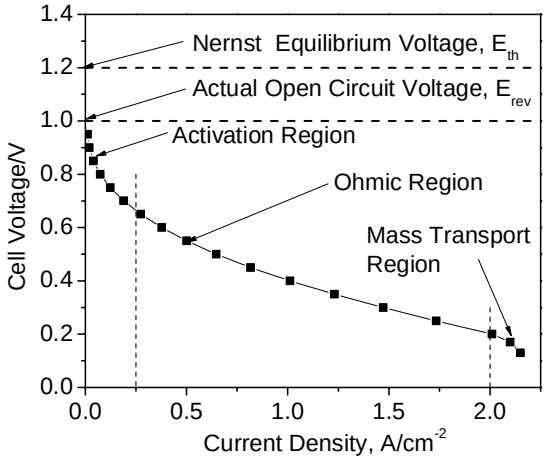

Figure 1.2: Typical Polarization Curve for PEMFC

As seen in Figure 1.2, the actual open circuit voltage is lower than the Nernst thermodynamic equilibrium voltage due to the mixed potential due to undesired fuel crossover, platinum oxidation and other contamination and impurity. Internal current due to electron leakage through the membrane also contributes to the difference between the actual open circuit voltage and Nernst thermodynamic equilibrium voltage [29, 30]. At low current density, activation losses dominate. These losses are due to the sluggish oxygen reduction reaction at the cathode catalyst layer and the poisoning of the anode Pt catalyst by carbon monoxide gases. As current increases, ohmic losses dominate the fuel cell performance losses. Ohmic losses mainly stem from ionic losses in the catalyst layer and the in the bulk membrane. However under certain operations, contact resistance and

electronic resistance are expected to be important also [10]. At high current density, mass transport losses become increasingly important. Mass transport losses reveal themselves when the concentrations of reactant gases in the catalyst layer become lowered significantly via consumption and incur a concentration drop in delivering material to the active sites. The oxygen mass transport limitation is complicated by flooding of the pores of the cathode catalyst layer and gas diffusion layer, which effectively restricts gas-phase access to the catalysts. As the current approaches the maximum value that can be sustained by gas-phase mass transport, the cell voltage will decrease sharply with any further increase in current density. For practical fuel cell operation, though, one desires to operate near the maximum power output, which occurs at high current densities. Therefore, improving mass-transport capabilities of the porous media has significant impact on the peak power attainable by the cell.

1.4 THERMODYNAMICS

The thermodynamic equilibrium voltage is derived from the thermodynamic condition when no current is drawn from the cell. The experimentally measured open circuit voltage is usually lower than the thermodynamic voltage because of the fuel cross over. The phase equilibrium representation of the PEMFC is as shown in Figure 1.3. The vertical lines denote distinct phase separation while the wavy lines show that the membrane phase separation is not sharp. Membrane extends to the catalyst layer in the adjacent region. Phase equilibrium between species exists in adjacent phases. Phases α and α' are composed of the same metal, i.e., graphite but are not necessarily in equilibrium since they may not at the same electrical potential. Similarly, phases β and β' are composed of the same material but may not be at the same electrical potential.

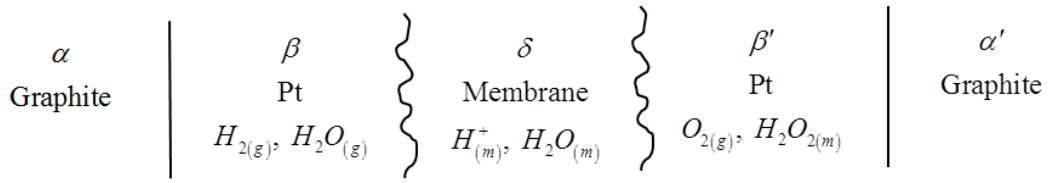

Figure 1.3: Phase Equilibrium Representation of PEMFCs

The potential of the cell is given as [10, 31]

$$FU = \mu_{e^-}^{\alpha} - \mu_{e^-}^{\alpha'}$$

$$\text{where } \mu_{e^-}^{\alpha} = \frac{1}{2}\mu_{H_2}^{\beta} - \mu_{H^+}^{\beta} \text{ and } \mu_{e^-}^{\alpha'} = \frac{1}{2}\mu_{H_2O}^{\beta'} - \frac{1}{4}\mu_{O_2}^{\beta'} - \mu_{H^+}^{\beta'} \tag{1.4}$$

$$FU = \frac{1}{2}\mu_{H_2}^{\beta} + \frac{1}{4}\mu_{O_2}^{\beta'} - \frac{1}{2}\mu_{H_2O}^{\beta'} + \left(\mu_{H^+}^{\beta'} - \mu_{H^+}^{\beta}\right)$$

where $\mu_{\varepsilon}^{\delta}$ is the electrochemical potential of s pecies ε in domain δ. If gases are assumed to be ideal and gradients in the membrane is neglected [10], we have the following:

$$U = U^{\theta} + \frac{RT}{4F}\ln\left[\frac{P_{H_2}^2 P_{O_2}}{P_{H_2O}^2}\right] \tag{1.5}$$

where U is the thermodynamic equilibrium potential, U^{θ} is the standard potential, R is the gas constant, T is the absolute temperature and F is the Faraday constant.

1.5 KINETICS

In electrochemical systems of practical importance, including fuel cell, it is reactions at the electrodes that are of primary importance [31]. The rate of electrochemical reaction depends on the following:

- The nature and the previous treatment of the electrode surface [31]
- The composition of the electrolytic solution adjacent to the electrode, just outside the double layer [31]

- The concentration of the species participating in the electrochemical reaction [10]
- The potential drop across the reaction interface between the ionomer and the electronically conducting solid phase [10]

In fuel cell, the rate of electrochemical reaction is generally described by Butler-Volmer (BV) equation. BV equation describes an electrochemical process limited by the charge transfer of electrons which is appropriate for the oxygen reduction reaction occurring that the cathode catalyst layer and in most cases hydrogen oxidation reaction occurring the anode catalyst layer when pure hydrogen is used as fuel [30]. The general BV equation can be written as follows [30]:

$$i_{cell} = i_o \left(\frac{C_s}{C^*} \right)^{\gamma} \left[\exp\left(\frac{\alpha_a F}{RT} \eta \right) - \exp\left(\frac{-\alpha_c F}{RT} \eta \right) \right] \quad (1.6)$$

Where i_{cell} is the fuel cell total current density, i_o is the exchange current density and it is a function of reaction concentration, temperature, catalyst, age and nature of the electrode, C_s is the electrode reactant concentration at the catalyst surface, C^* is the reference concentration of the reactant at STP conditions, α_a and α_c are the anodic and cathodic transfer coefficient, γ is the reaction order for the elementary charge transfer step, F is the Faraday constant, R is the gas constant, T is the absolute temperature and η is the activation overpotential at the given electrode. The first exponential term in the square bracket in eqn. [1.6] is the oxidation branch of the electrode reaction and the second exponential term in the square bracket is the reduction branch. It is the difference between the oxidation and the reduction branches that produces the net current.

In PEMFC where hydrogen oxidation reaction is generally fast, both the oxidation and the reduction branches of the BV equation are included for the hydrogen oxidation reaction. However, because the oxygen reduction reaction (ORR) is sluggish, the potential at the cathode has to be driven significantly out of equilibrium value in the

cathodic direction for the ORR to take place. Therefore, only reduction branch of the BV equation is included for the ORR at the cathode catalyst layer.

1.6 LITERATURE REVIEW

1.6.1 Water Transport in the Low-Temperature PEMFC

Major breakthroughs in PEMFCs, such as the reduction in the catalyst layer loading, buoyed by support from government and industry have brought research in PEMFC to an all-time high in the last few decades [10]. Numerical modeling of the PEMFC has been a major part of the research efforts directed at making PEMFC commercially viable. Numerical models of PEMFC vary in their dimensionality. Early numerical models of PEMFC are mostly 0-D [32-36]. 0-D model is a usually a single performance equation fitted to experimental data. They are quick and useful in analyzing data but less reliable in explaining and predicting observed behavior in PEMFC.

Springer et al. [37] and Bernardi et al. [38, 39] are two early fundamental 1-D models of PEMFC. Both treat gas diffusion layer, catalyst layer and the membrane. They are also isothermal. The main difference between the two models is how transport in the membrane is treated. Springer et al. [37] treat the membrane like a homogenous single phase, where water is assumed to dissolve in the membrane and the transport of water in the membrane is by diffusion and the driving force is the gradient of water concentration in the membrane. Bernardi et al. [38, 39] treats membrane as a two-phase system where water in the membrane behaves more like liquid water and the driving force is the gradient of hydraulic pressure of water in the membrane. Many other models that came later were influenced by the work of Springer et al. [37]. Nguyen et al. [40] developed a 2-D non-isothermal steady state model with transport in the membrane treated in a way similar to that of Springer et al. [37]. Other models that are influenced by Springer et al.

[37] are those of Amphlett et al. [41] , Okada et al. [42-44], Hubertus et al. [45], Yi et al. [46], Hsing et al. [47] and Dannenberg et al. [48]. The model of Bernardi et al. [38, 39] forms the basis for many other models too. Among them are the computational fluid dynamics (CFD) PEMFC models [49, 50]. Other models based on work of Bernardi et al. [38, 39] include that of Singh et al. [51] and Thampan et al. [52]. Weber and Newman [3, 10, 28, 53, 54] assert that the diffusion based model of Springer et al. [37] is strictly valid for a partially humidified condition and hydraulic pressure based model of Bernardi et al. [39] is strictly valid for fully humidified condition. They attempt a unified model valid for a wide range range of operating conditions by using chemical potential as the driving force for water transport in the membrane. Janssen [55] also used chemical potential as the driving force for water in the membrane. Rowe and Li [56] combine both the diffusion based and hydraulic based fluxes for water transport in the membrane. As mentioned by Weber and co-workers [57, 58], the approach of combining the two driving forces has weak physical basis as the two driving forces are supposed to strictly valid at the two extreme ends of the operating conditions. Wang and Nguyen [59-61] also combine the two driving forces.

2-D models not only consider the effects along the PEMFC sandwich but they also consider either the effects along the gas channels [46] where reaction depletion and liquid water accumulation is important or the effects across the gas channels [62, 63]where differences in transport under channel and land are studied. Effects across the gas channels are mostly important in interdigitated flow fields where there are not continuous gas channels. 3-D models consider the effects along the three directions [64-67].

While many of the modeling efforts in the literature have focused on steady state problem, understanding the dynamic processes taking in the PEMFC is also very

important, especially for applications that are subject to rapid load change such as automobile and portable applications. Next, we will review the transient models in the literature. The transient models in the literature differ in their geometric dimensionality: there are those that are 1D [11, 68, 69], 2D [70-73] and 3D [64, 74, 75]. Amphlett et al. [76], one of the first dynamic models in the literature, was a PEMFC stack. Natarajan and Nguyen [70] developed 2D transient models for only cathode CL and GDL. They showed that liquid water constitutes the slowest mass transfer phenomenon in the cathode. Wang and Wang [74], Wu et al. [71] and Meng [72] assumed thermodynamic equilibrium between water in vapor and membrane phases. Experimental studies show that the time scale for the membrane to reach its sorption equilibrium in humid air is on the order of 1000s [77]. Capturing membrane sorption/desorption is therefore essential for correct transient modeling. Shah et al. [68] and Gerteisen et al. [11] used Leverrett function for capillary pressure-saturation relation which has been used in most of the two-phase modeling because of the lack of experimentally measured capillary-saturation relations. Leverrett function was developed for an isotropic soil of uniform wettability while GDL is anisotropic, of mixed wettability because of the non-uniform PTFE coating [78]. Wu et al. [64] used modified Leverett function originally developed for GDL by Kumbur et al. [79] in both GDL and catalyst layer of their models. Their results did not show saturation discontinuity at the interface between GDL and CL, which is usually caused by two media with different capillary properties coming into contact. Weber and Newman [28] argued that if capillary pressure across the interface between the two media is continuous, the liquid water saturation across the interface should be discontinuous. The saturation discontinuity at the interface between two media has been used in some models in the literature [11, 28, 61]. The saturation jump has also been demonstrated by

bringing together two materials with different wetting properties [61]. Qu et al. [73] modeled the CL as an interface and also neglected ohmic drop in GDL.

In this dissertation, we present a 1D two-phase transient model with experimentally measured capillary pressure-saturation. We examine the effect of permanent hysteresis observed in the measured capillary pressure-saturation relation. Gostick et al., Harkness et al. and Fairweather et al. [80-82] observed that negative capillary pressure, with capillary pressure defined as total gas pressure minus liquid pressure, is required to force water into the gas diffusion layer (GDL), while positive capillary pressure is required to withdraw the water from the GDL. They also observed that primary intrusion of water into the GDL occurs at somewhat higher capillary pressure than the subsequent intrusion and that secondary intrusion is more likely to be relevant in fuel cell operation. Weber [83] used similar experimentally measured capillary pressure-saturation relation in h is steady state model, albeit the model only considered GDL.

1.6.2 Effects of MPL on the Transient Response of Low-Temperature PEMFC

Successful commercialization of proton-exchange membrane fuel cell (PEFC) for use in automotive and residential applications requires that PEFC be operated at high current density without any significant stability or material degradation issues. Flooding of the pores in g as diffusion layer (GDL) and catalyst layer (CL) has been identified as one of the main causes of stability concern in PEFC especially at high current density and low gas flow rates. One of the design iterations that has been proposed to help alleviate the flooding problem is the use o f micro-porous layer (MPL) between the t raditional GDL and CL. Experimental studies show that the use of MPL improves the fuel cell performance [84-91]. It has been hypothesized that the application of MPL between CL

and GDL helps to keep the membrane and the ionomer in the CL better hydrated, prevents flooding in the GDL, especially at high current densities and low gas flow rates, prevents CL from penetrating deeply into the GDL thereby reducing the loss of active catalyst and forms a more intimate contact between MPL and the surrounding layers (CL and GDL) [28, 84].

Researchers have attempted to use modeling to explain the observed improved fuel cell performance when MPL is used. However, the exact role of MPL in liquid water transport through the PEFC sandwich is still under debate. Nam and Kaviany [92] developed 1-D model of cathode gas diffusion medium and found that when MPL is placed between GDL and CL, the water in the MPL is lower than that of GDL. They concluded that MPL created a capillary barrier that prevents the some of the liquid water condensed in the GDL from penetrating into the CL. Similarly, Pasaogullari and Wang [93], in a cathode-side-only model, concluded that MPL enhanced liquid water removal from the CL through the GDL to the gas channel. It should be noted that because the modeling domain of Pasaogullari and Wang [93] and Nam and Kaviany [92] are only half-cell constructions, they could not account for back diffusion. On the other hand, Weber and Newman [28] modeled the full fuel cell sandwich and found that the major effect of the MPL is to promote back diffusion and membrane hydration. Wang and Nguyen [61], by considering a membrane and cathode electrode model, reached similar conclusion as Weber and Newman [28]. Wang and Nguyen [61] found that MPL increased the liquid water pressure on the cathode to a level higher than that of anode, thereby increasing the back diffusion of water through the membrane. They also suggested cracks in the MPL might reduce the liquid water build up on the cathode resulting in lower back diffusion compared to MPL with no cracks. Kang and Ju [94]

developed 3D model and found also found that MPL enhanced back flow of water from cathode to the anode.

While the above-mentioned models have provided useful insights on the role of MPL in improving the performance of fuel cells, none has focused on how the inclusion of MPL affects the transient response of PEMFC. Understanding fuel cell behavior under transient operation is very important in mobile applications like vehicles and portable devices [15, 64]. Also, as MPL is used almost all PEMFC, it is important to study how the use of MPL affects the dynamic response of PEMFC. In this dissertation, we study how the inclusion of MPL affects the transient response of PEMFC subjected load change.

1.6.3 Optimization of High-Temperature PEMFC

A number of numerical models have been developed for HT-PEMFC. Cheddie and Munroe [21] developed a 1D steady non-isothermal model with CL treated as an interface. The model assumed proton conductivity to be constant. The model was later extended to include CL as a finite region [95] and also included channel and rib effects[96]. Ubong et at. [97] developed a 3D steady state model to study the effects of temperature, pressure and air stoichiometry on cell performance. The main drawback of models developed by Cheddie and Munroe [21, 95, 96] and Ubong et al [97] is the assumption of constant proton conductivity, which has been shown to vary with both relative humidity and temperature [20, 22]. Peng et al. [98, 99] developed both 3D steady and unsteady models of HT-PEMFC. Their steady-state model [98] showed the effects of width and distribution of gas channels and ribs on cell performance. They also showed the effects of double layer charging on current density for step change in voltage [99].

Sousa et al. [100, 101] developed both 2D steady state isothermal and 2D transient non-isothermal models for HT-PEMFC. They showed that utilization of catalyst layer particles was very low at high current densities [100]. They also tried to determine the optimum phosphoric acid loading from their model [100]. In their 2D transient model, they studied the effects of double layer charging on current density during step change in voltage [101]. They also include degradation mechanisms for phosphoric acid loss from CL and platinum sintering in their transient model [101]. Jiao and Li [102] developed a 3D steady state non-isothermal model to study the effects of operating temperature, phosphoric acid doping level in the PBI membrane and inlet relative humidity on cell performance. Bergmann et al. [103] and Jiao et al [104] developed models to study the effects of CO poisoning on HT-PEMFCs. While the previous HT-PEMFC models have been helpful in understanding the various transient effects during step change and also how various operating conditions affect cell performance, none has focused on determining the optimum morphological properties of the PEMFC components that will help keep water generated by oxygen reduction reaction as much as possible in the CL to hydrate the membrane.

In this dissertation, we developed a 1D steady-state non-isothermal model is to study those optimum morphological properties of PBI-phosphoric-acid-imbibed fuel cell components that will help keep water vapor humidifying the membrane, so as to increases its proton conductivity. The model developed in this work can easily be adapted for other types of high temperature membranes.

1.7 SCOPE OF RESEARCH AND OBJECTIVE

The dissertation focuses on the transport through the PEMFC sandwich which is where the most transport and electrochemical processes take place in the fuel cell. The PEMFC sandwich comprises of the anode GDL, anode CL, proton-exchange membrane, cathode CL and cat hode GDL. PE MFC sandwich is e xplained in details in the next section. In this dissertation, we developed two major lines of numerical investigation: understanding water management with typical PEM materials operating at less than 100°C under transient condition, and evaluating how to retain water in the separator for high-temperature operation. The first part of the dissertation involves modeling the transport process in low temperature PEMFC under transient condition and the focus will include:

- Using the latest experimental data to get a more realistic result compared to what is currently in the literature.
- Developing better understand water transport in the PEMFC.
- Explaining the observed differences between hydration and dehydration time constants during load change.
- Investigating the role of MPL in transient response of proton-exchange membrane.

In this second part of the dissertation, we develop model for the optimization of the morphological properties of HT-PEMFC to retain as much water in the catalyst layer as possible to reduce the ionic resistance in the membrane. Although the model developed in this part uses phosphoric acid doped PBI membrane, the model can easily be adapted for other types of high temperature membranes.

Chapter 2: Model Development

Modeling approaches to describe PEMFC behavior can be broadly classified into microscopic and macroscopic modeling approaches. Microscopic models deal with phenomena on the pore length scale while macroscopic models are continuum and average properties over this scale. Microscopic models may provide more realistic condition and yield valuable information about what occurs in the modeling domain, it is too complex to be used in overall fuel cell model [3]. In this dissertation, a macroscopic approach for porous electrodes as described by Newman and Tiedemann [105] is used. In this approach, the exact geometric detail of the modeling domain is neglected. Instead, the medium is treated as randomly arranged porous structure where quantities such as electric potential, ϕ_1 in the solid phase and ionic potential, ϕ_2 in the ionomer phase are assumed to be continuous function of time and space coordinates. Fluctuations in transport properties in the porous media are neglected rather an average value is used. This averaging is valid for regions that are large compared to the pore structure but small compared to the regions over which the macroscopic variation occurs [54].

2.1 Governing Equations for the Transient Response of Proton-Exchange Membrane Fuel Cell Subjected to Load Change

The modeled domain consists of the anode gas diffusion layer (aGDL), anode catalyst layer (aCL), membrane, cathode catalyst layer (cCL), cathode microporous layer (cMPL) and cathode gas diffusion layer (cGDL). The liquid water in the GDL and CL is assumed to move due to capillary forces only (convective force is neglected). Water in the membrane is assumed to reside in the ionomer phase alone. Other assumptions implicit in this work are:

- The total gas pressure is assumed to be constant.

- Temperature is assumed to be uniform. The uniform temperature assumption is reasonable for a single cell where constant temperature conditions are easier to maintain.
- Water in the membrane interacts significantly with the sulfonic acid group in the membrane.
- The double-layer charging time constant has been shown to be in the order of micro seconds and can therefore be safely neglected [74]. This implies that charge transport can be treated as steady state in this transient problem.
- Reactant gases and vapor behave as ideal gases.
- Gas transport is dominated by diffusion (convection is neglected).

2.1.1 Transport of electric charges

The charge transfer is only through electronic phase in the GDL and MPL. Also, charge transfer in the bulk membrane is only through ionic phase. Because of the presence of both ionomer and electronically conductive solid phase in the CL, charge transfer in the CL is through both ionic and electronic phase. During electrochemical reaction, charge transfer occurs. Electrochemical double layer charging/discharging occurs in a thin layer adjacent to the reaction interface in the CL. Wang and Wang [74] estimated the time constant for the double layer and found it to be in the order of microseconds. Since the time constant for the double layer is much smaller than the time constant for water transport that we are interested in, we neglect the double layer charging in this model.

The transport of electrons through the GDL and CL is governed by Ohm's law

$$i_1 = -\sigma_s e_s^{1.5} \nabla \phi_1 \tag{2.1}$$

where σ_s and e_s are the electronic conductivity and volume fraction of the electronically conductive solid phase respectively. ϕ_1 is the electric potential in the electronically conductive solid phase. Similarly, Ohm's law can be used to describe the transport of ions through the ionomer in the CL and membrane

$$i_2 = -\sigma_m e_i^{1.5} \nabla \phi_2 \tag{2.2}$$

where σ_m and e_i are the ionic conductivity and volume fraction of the ionomer respectively. ϕ_2 is the electric potential in the membrane. The conservation of electronic charge in the GDL is governed by

$$\nabla \bullet i_1 = 0 \tag{2.3}$$

For the current balance in the CL, the transfer current between the membrane and the electronically conductive solid gives [28, 57]

$$\nabla \bullet i_2 = -\nabla \bullet i_1 = a_{1,2}^0 i_h (1-s) E \tag{2.4}$$

where $a_{1,2}^0$ is the specific interfacial reaction area, i_h is the transfer current for reaction h, and E is the effectiveness factor. In this model, because of the high diffusion coefficient of H_2, we assume that the effectiveness factor for hydrogen oxidation reaction (HOR) at the aCL is unity. At the cCL, the effectiveness factor is determined from agglomerate model with the potential assumed to be uniform in each of the spherical agglomerates, but allowed to vary across the thickness of the catalyst layer. The liquid water in the pore of aCL and cCL are taken into account by multiplying the specific interfacial area for reaction by the factor of $(1-s)$, where s is the liquid water saturation in the pore[28]. Both oxygen reduction reaction (ORR) and HOR are assumed to be first-order reaction. The transfer current for the ORR and HOR are [28] as follows

$$i_{HOR} = i_{0_{HOR}} \left[\frac{p_{H_2}}{p_{H_2}^{ref}} \exp\left(\frac{\alpha_a^a F}{RT} \left(\Phi_1 - \Phi_2 \right) \right) - \exp\left(\frac{-\alpha_c^a F}{RT} \left(\Phi_1 - \Phi_2 \right) \right) \right] \tag{2.5}$$

$$i_{ORR} = -i_{0_{ORR}} \left(\frac{p_{O_2}}{p_{O_2}^{ref}} \right) \exp\left[\frac{-\alpha_c^c F}{RT} \left(\Phi_1 - \Phi_2 - U^\theta \right) \right] \tag{26}$$

respectively, where α_a^a and α_c^a are the anodic and cathodic transfer coefficients respectively for the hydrogen oxidation reaction. α_c^c is the cathodic transfer coefficients for oxygen reduction reaction. $p_{O_2}^{ref}$ and $p_{H_2}^{ref}$ are the reference partial pressure of oxygen and hydrogen respectively. For a first-order reaction, the effectiveness factor at cCL can be written as [57]

$$E = \frac{1}{3\phi^2} \left(3\phi \coth\left(3\phi\right) - 1 \right) \tag{27}$$

where ϕ is the Thiele modulus for the system [28]:

$$\phi = \sqrt{\frac{R_{Agg}^2 k'}{\psi_{Agg}}} = \sqrt{\phi_{mt} k'} \tag{28}$$

where R_{Agg} is the radius of the agglomerate in the cCL, ψ_{Agg} is the O_2 permeation coefficient into the agglomerate, and ϕ_{mt} is the mass-transfer portion of the Thiele modulus. The mass-transfer portion represents the size and reactant gas permeation into the agglomerate. k' is the kinetic portion of the Thiele modulus and is given as [28]

$$k' = \frac{a_{1,2}^o i_{ORR}}{4F p_{O_2}^{ref}} \exp\left(-\frac{\alpha_c^c F}{RT} \left(\Phi_1 - \Phi_2 - U^\theta \right) \right) \tag{29}$$

2.1.2 Transport of water in membrane phase

The Nafion® typically used in low temperature PEMFC has been shown to consist of hydrophilic sulfonic acid sites and hydrophobic polymer backbone. Dry perfluorinated membrane is almost completely non-conductive [30]. When the membrane is hydrated, the dry membrane absorbs water in order to solvate the sulfonic acid group, $H^+SO_3^-$. The initial water is associated strongly with the sulfonic acid sites. With the addition of more water in the membrane, the water becomes less bound and ionic cluster is formed in the polymer [54]. The presence of the water in the membrane boosts proton conductivity and

reduces ohmic losses. In an operating cell, water is transported along with the proton from the anode to the cathode side of the membrane. Two modes of proton transport in the membrane have been suggested. The dominant mode of transport depends on the water content in the membrane. At low water content, proton transport is dominated by diffusion or vehicular mechanism. The water is strongly bound to the sulfonic acid sites at low water content and the water has to move through void fraction from one charged site to another. Because the H^+ is weakly bound to the SO_3^-, it is possible for the proton to jump from one sulfonic acid site to another. Increasing the number of SO_3^- in the membrane enhances the proton transport by reducing the distance between the SO_3^-, but the mechanical and thermal strengths of the membrane are reduced [106]. The diffusion or vehicle mechanism depends mainly on the diffusion coefficient of water in the membrane which depends on water content and the local temperature in the membrane. With high hydration of the membrane, a proton hopping or Grotthus mechanism is observed. In this mode of transport, protons "hop" from one H_3O^+ to another along a connected pathway [30].

The conservation equation for the transport of water in the membrane phase is as shown in eq. 2.10

$$\frac{e_i}{\bar{V}_m}\frac{\partial \lambda}{\partial t} = -\nabla \bullet N_{wm} + R_{wm} \tag{2.10}$$

where e_i is the ionomer volume fraction, $\bar{V}_m$ is the molar volume of the dry membrane, λ is the water content in the membrane, which is the moles of water per equivalent of sulfonic acid sites, N_{wm} is the superficial flux density of water in the membrane, and R_{wm} is the source term. In the bulk membrane, e_i=1. N_{wm} is governed by dilute-solution theory:

$$N_{wm} = -\frac{e_i^{eff}}{V_m} D_\lambda^{eff} \frac{\partial \lambda}{\partial y} + \frac{\xi i_2}{F} \tag{2.11}$$

The flux of water in the membrane comprises two parts: back-diffusion which arises due to the gradient in concentration of water in the membrane and electro-osmotic drag accounts for the water molecule dragged along with the protons moving from the anode to the cathode side of the membrane. The drag coefficient, ξ is the ratio of water molecules carried across the membrane per unit proton transported [107]. The drag coefficient is shown to be constant for vapor equilibrated membrane but increases with water content for liquid equilibrated membrane [107-110]. The values used in this work are shown in Table I. At both aCL and cCL, water can be absorbed or desorbed from the membrane depending on the direction of the driving force given by the difference in equilibrium water content, λ_{eq} and the water content, λ in the membrane. The equilibrium water content, λ_{eq} is defined as

$$\lambda_{eq} = \begin{cases} 0.3 + 6a\left[1 - \tanh(a - 0.5)\right] + 3.9\sqrt{a}\left[1 + \tanh\left(\dfrac{a - 0.89}{0.23}\right)\right] & a \le 1 \\ 16.8s + \lambda\,|_{(a=1)}\,(1 - s) & a > 1 \end{cases} \tag{2.12}$$

The equilibrium water content used by Wu et al. [64] is slightly modified here. Where a is the water vapor activity. Water generated by ORR in the cathode catalyst layer is assumed to be in the ionomer phase. The source term, R_{wm} for aCL and cCL are as follows

$$R_{wm}^{aCL} = \frac{k_{a/d}^{mem}}{\bar{V}_m}(\lambda_{eq} - \lambda) \tag{213}$$

$$R_{wm}^{CCL} = \frac{1}{2F} a_{12}^{o} i_{ORR}(1 - s)E + \frac{k_{a/d}^{mem}}{\bar{V}_m}(\lambda_{eq} - \lambda) \tag{2.14}$$

respectively, where $k_{a/d}^{mem}$ is the absorption or desorption rate. The value of $k_{a/d}^{mem}$ is given in table I Because water in the bulk membrane is assumed to be in the ionomer phase which implies that there is no phase change and no water is generated in the bulk membrane, R_{wm} in the bulk membrane is zero.

2.1.3 Transport of gas species

The conservation equation for the transport of gases in CL and GDL is as shown in eq. 2.15

$$\frac{e_G}{RT}\frac{\partial p_i}{\partial t} = -\nabla \bullet N_i + R_i \tag{2.15}$$

where p_i and N_i are the partial pressure and molar flux of the species *i* respectively. *R* is the universal gas constant, *T* is the absolute temperature. R_i is the rate of generation or consumption of the species *i*, and e_G is the gas phase volume fraction defined as:

$$e_G = e_o(1-s) \tag{2.16}$$

where e_o is the bulk porosity. As shown by Natarajan and Nguyen [70], liquid water is the slowest mass transfer phenomenon in the CL. Because liquid water saturation, s changes much more slowly than the reactant gases, we can neglect the change in e_G over the course of the time step used in the model.

The flux term for the species *i* in eq. 2.15 governed by the Stefan-Maxwell multicomponent diffusion equation [10, 111] as shown below

$$\nabla p_i = \sum_{j \neq i} \frac{RT}{p_G D_{i,j}^{eff}} \left(p_i N_j - p_j N_i \right) \tag{2.17}$$

where p_i is the interstitial partial pressure of species i, p_G is the total gas-phase pressure, which is assumed to be constant, $D_{i,j}^{eff}$ is the effective binary diffusion coefficient between species i and j. The values of $D_{i,j}^{eff}$ are given in Table II. In the GDL, where there is no homogeneous generation or consumption of the reactant gases, the rate of generation term, R_i for oxygen and hydrogen transport is zero. For vapor-phase transport in the GDL, R_i is the rate of evaporation or condensation, R_w and is as shown in eq. 2.18 [112]

$$R_w = \frac{k_e e_G \rho_0}{M_0} s(p_0^{sat} - p_0) \times switch + \frac{k_c e_G (1-s) p_0}{p_G} \frac{(p_0^{sat} - p_0)}{RT} \times (1 - switch) \tag{2.18}$$

where M_0 is the molecular weight of water, k_e is the evaporation rate constant, k_d is the condensation rate constant, ρ_0 is the density of the water vapor, p_0 is the partial pressure of the water vapor and p_0^{sat} is the saturated vapor pressure. The first term in eq. 18 is the rate of evaporation while the second term is the condensation rate. The switch is designed so that only one of the functions is turned on at a time depending on the direction of the driving force, which is the difference between the saturated vapor pressure and the vapor pressure of water at the operating temperature [70]. The switch is given by eq. 2.19

$$switch = \left[\frac{1}{2} + \frac{| p_0^{sat} - p_0 |}{2(p_0^{sat} - p_0)} \right] \tag{2.19}$$

Since hydrogen gas is consumed by HOR at the aCL, the generation term, R_i for the transport of hydrogen in the aCL can be given as

$$R_{H_2} = -\frac{1}{2F} a_{12}^o (1-s) i_{HOR} E \tag{2.20}$$

Similarly, oxygen is consumed by ORR at the cCL. The generation term, R_i for the transport of oxygen in the cCL is given as

$$R_{O_2} = -\frac{1}{4F} a_{12}^o (1-s) i_{ORR} E \tag{2.21}$$

For the transport of water vapor in both aCL and cCL, the generation term, R_i is given as

$$R_{H_2 0} = -\frac{k_{a/d}^{vap}}{V_m} (\lambda_{eq} - \lambda) + R_w \tag{2.22}$$

where R_w is the evaporation or condensation rate given by eq. 2.18. The first term on the LHS of eq. 2.22 is the absorption or desorption term while the second term is the evaporation or the condensation term. Absorption of water into the membrane occurs when $\lambda < \lambda_{eq}$ and desorption occurs when $\lambda > \lambda_{eq}$. Based on the assumption that the evaporation rate is so fast that any liquid water formed evaporates quickly as long as the gas phase is not saturated, desorption from the ionomer goes to vapor phase if the water

vapor is not saturated. However, once water vapor is saturated, desorption goes to liquid phase. Therefore k_d^{vap} is zero when water vapor is saturated but its value is as g iven in Table II when water vapor is not saturated.

Similarly, absorption is assumed to come from the vapor phase if water vapor is not saturated. However when water vapor becomes saturated, absorption is assumed to come from both water vapor and liquid water. As a simplified approach, we assume that the fraction of the absorption from liquid phase is proportional to saturation, *s*, while that from vapor phase is proportional to (1-s). The value of k_a^{vap} is given by Table II when water vapor is not saturated but when water vapor becomes saturated, the value of k_a^{vap} is:

$$k_a^{vap} = (1-s)k_a \tag{223}$$

where k_a is given by Table II.

2.1.4 Transport of liquid water

The transport of liquid water in both CL and GDL is governed by

$$e_o \rho_L \frac{\partial s}{\partial t} = -\nabla \bullet N_L - M_0 \times R_L \tag{224}$$

where ρ_L is the density of the liquid water, N_L is the liquid water flux, M_0 is the molecular weight of water and R_L is the source term for the liquid water transport. The flux of liquid water is governed by Darcy's law

$$N_L = -\frac{\rho_L k_r k_{abs}}{\mu_L} \frac{dp_L}{dx} \tag{225}$$

where k_r is the relative permeability, k_{abs} is the absolute permeability of the porous media, μ_L is the dynamic viscosity of liquid water, and p_L is the liquid water pressure. In this work, capillary pressure, p_c is defined as

$$p_c = p_G - p_L \tag{226}$$

Total gas pressure, p_G is assumed to be constant. By substituting eq. 2.26 into eq. 2.25, we obtain the following

$$N_L = \frac{\rho_L k_r k_{abs}}{\mu_L} \frac{dp_c}{ds} \frac{ds}{dx} \tag{27}$$

Absolute permeability is an intrinsic property of the medium and it can be approximated by the Kozeny-Carman equation [68, 78]

$$k_{abs} = \frac{e_o^3}{k e_o (1-e_o) S_0^2} \tag{2.28}$$

where k is the Kozeny constant and S_0 is the specific surface area based on the solid's volume. We used Wyllie expression for relative permeability, k_r , which is based on cut-and-rejoin model of tubes [78], and is as follows

$$k_r = s^3 \tag{2.29}$$

In the GDL where only evaporation and condensation take place, the source term, R_L is given by eq. 2.18. However in the CL, where in addition to evaporation and condensation, absorption and desorption of water from the membrane phase take place, R_L is defined as

$$R_L = R_w + \frac{k_{a/d}^{liq}}{V_m}\left(\lambda_{eq} - \lambda\right) \tag{30}$$

where both k_a^{liq} and k_d^{liq} are zero when water vapor is not saturated. However when water vapor becomes saturated, the desorption of water from the ionomer phase is assumed to go the liquid phase and the both liquid and water vapor contribute to the absorption of water into the ionomer phase. Therefore, k_d^{liq} and k_a^{liq} are given as

$$k_d^{lid} = k_d \tag{31}$$

$$k_a^{liq} = s k_a \tag{32}$$

respectively. Where k_d and k_a are given in Table I. In this study, we use the capillary pressure-saturation relation measured experimentally by Gostick et al [81]. Though ex-situ and equilibrium measurements, their data provides more information than previously obtained [83] and thus serves as basis for a more accurate description of the liquid water

transport in the GD L. It has been observed that the capillary pressure data for water intrusion and water withdrawal shows permanent hysteresis [80-82, 113]. In this study we examine the implication of including t he hysteresis effect on the modeling results. For ease of use in modeling, we fitted polynomials to the experimentally measured capillary pressures of compressed Toray 120C in Gostick et al [81] as shown in Figure 2.1. The polynomial expressions fitted to both secondary injection and primary withdrawal capillary pressures are as shown in appendix A.

Almost all the experimentally measured capillary pressure-saturation relations in the literature are for GDL. In absence of suitable experimentally measured CL capillary pressures, we choose an approach similar to that of Leverett J-function, where the CL capillary pressure is a constant multiplied by the GDL capillary pressure. Leverett J-function for GDL and CL capillary pressure-saturation relation is given as [11, 15, 114]

$$p_C^{\Omega} = \sigma_w \cos\left(\theta^{\Omega}\right)\sqrt{\frac{e_o^{\Omega}}{k_{abs}^{\Omega}}}\left(1.417s - 2.12s^2 + 1.263s^3\right) \tag{2.33}$$

where σ_w is the surface tension of water and θ^{Ω} is the contact angle of domain Ω, which can be CL or GDL. In the case of Leverett J-function, the constant is given as

$$\text{constant for Leverett J-function} = \frac{\cos(\theta_{CL})}{\cos(\theta_{GDL})}\left(\frac{e_o^{CL}}{k_{abs}^{CL}}\right)^{0.5}\left(\frac{k_{abs}^{GDL}}{e_o^{GDL}}\right)^{0.5} \tag{2.34}$$

The constant represents the difference in the capillary properties, namely: contact angle, porosity and permeability of the two porous media.

As an initial approximation, we choose $p_C^{CL} = 1.3\,p_c^{GDL}$ as our base case for both secondary injection and withdrawal CL capillary pressures. Similar to the Leverett J-function, the constant used to multiply the capillary pressure of GDL represents the difference in the capillary properties of the two porous media. The plots of the base case CL capillary pressures are also shown in Figure 2.1. In this work, we assume that CL

capillary pressure also exhibits hysteresis. However, we do acknowledge that more work is needed to determine whether or not CL capillary pressure truly does show hysteresis.

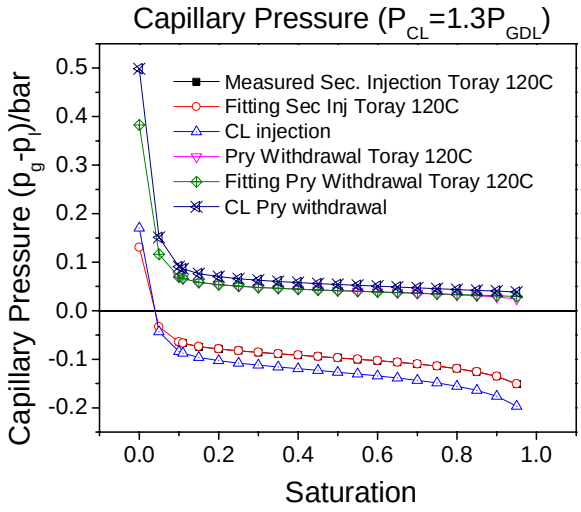

Figure 2.1. Capillary pressures of compressed Toray 120C

The electrochemical and physical relationships used in this work are given in Table I. The physical parameters used in this study are listed in Table II.

Description	Expression
Membrane water diffusivity, D_λ (cm^2S^{-1})	$10e-6\exp\left[2416\left(\frac{1}{303}-\frac{1}{T(K)}\right)\right]$ $\left(2.563-0.33\lambda+0.0264\lambda^2-0.000671\lambda^3\right)$ [37]
Electro-osmotic drag coefficient, ξ	$\xi=\begin{cases}1 & \lambda<9\\ 0.117-0.0544 & \lambda\geq 9\end{cases}$ [115]
Proton Conductivity, σ_i	$\sigma_i=\left(0.005139\lambda-0.00326\right)\exp\left[1268\left(\frac{1}{303}-\frac{1}{T}\right)\right]$ [37]
Absorption Rate, k_a (S^{-1})	$k_a=\frac{4.59e-5\,f_v}{d_{CL}}\exp\left[2416\left(\frac{1}{303}-\frac{1}{T}\right)\right]$, $f_v=\frac{\lambda V_w}{V_m+\lambda V_w}$ [116]

Desorption Rate, k_d (S^{-1})	$k_d = \frac{4.59e-5 f_v}{d_{CL}} \exp\left[2416\left(\frac{1}{303}-\frac{1}{T}\right)\right]$ [116]
Equilibrium Potential, U^θ	$U^\theta = 4.1868\left(\frac{70650+8T\ln T-92.84T}{2F}\right)V$ [10]

Table I: Electrochemical and physical relationships

Parameters	Value
Thickness of CL/GDL	20 μm /250 μm [10]
Thickness of membrane, Nafion® 117	177.8 μm [10]
Porosity of CL/CGL, e_o	0.3/0.6 [64]
Nafion® content in CL, e_i	0.3wt% [64]
Liquid water density, ρ_L	0.9718 g/cm^3
Molar volume of dry membrane, V_m	550 cm^3/mol
Evaporation rate constant, k_e	100 1/(atm s) [59]
Condensation rate constant, k_c	100 s^{-1} [59]
Cathode exchange current density, i_{ORR}	$1.5e-7$A/cm^2 [28]
Anode exchange current density, i_{HOR}	$1.4e-3$A/cm^2 [28]
Cathodic transfer coefficient for HOR, α_c^a	1 [28]
Anodic transfer coefficient for HOR , α_a^a	1 [28]
Cathodic transfer coefficient for ORR, α_c^a	1 [28]
Reference partial pressure of O_2, $p_{O_2 ref}$	1.01325bar
Reference partial pressure of H_2, $p_{H_2 ref}$	1.01325bar
O_2 permeation coefficient in agglomerate, $p_{O_2 agg}$	$1.5e-11$mol/(bar cm s) [10]
Agglomerate radius in cathode, R_{aggcat}	$110e-5$cm [10]

Electrode specific surface area, a_{12}^{o}	1e5cm^{-1} [28]
Water vapor /O_2 diffusion coefficient, D_{0,O_2}^{eff}	$0.282\frac{p_G}{p_G^{ref}}\left(\frac{T(k)}{307.1}\right)^{1.5}$ cm^2/s [117]
Water vapor/ H_2 diffusion coefficient, D_{0,H_2}^{eff}	$0.915\frac{p_G}{p_G^{ref}}\left(\frac{T(k)}{307.1}\right)^{1.5}$ cm^2/s [117]
Electronic conductivity, k_s	100 S/cm [28]
CL absolute permeability, k_{abs}^{CL}	1e-12cm^2
GDL absolute permeability, k_{abs}^{GDL}	8.7e-10cm^2
Liquid water dynamic viscosity, μ_L	3.5e-9bar s [118]

Table II: Parameters used in the model

2.1.5 Boundary Conditions

The boundary conditions used in this model are summarized in Table III below. Fully saturated inlet conditions are used as the base case for anode and cathode. As no liquid water was observed at the anode side in any of the cases considered in the model, we choose, as our base case, the saturation, s_0 at the anode side to be zero while that at the cathode side is assumed to be 0.05.

Variables	GC/aGDL	aGDL/aCL	aCL/Mem	Mem/cCL	cCL/cGDL	cGDL/GC
λ		$\frac{\partial\lambda}{\partial y}=0$			$\frac{\partial\lambda}{\partial y}=0$	
p_0	p_0 given					p_0 given
p_{H_2}	p_{H_2} given					
p_{O_2}						p_{O_2} given
N_0			$N_0=0$	$N_0=0$		

N_{H_2}			$N_{H_2}=0$	$N_{H_2}=0$		
N_{O_2}			$N_{O_2}=0$	$N_{O_2}=0$		
i_1			$i_1=0$	$i_1=0$		
i_2		$i_2=0$			$i_2=0$	
ϕ_1	$\phi_1=0$					$\phi_1=V_{cell}$
ϕ_2		$\frac{\partial \phi_2}{\partial y}=0$				
s_{GDL}	$s=s_0$	$N_L^{GDL}=N_L^{CL}$			$N_L^{GDL}=N_L^{CL}$	$s=s_0$
s_{CL}		$p_c^{GDL}=p_c^{CL}$	$N_L^{CL}=0$	$N_L^{CL}=0$	$p_c^{GDL}=p_c^{CL}$	

Table III: Summary of boundary conditions.

2.2 MODEL DEVELOPMENT FOR THE EFFECTS OF MPL ON TRANSIENT RESPONSE OF PEMFC TO LOAD CHANGE

The modeled regions in this section include anode gas diffusion layer (aGDL), anode catalyst layer (aCL), membrane, cathode catalyst layer (cCL), cathode micro-porous layer (cMPL) and cathode gas diffusion layer (cGDL). The assumptions in this model are the same as those listed in section 2.1.

It has been suggested that the use of MPL reduces the contact resistance between the layers in the gas diffusion medium and the CL [28]. To account for this reduction in contact resistance, the contact resistance in cases without MPL is taken to be $0.1\Omega cm^2$ while that of cases with MPL is taken to be $0.06\Omega cm^2$. Table IV shows the parameters used in the model. All other parameters not given in Table IV are taken from section 2.1.

Most of the governing equations for aGDL, aCL, membrane, cCL and cGDL are the same as those reported in section 2.1. The only addition to the modeling domain

reported in section 2.1 is the cMPL which is placed between the cCL and cGDL. The transport of electric charges and the transport of liquid water in MPL are the same as those in GDL. We briefly explain here the transport of gas species in MPL, GDL and CL. The reader is referred to section 2.1 for the transport of electric charges and liquid water in MPL.

2.2.1 Transport of gas species

The transport of gas species in the MPL, GDL and CL is governed by the following conservation equations.

$$\frac{e_s}{RT}\frac{\partial(1-s)\,p_i}{\partial t} = -\nabla \bullet N_i + S_T \tag{2.35}$$

where p_i is the partial pressure of the gas species which can either be oxygen or water vapor, e_s is the porosity of the porous medium, R is the universal gas constant, T is the absolute temperature in Kelvin, s is the liquid water saturation, N_i is the flux of the gas species and S_T is the source term. The source term, S_T is zero for oxygen since no reaction takes place in the MPL. However for water vapor, the source, S_T is the rate of evaporation or condensation which is given as [112]:

$$\begin{aligned} S_0 &= \frac{k_e e_s \rho_0}{M_0} s(p_0^{sat} - p_0) \times switch + k_c e_s (1-s)\frac{(p_0^{sat} - p_0)}{RT} \times (1 - switch) \\ switch &= \left[\frac{1}{2} + \frac{|\, p_0^{sat} - p_0 \,|}{2(p_0^{sat} - p_0)}\right] \end{aligned} \tag{2.36}$$

where k_e and k_c are the rates of evaporation and condensation respectively and their values are given in Table II in section 2.1, ρ_0 is the vapor pressure density, M_0 is the molar mass of vapor pressure, p_0^{sat} is the saturation vapor pressure at the operating condition, p_0 is the local vapor pressure. The switch is designed to be either zero or one depending on whether it is evaporation or condensation is taking place respectively. The flux of gas species was given by Stefan-Maxwell equation in section 2.1. Here we use a

more complete momentum equation for the flux of gas species in the GDL, MPL and CL which is given as [58, 111]

$$\nabla p_i = \sum_{j \neq i} \frac{RT}{p_G D_{i,j}^{eff}} \left(p_i N_j - p_j N_i \right) - \frac{RT}{D_{k,i}^{eff}} N_i \tag{2.37}$$

where the first term on the right the Stefan-Maxwell equation and the second term on the right is the Knudsen diffusion. p_G is the total gas pressure, $D_{i,j}^{eff}$ is the effective binary diffusion coefficient between species i and j. $D_{k,i}^{eff}$ is the effective Knudsen diffusion coefficient and is as given as

$$\begin{aligned} D_{k,i}^{eff} &= \frac{e_s}{\tau} D_{k,i} \\ D_{k,i} &= \frac{2}{3} \left(\frac{8RT}{\pi M_i} \right)^{1/2} r_p \end{aligned} \tag{2.38}$$

where e_s and τ are the porosity tortuosity of the porous medium respectively, M_i is the molar mass of the gas species and r_p is the mean pore size of the porous medium.

Parameters	*Value*
Thickness of GDL/MPL/CL	250 μm/50 μm /20μm[10]
Porosity of CGL/MPL/CL e_o	0.55/0.3/0.3[64]
MPL absolute permeability, k_{abs}^{CL}	1e-11cm^2

Table IV: Parameters used in the model

2.2.2 The boundary conditions

The boundary conditions used in this model are similar to those used in Table III in section 2.1. Only the boundary conditions that are different from those shown in Table III in section 2.1 are shown in Table V below. The liquid saturation is assumed to be constant at the interface between the GDL and the gas channels. The saturation is

assumed to be zero at the interface between the aGDL and the gas channels while a value of 0.1 is assumed at the interface between the cGDL and the gas channel.

Variables	*GC/aGDL*	*aGDL/aCL*	*aCL/Mem*	*Mem/cCL*	*cCL/cMPL*	*cMPL/cGDL*	*cGDL/GC*
λ		$\frac{\partial \lambda}{\partial y} = 0$			$\frac{\partial \lambda}{\partial y} = 0$		
i_2		$i_2 = 0$			$i_2 = 0$		
s_{GDL}	$s = s_0$	$N_L^{GDL} = N_L^{CL}$				$N_L^{MPL} = N_L^{GDL}$	$s = s_0$
s_{MPL}					$N_L^{CL} = N_L^{MPL}$	$p_c^{MPL} = p_c^{GDL}$	
s_{CL}		$p_c^{GDL} = p_c^{CL}$	$N_L^{CL} = 0$	$N_L^{CL} = 0$	$p_c^{CL} = p_c^{MPL}$		

Table V: Summary of boundary conditions

2.3 Model Development for Parametric Study of the Morphological Proprieties of HT-PEMFC Components for Effective Membrane Hydration

The model includes the transport in the following regions: anode gas diffusion layer (aGDL), anode micro-porous layer (aMPL), anode catalyst layer (aCL), membrane, cathode catalyst layer (cCL), cathode micro-porous layer (cMPL) and cathode gas diffusion layer (cGDL). The following assumptions are made in the model:

- Steady state operation is assumed.
- Because the operating temperature is above the boiling point of water, 100°C, water in all porous materials is assumed to reside exclusively in the vapor phase.
- By similar logic, the water generated by electrochemical reaction is assumed to be in the vapor phase.

- Reactant gases and vapor are assumed to behave as ideal gases.
- The gas permeability through the membrane is assumed to be negligibly small[23], such that gas cross-over can be neglected.
- The gas supply (stoichiometry) is assumed to be sufficiently high so that there is little variation in gas concentration along the gas channels.
- Contact resistance between adjacent components is assumed to be negligible.
- Water transport through the membrane is neglected due to the dry environment in HT-PEMFC and also because of the negligibly small water electro-osmotic drag force in the acid doped PBI membrane. Similar assumptions are used in the literature [102].

2.3.1 Transport of electric charges

The transport of electrons in GDL, MPL and CL and the transport of ions in CL and bulk membrane are as described in section 2.1.1. The difference between the Nafion® membrane used in section 2.1 and the acid doped PBI membrane used in this section is in how proton is transported across the membrane. Here we explain the proton conductivity of the acid doped PBI membrane. The temperature dependence of the proton conductivity is described by an Arrhenius equation [22, 26]

$$k_m = \frac{\sigma_o}{T}\exp\left(-\frac{E_a}{RT}\right) \tag{2.39}$$

where σ_o is the pre-exponential factor of the conductivity, T is the absolute temperature, E_a is the activation energy and R is the universal gas constant. Ma et al. [22] showed that for less than 10% RH, activation energy, E_a is independent of RH for phosphoric acid doping levels of 420% and 630%, while it increases with RH for an acid doping level of 300%. In this study, we are interested in a low RH condition that would be encountered at an elevated temperature operation and also at reasonable doping level of 400% to 650%.

Therefore, the activation energy, E_a can be assumed to depend only acid doping level under these conditions. We adopt the pre-exponential factor and activation energy derived by Jiao and Li [102] because they fit the conditions we are interested in. The proton conductivity, k_m is shown in table IV.

2.3.2 Transport of gas species

The conservation equation for the transport of gas species in the GDL, MPL and CL is given

$$\nabla \bullet N_i = R_i \tag{2.40}$$

where R_i is the reaction term and N_i is the flux of species i which is governed by the following momentum equation [58, 119]

$$\nabla p_i = \sum_{j \neq i} \frac{RT}{p_G D_{i,j}^{eff}} \left(p_i N_j - p_j N_i \right) - \frac{RT}{D_{k,i}^{eff}} N_i - \frac{p_i}{RT} \left(\bar{V}_i - \frac{M_i}{\rho_G} \right) \nabla p_G \tag{2.41}$$

where the first term on the right is the Stefan-Maxwell multicomponent diffusion equation and p_i is the interstitial partial pressure of species i, R is the universal gas constant, T is the absolute temperature, p_G is the total gas-phase pressure, $D_{i,j}^{eff}$ is the effective binary diffusion coefficient between species i and j; by the Onsager reciprocal relationships, $D_{i,j}^{eff} = D_{j,i}^{eff}$. The second term on the right is the Knudsen diffusion term, which represents the interactions between the molecules of the species i and the pore walls. Knudsen diffusion is significant when the pore radius is less than about 0.5μm [49]. In this model, the GDL mean pore diameter is taken to be 20μm [120, 121], the MPL mean pore diameter is taken be 0.06μm [120] and CL mean pore diameter is taken to be 0.08μm [11]. We therefore expect Knudsen diffusion to be significant in both the MPL and CL. The last term on the right is the pressure diffusion term, which is usually neglected, but it is expected to be significant on the anode side, where the molar mass of water vapor is very different from that of hydrogen [58]. In the pressure diffusion

component of gas transport equation [37], $\bar{V}_i$ and M_i are the molar volume and molar mass of the gas species i, ρ_G is the density of the gas mixture. $D_{k,i}^{eff}$ in the second term on the right in eqn. [2.41] is the effective Knudsen diffusion coefficient and is given by [94]

$$D_{k,i}^{eff} = \frac{e}{\tau} D_{k,i}$$
$$D_{k,i} = \frac{2}{3}\left(\frac{8RT}{\pi M_i}\right)^{1/2} r_p \tag{2.42}$$

where e and τ are the porosity and the tortuosity of the porous medium. R is the universal gas constant, T is the absolute temperature, M_i is the molar mass of species i and r_p is the mean pore radius of the porous medium. The total gas pressure, p_G is given by Darcy's law [78]

$$v_G = \frac{\sum_{i \neq s} M_i N_i}{\rho_G} = -\frac{k_G}{\mu_G} \nabla p_G \tag{2.43}$$

where v_G is the mass-average velocity of the gas phase, ρ_G is the density of the gas mixture, M_i is the molar mass of species i, N_i is the flux of species i, k_G is the gas permeability and μ_G is the dynamic viscosity of the gas mixture.

For the reactant gases and water vapor, the reaction term, R_i is zero in the GDL and the MPL. The water generated by oxygen reduction reaction is assumed to be in the vapor phase, the reaction term in eqn. [2.40] in the case of vapor transport in the aCL and cCL can therefore be given by

$$R_{H_2O}^{aCL} = 0 \tag{2.44}$$

and

$$R_{H_2O}^{cCL} = \frac{1}{2F} a_{12}^{o} i_{ORR} \tag{2.45}$$

respectively. The water produced by oxygen reduction reaction in the cCL is assumed to be in the vapor phase. For hydrogen gas transport in aCL, the reaction term is given by

$$R_{H_2}^{aCL} = -\frac{1}{2F} a_{12}^{o} i_{HOR} \tag{2.46}$$

because hydrogen is consumed by the hydrogen oxidation reaction that occurs in the aCL. Also, for oxygen transport in cCL, the reaction term is given by

$$R_{O_2}^{cCL} = -\frac{1}{4F} a_{12}^{o} i_{ORR} \tag{2.47}$$

because oxygen is consumed by the oxygen reduction reaction that occurs in the cCL.

2.3.3 Transport of Energy

The conservation of energy in the GDL, MPL, CL and membrane is governed by [58, 64]

$$-\nabla \bullet \left(-k_T^{eff} \nabla T \right) = S_T \tag{2.48}$$

where k_T^{eff} is the effective thermal conductivity of the system, T is the absolute temperature and S_T is the source term. The source term, S_T takes into account the joule heating and the heat of reaction. The heat of reaction is directly proportional to the entropy change for the reaction and the activation overpotential. Latent heat associated with phase change is not included in the source term, S_T because water is expected to be in the vapor phase only in HT-PEMFC. In the GDL and MPL, the source term, S_T is given by

$$S_T = \frac{i_1^2}{\sigma_s^{eff}} \tag{2.49}$$

where i_1 is the electronic current density and σ_s^{eff} is the electronic conductivity in the solid phase. The source term, S_T in the aCL is given by

$$S_T = \frac{i_1^2}{\sigma_s^{eff}} + \frac{i_2^2}{k_m^{eff}} + \eta_a a_{12}^{o} i_{HOR} \tag{2.50}$$

where i_2 is the ionic current density, η_a is the anode activation overpotential which is given by

$$\eta_a = (\phi_1 - \phi_2) \tag{251}$$

The source term, S_T in cCL is given by

$$S_T = \frac{i_1^2}{\sigma_s^{eff}} + \frac{i_2^2}{k_m^{eff}} + \left\{ \left| \frac{T\Delta S}{2F} \right| + \eta_c \right\} a_{12}^o i_{ORR} \tag{2.52}$$

where T is the absolute temperature, F is the Faraday constant, ΔS is the entropy change for the oxygen reduction reaction at the operating condition and is as given by [122]

$$\Delta S_T = -9967.35 \ln(T(K)) + 12414.83 \text{ J/(kmol•K)} \tag{2.53}$$

η_c in eqn. 2.52 is the cathode activation overpotential, and is given by

$$\eta_c = (\phi_1 - \phi_2 - U^\theta) \tag{2 .54}$$

where U^θ is the equilibrium potential and is as given in table IV. The source term in the membrane is given by

$$S_T = \frac{i_2^2}{k_m^{eff}} \tag{2.55}$$

The electrochemical and physical relationships used in this model are given in Table VI. Also, the parameters used in the model are given in Table VII.

2.3.4 Transport of Electric Charge

The charge transport equations used for the HT-PEMFC model are similar to those used in l ow temperature PEMFC model described in section 2.1.1. The major difference is that while agglomerate model in the cCL o f the low-temperature PEMFC model, effectiveness is assumed to be unity in the cCL of the HT-PEMFC model. To assess the effects of using the agglomerate model as o pposed to assuming that the effectiveness is unity, we compare a case w here agglomerate model is used in both cCL and aCL to that where effectiveness is assumed to be unity. The comparison is discussed

in the result section for the HT-PEMFC in chapter 5. We describe briefly here the derivation of the agglomerate model used in the aCL and cCL used for the comparison.

We recall that the current balance between the ionomer and the electronically conducting solid phase in the CL is given by:

$$\nabla \bullet i_2 = -\nabla \bullet i_1 = a_{1,2}^0 i_h (1-s) E \tag{2.56}$$

where E is the effectiveness factor and other variables are defined in section 2.1.1. As mentioned in section 2.1.1, the effectiveness factor is defined as [15, 28]:

$$E = \frac{1}{3\phi^2}\left(3\phi \coth\left(3\phi\right) - 1\right) \tag{2.57}$$

where ϕ is the Thiele modulus for the system and is defined as

$$\phi = \sqrt{\frac{R_{Agg}^2 k'}{\psi_{Agg}}} \tag{2.58}$$

where R_{Agg} is the agglomerate radius, ψ_{Agg} is the reactant gas permeation in the agglomerate and k' is the kinetic portion of the Thiele modulus and is given for ORR at the cCL as follows [28]:

$$k'_{ORR} = \frac{a_{1,2}^o i_{O_{ORR}}}{4F p_{O_2}^{ref} H_{O_2}} \exp\left(-\frac{\alpha_c F}{RT}\left(\phi_1 - \phi_2 - U^\theta\right)\right) \tag{2.59}$$

where $a_{1,2}^o$ is the specific surface area per unit volume between the ionomer and the electronically conducting solid phase in the cCL, $i_{O_{ORR}}$ is the exchange current density for the ORR, F is the Faraday constant, $p_{O_2}^{ref}$ is the reference partial pressure of oxygen in the cCL, H_{O_2} is the Henry's constant for oxygen in the phosphoric acid, α_c is the cathodic transfer coefficient, R is the gas constant, T is the absolute temperature, ϕ_1 is the potential in the solid phase, ϕ_2 is the potential in the ionic phase and U^θ is the reference potential for oxygen reduction with respect to a standard hydrogen reference electrode [28]. Also, the kinetic portion of the Thiele modulus, k'_{Agg} can be defined for the HOR as the aCL as follows:

$$k' = \frac{a_{1,2}^{o} i_{O_{HOR}}}{2Fp_{H_2}^{ref} H_{H_2}} \exp\left(\frac{\alpha_a F}{RT}\left(\phi_1 - \phi_2\right)\right) \tag{2.60}$$

where $i_{O_{HOR}}$ is the exchange current density for the HOR at the aCL, $p_{H_2}^{ref}$ is the reference partial pressure of hydrogen at the aCL, H_{H_2} is the Henry's constant for hydrogen in phosphoric acid and α_a is the anodic transfer coefficient. The diffusivity of oxygen gas in hot phosphoric acid, $\psi_{Agg}^{O_2}$ is used and is given as [100]

$$\psi_{Agg}^{O_2} = \exp\left(\begin{array}{l} \left(-9.21e5 w_{H_3PO_4}^3 + 2.47e6 w_{H_3PO_4}^2 - 2.21e6 w_{H_3PO_4} + 6.54e5\right)\frac{1}{T} \\ +\left(1.66e3 w_{H_3PO_4}^3 - 4.46e3 w_{H_3PO_4}^2 + 4.01e3 w_{H_3PO_4} + 1.21e3\right) \end{array} \right) \tag{2.61}$$

where $w_{H_3PO_4}$ is the mass fraction of phosphoric acid and is defined as

$$w_{H_3PO_4} = \frac{0.0544 x_{H_3PO_4}}{x_{H_3PO_4}\left(0.0544 - 0.01\right) + 0.01} \tag{262}$$

where $x_{H_3PO_4}$ is the mole fraction of phosphoric acid and is defined as

$$x_{H_3PO_4} = \frac{\ln\left(p_{H_2O}\right) + \frac{2765.1}{T} - 22.002}{\frac{-4121.9}{T} + 2.5929} \tag{263}$$

where p_{H_2O} is the partial pressure of water. The henry's constant for oxygen in hot phosphoric acid is used and is given as [100]

$$H_{O_2} = \exp\left(\left(-1.27e4 w_{H_3PO_4} + 1.23e4\right)\frac{1}{T} + \left(35.2 w_{H_3PO_4} - 46.6\right)\right) \tag{2.64}$$

The diffusivity of hydrogen and the henry's constant of hydrogen in phosphoric acid are related that of oxygen due to lack of experimental data. We use the same relation that was assumed by Sousa et al. [100]

$$H_{H_2} = 4H_{O_2} \tag{2.65}$$

$$\psi_{Agg}^{H_2} = 2\psi_{Agg}^{O_2} \tag{2.66}$$

Description	***Expression***

Equilibrium Potential, U^{θ}	$U^{\theta} = 4.1868\left(\frac{70650 + 8T\ln T - 92.84T}{2F}\right)V$ [10]
Surface area per unit of mass of individual spherical Pt particle	$s_{Pt} = \frac{3}{\left(\rho_{Pt} r_{Pt}\right)}$ where mean Pt radius, $r_{Pt} = 2.01\text{e-}7\text{cm}$ [100]
Specific Pt surface area per unit CL volume for anode	$a_{Pt}^{ano} = \frac{L_{Pt}^{ano} s_{Pt}}{\delta_{CL}}$ where δ_{CL} is the thickness of the CL
Specific Pt surface area per unit CL volume for cathode	$a_{Pt}^{cat} = \frac{L_{Pt}^{cat} s_{Pt}}{\delta_{CL}}$ where δ_{CL} is the thickness of the CL
Anodic exchange current density	$i_o^{ano} = 0.072\exp\left[\frac{16900}{R}\left(\frac{1}{433.15} - \frac{1}{T(K)}\right)\right]$ [101, 122]
Cathodic exchange current density	$i_o^{cat} = 1.3150\text{e-}8\exp\left[\frac{72400}{R}\left(\frac{1}{423.15} - \frac{1}{T(K)}\right)\right]$ [101, 122]
PBI membrane conductivity	$k_m = \frac{ab}{T}\exp\left(-\frac{E_a}{RT}\right)$ $E_a = -619.6DL + 21750\text{Jmol}^{-1}$ $a = 168DL^3 - 6324DL^2 + 65750DL + 8460$ $b = \begin{cases} 1 + \left(0.01704T - 4.767\right)RH^{eff} & \text{if } 373.15K \le T \le 413.15K \\ 1 + \left(0.1432T - 56.89\right)RH^{eff} & \text{if } 413.15K < T \le 453.15K \\ 1 + \left(0.7T - 309.2\right)RH^{eff} & \text{if } 453.15 < T \le 473.15K \end{cases}$ $RH^{eff} = \begin{cases} RH & \text{in CL} \\ RH_{avg} & \text{in membrane} \end{cases}$ [102]

P_{sat} (range 100 and 200°C)	$p_{sat} = 0.68737T^3(K) - 732.39T^2(K) + 263390T(K) - 31919000$ Pa [102]

Table VI: Electrochemical and physical relationships

Parameters	***Values***
Anode GDL/MPL porosity	$e_{aGDL} / e_{aMPL} = 0.6 / 0.3$
Anode CL porosity	$e_{aCL} = 0.3$
Anode CL ionomer volume fraction	$e_{iaCL} = 0.3$
Cathode CL porosity	$e_{CCL} = 0.3$
Cathode CL ionomer volume fraction	$e_{iCCL} = 0.3$
Cathode GDL/MPL porosity	$e_{cGDL} / e_{cMPL} = 0.6 / 0.3$
Mean pore diameter of GDL/MPL	$d_{GDL} / d_{MPL} = 20 / 0.06\mu m$ [120]
Mean pore diameter of CL	$d_{CL} = 0.08\mu m$ [11]
Cathodic transfer coefficient for anode	$\alpha_c^a = 0.5$ [101]
Anodic transfer coefficient for anode	$\alpha_a^a = 0.5$ [101]
Cathodic transfer	$\alpha_c^c = 1$

coefficient for cathode	
Reference partial pressure of O_2	$p_{H_2ref} = 1.01325\text{bar}$
Reference partial pressure of H_2	$p_{O_2ref} = 1.01325\text{bar}$
Cathode CL Pt loading	$L_{Pt}^{cat} = 0.4\text{e-}3\text{g/cm}^2$
Anode CL Pt loading	$L_{Pt}^{ano} = 0.2\text{e-}3\text{g/cm}^2$
Density of Pt	$\rho_{Pt} = 21.45\text{g/cm}^3$
Electronic conductivity	$\sigma_s = 7\text{S/cm}$
Gas permeability CL/MPL/GDL	$k_{per}^{CL} / k_{per}^{MPL} / k_{per}^{GDL} = 1e-10\text{cm}^{-2} / 5e-10\text{cm}^{-2} / 1e-8\text{cm}^{-2}$

Table VII: Parameters used in the model

2.3.5 Boundary Conditions

The boundary conditions used in the model are summarized in Table VIII. In this model, it is assumed that both the relative humidity and the operating temperature at the interface between the gas channel and the gas diffusion layer are fixed. Because the acid-doped PBI membrane is assumed to be impermeable to the gases, the flux of reactant gases and vapor is assumed to be zero at the interface between the bulk membrane and the catalyst layer.

Variables	***aGC/aGDL***	***aGDL/aCL***	***aCL/Mem***	***Mem/CCL***	***CCL/CGDL***	***CGDL/CGC***
p_G	$p_G = p_0 + p_{H_2}$					$p_G = p_0 + p_{O_2}$
p_0	p_0 given					p_0 given

p_{H_2}	p_{H_2} given				
p_{O_2}					p_{O_2} given
N_0			$N_0 = 0$	$N_0 = 0$	
N_{H_2}			$N_{H_2} = 0$	$N_{H_2} = 0$	
N_{O_2}			$N_{O_2} = 0$	$N_{O_2} = 0$	
i_1			$i_1 = 0$	$i_1 = 0$	
i_2		$i_2 = 0$		$i_2 = 0$	
ϕ_1	$\phi_1 = 0$				$\phi_1 = V_{cell}$
ϕ_2		$\frac{\partial \phi_2}{\partial y} = 0$			
T	T given				T given

Table VIII: Summary of the boundary conditions

2.6 NUMERICAL IMPLEMENTATION

The governing equations are solved using a control-volume approach. The same approach was used by Weber and Newman [53] in their modeling work. The domain of interest is discretized into finite elements or boxes and the governing equations are also cast into finite-difference form. The flux density leaving the left-side half box is set equal to that entering the right-side half box, so that the material is rigorously conserved. In this technique, all vectors are defined at half-mesh points, while the scalars are defined at full-mesh points. Figure 2.2 illustrates the numerical approach used in this work. All reaction terms are evaluated at quarter-mesh points. The coupled differential equations are solved using a MATLAB® implementation of the Newman BAND (J) sub-function. The Newwan BAND sub-function solves the coupled non-linear differential equations iteratively using Newton-Raphson method. If we represent the systems of equations described above as

$$F_i\left(x_1,\ x_2,...,\ x_N\right)=0 \qquad i=1,\ 2,\ ...,\ \mathrm{N} \tag{2.67}$$

The equations can be expanded using Taylor series. If we neglect second and higher order terms, we can write the Taylor expansion of the systems of equation as follows:

$$F_i(x+\delta x)=F_i(x)+\sum_{j=1}^{N}\frac{\partial F_i}{\partial x_j}\delta x_j+0\left(\delta x^2\right) \tag{2.68}$$

The derivatives of the systems of equation with respect to the independent variables form a Jacobian matrix, *J(x)* which can be written as

$$J(x)=\begin{bmatrix} \dfrac{\partial F_1(x)}{\partial x_1} & \cdots & \dfrac{\partial F_1(x)}{\partial x_N} \\ \vdots & \ddots & \vdots \\ \dfrac{\partial F_N(x)}{\partial x_1} & \cdots & \dfrac{\partial F_N(x)}{\partial x_N} \end{bmatrix} \tag{2.69}$$

We can therefore write the iterative functions for the systems of equations as follows

$$\delta x^k=-J(x^k)^{-1}F(x^k) \tag{2.70}$$

The iteration process continues until the change variable, δx is less than the specified tolerance.

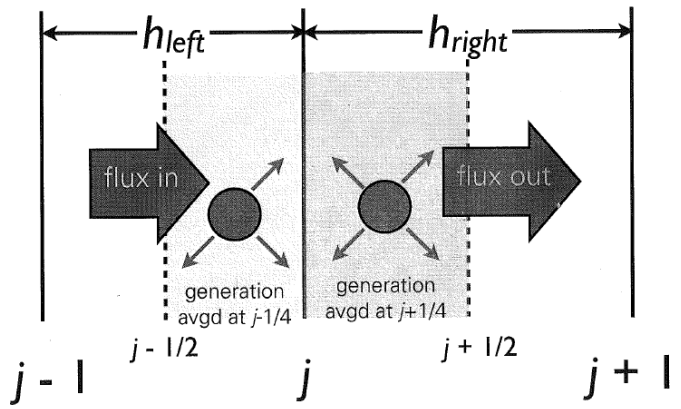

Figure 2.2: Schematic diagram illustrating the numerical implementation

The time dependent variables are solved using Crank-Nicolson method. To illustrate the Crank-Nicolson method, consider the following partial differential equation with dependent variable, *u* and independent variables, *t* and *x*.

$$\frac{\partial u}{\partial t} = D\frac{\partial^2 u}{\partial x^2} \tag{2 .71}$$

using Crank-Nicolson method, we can discretize eqn 2.71 as follows

$$\frac{u_i^{n+1} - u_i^n}{\Delta t} = \frac{1}{2}\left\{\left[D_i \frac{u_{i+1} - 2u_i + u_{i-1}}{(\Delta x)^2} \right]^{n+1} + \left[D_i \frac{u_{i+1} - 2u_i + u_{i-1}}{(\Delta x)^2} \right]^{n} \right\} \tag{2.72}$$

where *n* is the current time step, *i* is the mesh point, Δt is the time step size and Δx is the spatial step s ize. To reduce the computational time, we use adaptive time step in this work. We started with a time step size of 0.5s and after 2s, we increase the time step size to 1s. In order to prevent the code from diverging, we put both lower and upper bounds on the size of the change variables during the iterative process.

Chapter 3: Result and Discussions Part 1: Modeling Transient Response of Proton-Exchange Membrane Fuel Cell under Load Change

The developed model will be used to predict fuel cell transients, in particular the response of fuel cell operation to step transients in current/voltage. These results are compared against fuel cell experimental results, which stepped operating current up and down between 0.01 A/cm^2 and 0.68 A/cm^2. The model simulates these step transients in current by stepping the voltage (due to mathematical ease) from 0.8 V to 0.5 V and vice versa. Figure 3.1 shows the current density in the bulk membrane for Nafion®112, 115 and 117 when the voltage is stepped up from 0.5V to 0.8V at 0s and back to 0.5V at 800s. As will be shown later, since the ionic resistance in the membrane decreases as the thickness of the membrane decreases, the current density in the membrane increases as the thickness of the membrane decreases as shown in figure 3.1.

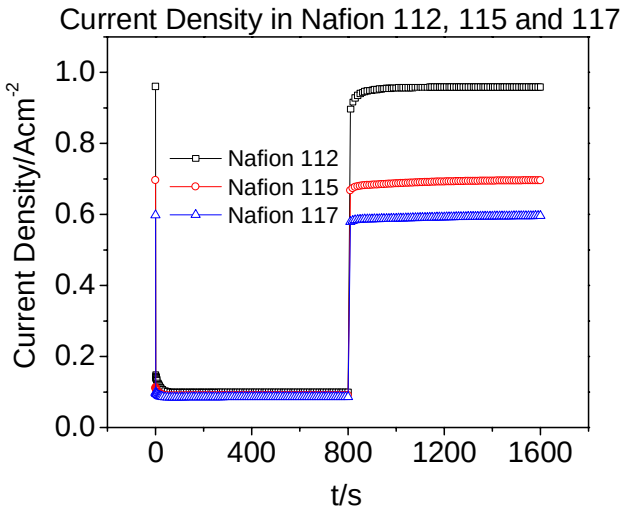

Figure 3.1: Current density in Nafion® 112, 115 117 for step change in voltage (T = 80 ^oC, P = 1bar, RH_a/RH_c = 100%/100%, 0.5V to 0.8V from t = 0 to 800s and 0.8V to 0.5V from 800s to 1600s).

As recognized by Gostick et al.[81], secondary injection capillary pressure is likely to be relevant to fuel cell operation because the pores in GDL are likely to be partially wet by vapor condensation before any liquid water is formed in the pores. We therefore use secondary injection capillary pressure relation when the voltage is stepped down and primary withdrawal capillary pressure relations when the voltage is stepped up for the cases where the hysteresis in capillary pressure-saturation relation is considered. Similarly, we use secondary injection capillary pressure relation for when voltage is stepped up or down when we neglect the hysteresis in the capillary pressure-saturation relation.

In all the cases considered, the initial condition is the steady state at the starting condition. For the cases where the hysteresis in capillary pressure relation is considered, when voltage is stepped down, the initial condition is computed using primary withdrawal capillary pressure. Also, when voltage is stepped up, the initial condition is computed using secondary injection capillary pressure.

In this section of the dissertation, we include the hysteresis effect in the capillary pressure-saturation relation as the base case. We investigate the effect of including the hysteresis effect in the model. As shown in figure 3.2, the effect of including the hysteresis on both the water content in the bulk membrane and the liquid water saturation is minimal. The result agrees with what was suggested by Weber [83], that the effect of hysteresis is not expected to be significant. However, both experimental observation and model predictions show that net flux of liquid water is into the GDL and CL when the current density is increased, that is, more liquid water accumulates in the GDL and CL while the net flux of liquid water is out of the GDL and CL when the current density is decreased as more water moves by capillary action towards the gas channel.

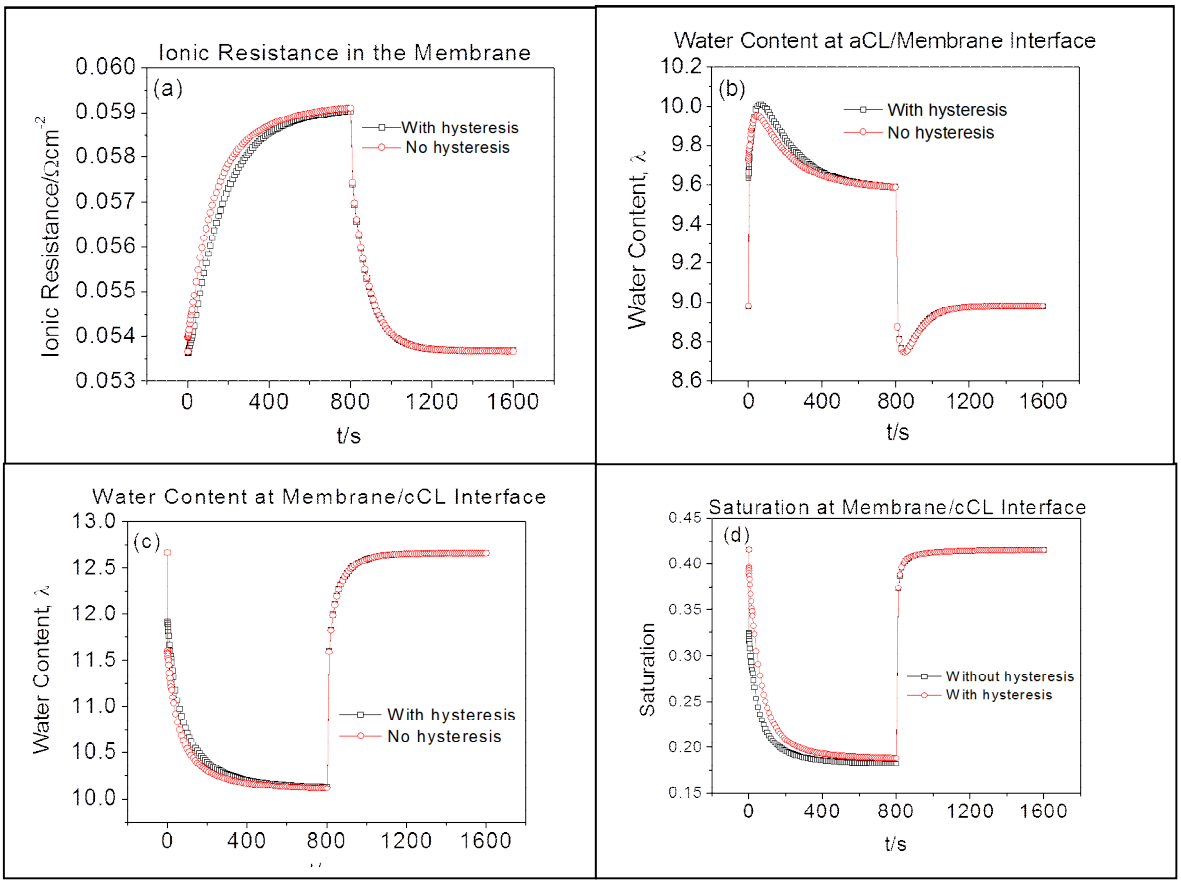

Figure 3.2: The effect of the hysteresis observed in the capillary pressure-saturation relation (a) ionic resistance in the bulk membrane during step change in voltage, (b) water content at aCL/membrane interface during step change in voltage, (c) water content at membrane/cCL interface during step change in voltage, (d) liquid water saturation at membrane/cCL interface during step change in voltage. ($T = 80\,^{o}C$, P = 1bar, RH_a/RH_c = 100%/100%, 0.5V to 0.8V from t = 0 to 800s and 0.8V to 0.5V from 800s to 1600s, Nafion® 112).

For instance, figure 3.2d shows that the liquid water saturation in the cCL decreases until steady state is reached when the voltage is increased; Figure 3.2d also shows that the saturation increases when the voltage is decreased. While including the hysteresis effect seems appropriate, its effect on modeling results is negligible under all of the experiments that we simulated. We conclude that one should still get good

modeling prediction of transient behavior in PEMFC by using only the secondary injection capillary pressure relation in transient modeling.

The High Frequency Resistance (HFR) measurement conducted at Los Alamos National Laboratory (LANL) shows that the time constant for the membrane hydration when current is increased is shorter than that of membrane dehydration when current is decreased, as shown in Figure 3.3 [123]. In these experiments, the MEA used was a Gore™ Primea® MEA Series 57 with 18 µm thick GORE-SELECT® membrane and carbon supported 0.2 mg Pt cm^{-2} on the cathode and 0.1 mg Pt cm^{-2} on the anode. See Davey et al. [123] for details on experimental procedures.

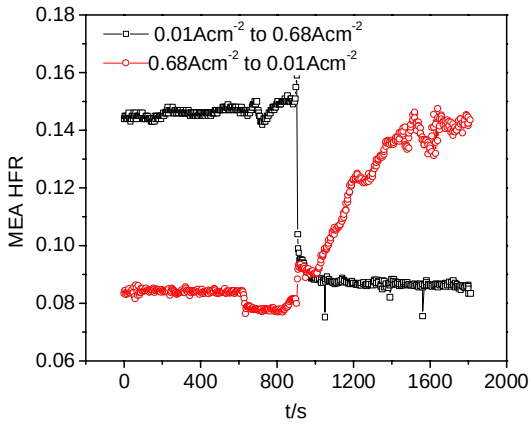

Figure 3.3: MEA High-Frequency Resistance (18 µm thick GORE-SELECT® membrane, aCL/cCL thickness = 4.5µm/9µm, GDL thickness = 200µm macro-GDL and 50µm MPL, T = 80 ° C).

We attempted to simulate these experiments with the model; the results are shown in Figure 3.3. For the runs shown in Figure 3.3, the relative humidity of the anode inlet gas is 100%, while that of the cathode gas is 50%. Other researchers have also witnessed different time constants for the evolution of the impedance response for increasing and decreasing current steps. Wu et al. [71] found that the membrane hydrates faster when the

relative humidity is increased compared to how fast it dehydrates when the relative humidity is decreased. They suggested that this is due to non-linear diffusion in the membrane. Wang and Wang [74] increased cathode relative humidity from 0% to 100% for different cell voltage and found that the time constant for membrane hydration increases as voltage increases. However, when the cathode relative humidity is decreased from 100% to 0%, they found the dehydration time to be shorter for a cell with higher voltage.

In this dissertation we provide an explanation for the difference in time constant in membrane hydration and dehydration when voltage is stepped down and up respectively. Figure 3.4a shows calculated water content profiles of Nafion® 112 when the voltage is stepped down from 0.8V to 0.5V as a function of time while figure 3.4b shows the calculated water content profiles of Nafion® 112 when the voltage is stepped up from 0.5V to 0.8V. On the x-axis, the first 20μm and the last 20μm represent the water content in the ionomer of aCL and cCL respectively while the water content in between them is that of the bulk membrane. For ease of comparison, the water content profile in Figure 3.4 is shown up to 140s. In this macroscopic model, the governing equation for ionomer water transport in catalyst layer is the same as that in the bulk membrane, except that the volume fraction of ionomer in the bulk membrane is assumed to be unity. This approach is based on the fact that there should be a continuous path for hydrogen ions to travel from aCL through the membrane to cCL. Similar to the HFR measurement shown in Figure 3.4, the water content, λ increases more rapidly when the voltage is decreased compared to when it is increased. The water content profile reaches steady state at round 120s when the voltage is decreased, though it is still decreasing at 140s when the voltage is increased.

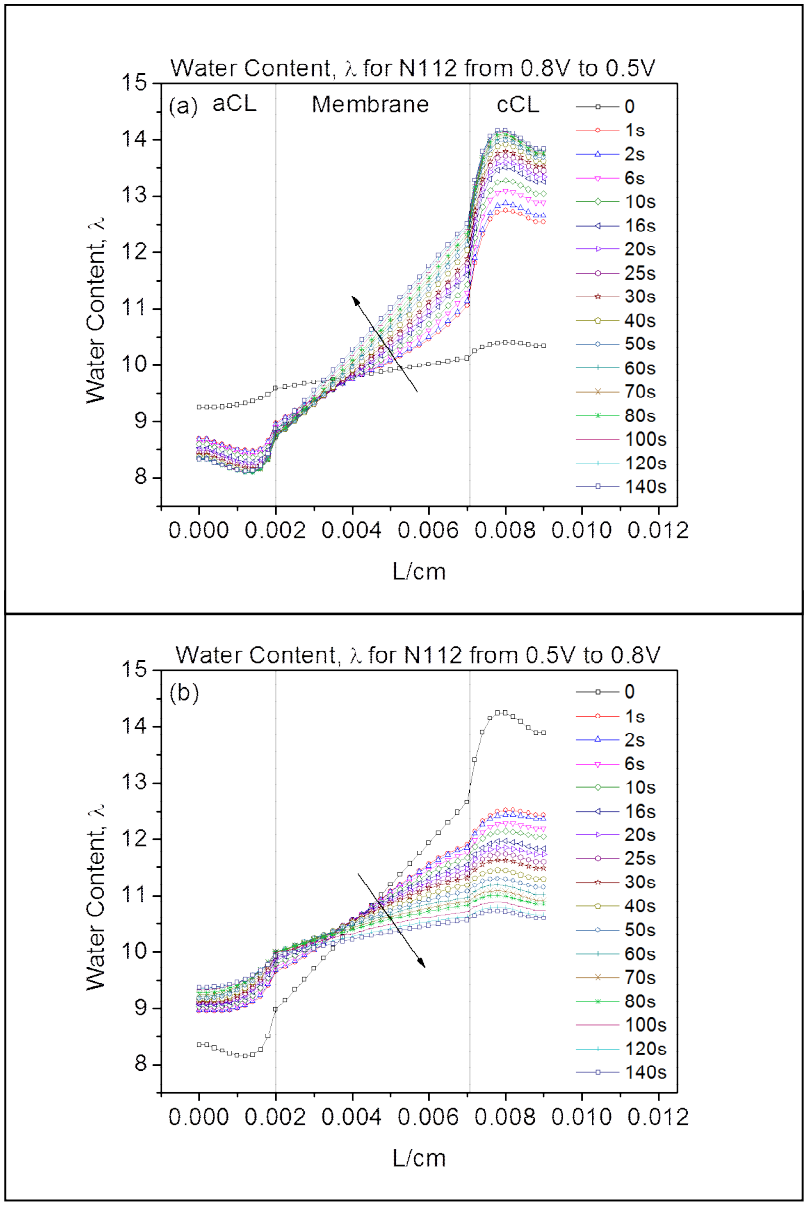

Figure 3.4: The plot of water content of Nafion® 112 for when voltage is stepped up from 0.5V to 0.8V and vice versa (T = 80 ^{o}C , P = 1bar, RHa/RHc = 100%/100%).

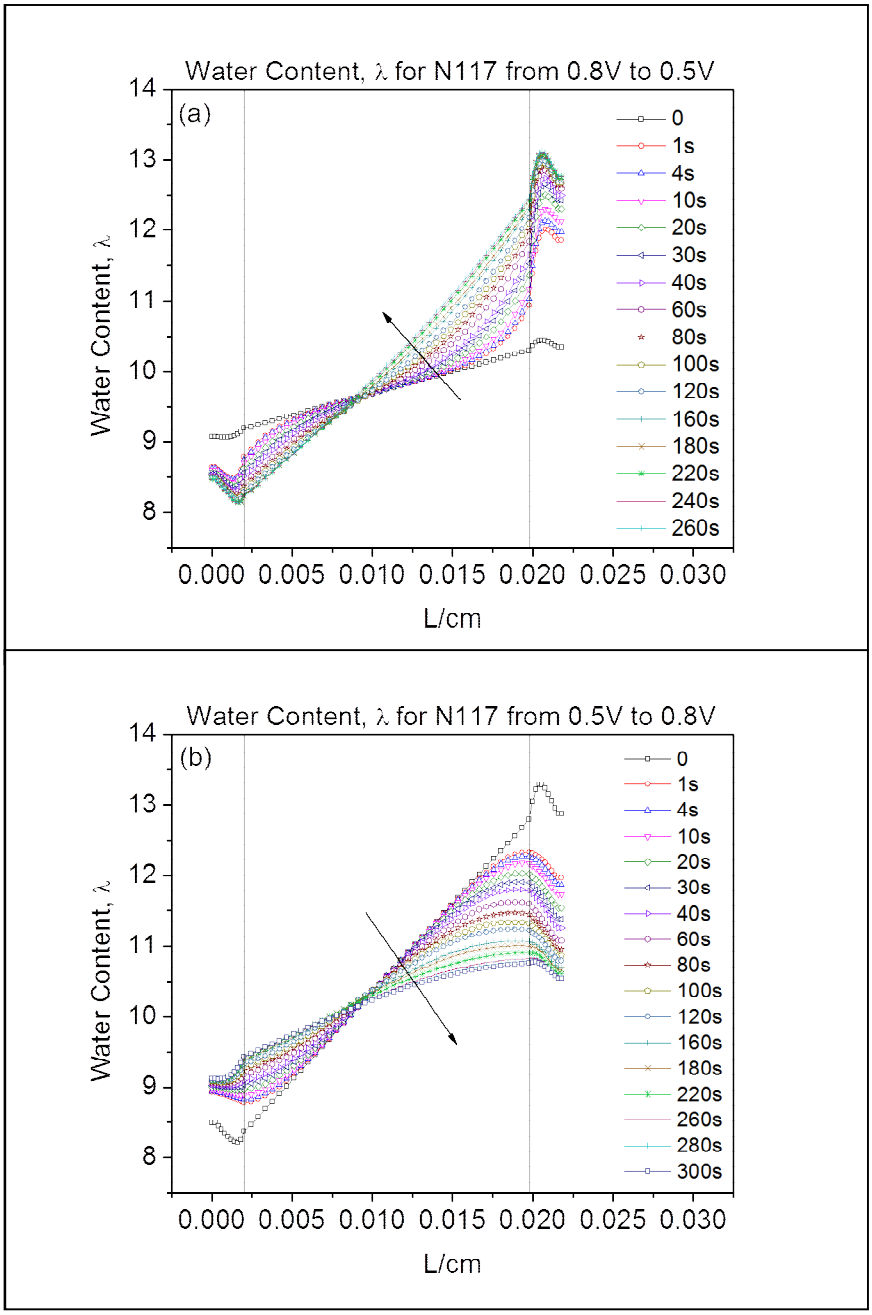

Figure 3.5: The plot of water content of Nafion® 112 for when voltage is stepped up from 0.5V to 0.8V and vice versa (T = 80 ^{o}C , P = 1bar, RH_a/RH_c = 100%/100%).

Figure 3.5a shows water content profiles of Nafion® 117 when the voltage is stepped down from 0.8V to 0.5V while figure 3.5b shows the water content profiles of Nafion® 117 when the voltage is stepped up from 0.5V to 0.8V. The first 20μm and the last 20μm on the x-axis in Figure 3.5 also represent the water content in the ionomer of aCL and cCL respectively while the water content in between them is that of the bulk membrane. The water content profile when the voltage is decreased from 0.8V to 0.5V is shown up to 260s while the water content profile when the voltage is increased from 0.5V to 0.8V is shown up to 300s. Similar to the Nafion® 112 water content profile in Figure 3.4, the water content profile in Figure 3.5 increases more rapidly when the voltage is decreased compared to when it is increased. However, the hydration and dehydration time for Nafion® 112 was shorter than that of Nafion® 117.

Also, unlike Nafion®112 where the water content of the ionomer in the CL reaches steady state almost at the same time as the water content in the bulk membrane, the water content of the ionomer in the CL in the case of Nafion® 117 reaches steady state faster than the water content in the bulk membrane. For instance, when the voltage is decreased, the water content in the ionomer of cCL is at steady state at around 140s, while the water content in the bulk membrane does not reach steady state until around 260s.

Similarly, when the voltage is increased, the water content in the ionomer of cCL reaches steady state around 220s while the water content in the bulk membrane is still decreasing at 300s. The difference in the time to reach steady state between the ionomer in CL and the bulk membrane can be partly accounted for by the time for the water to diffusion across the membrane. For Nafion® 117 and $\lambda = 10$, the time constant, $\tau_{m,D}$ for water diffusion across the membrane can be estimated as $\tau_{m,D} = \delta_m^2 / D_\lambda^{eff} \approx 45s$ while in the case of Nafion® 112 and $\lambda = 10$, $\tau_{m,D} = \delta_m^2 / D_\lambda^{eff} \approx 3.5s$. It takes only around 3.5s for

water to diffuse through Nafion® 112 which is 50µm thick while it takes around 45s for water to diffuse through Nafion® 117 which is 177.8µm thick. Because the water diffuses through the thinner membrane faster, the water content in the thinner membrane reaches steady state faster than the thicker one.

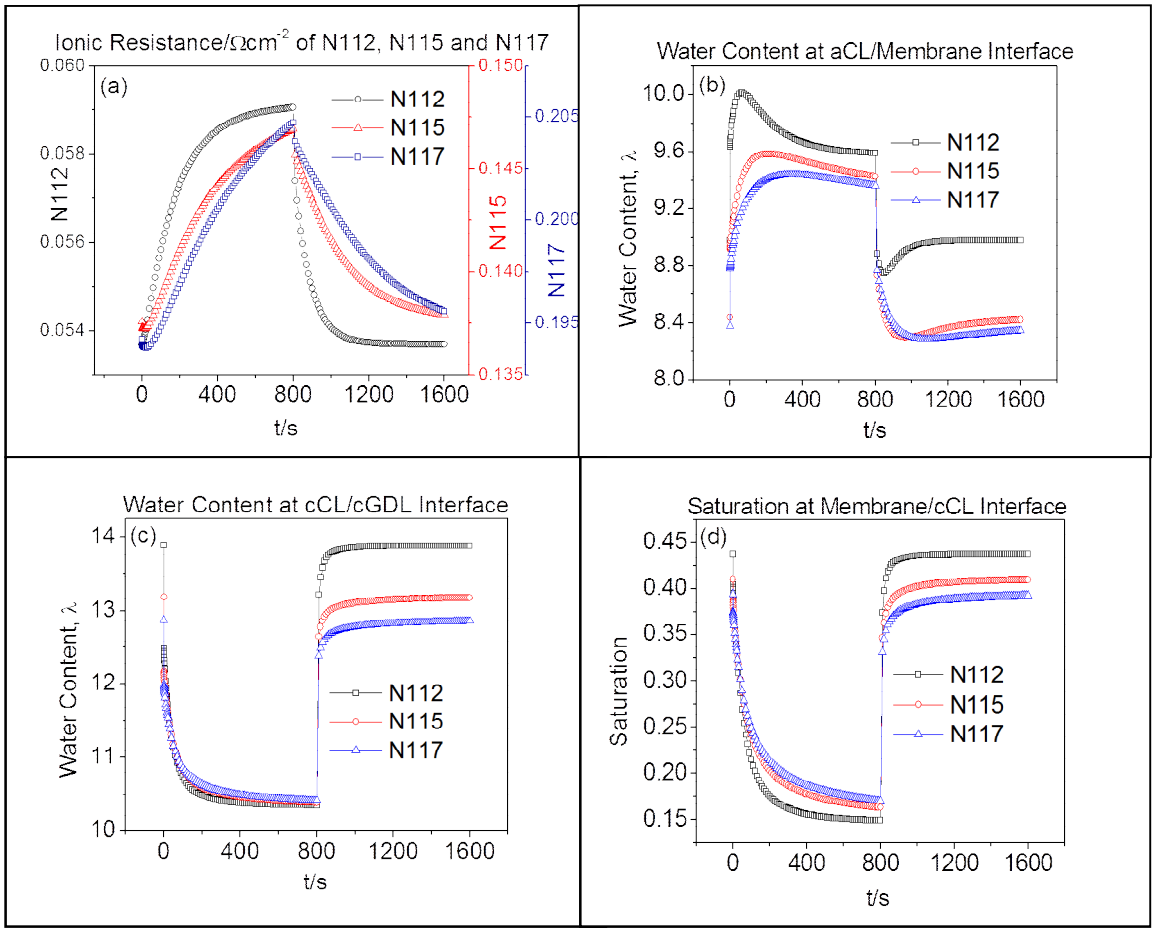

Figure 3.6: Comparison of ionic resistance, water content and saturation for Nafion® 112, 115 and 117 (a) ionic resistance in the bulk membrane during step change in voltage, (b) water content at aCL/membrane interface during step change in voltage, (c) water content at cCL/cGDL interface during step change in voltage, (d) liquid water saturation at membrane/cCL interface during step change in voltage ($T = 80\,^{o}C$, P = 1bar, RH_a/RH_c = 100%/100%, 0.5V to 0.8V from t = 0 to 800s and 0.8V to 0.5V from 800s to 1600s).

Figure 3.6 shows the comparison of the ionic resistance in the bulk membrane, water content at the membrane interface and liquid water saturation at the cathode side interface for Nafion® 112, 115 and 117 when voltage is stepped up from 0.5V to 0.8V and then back to 0.5V after 800s. The ionic resistance R in Figure 3.6a is computed as:

$$R = \frac{\Delta\phi_2}{I_2} \qquad (3.1)$$

where $\Delta\phi_2$ and I_2 are the potential drop and the ionic current density in the membrane respectively. Figure 3.6a shows that the ionic resistance in the membrane increases as the thickness of the membrane increases. Similar to the experimental observation shown in Figure 3.3, the ionic resistance decreases faster when the voltage is decreased compared to how fast it increases when the voltage is increased. Comparing the experimental measurement where 18μm Gore-select membrane is used to the modeling result where Nafion®112 is used, MEA hydration and dehydration in the HFR experiment take 100s and 550s respectively while MEA hydration and dehydration in the model with Nafion®112 take 250s and more than 600s respectively. It should be noted that Nafion® 112 used in the model is more than two times thicker than 18μm Gore-select membrane used in the experiment and we have shown that thinner membrane has shorter diffusion time constant compared to thicker membrane. This explains why the hydration and dehydration time constants in Nafion® 112 are longer than that of 18μm Gore-select membrane. While the membrane thickness explains why the hydration and the dehydration time constants for Nafion® 112 are longer than that of 18μm Gore-select membrane, the difference in the hydration time constants between the two membranes seems larger than the difference in the dehydration time constant between the two membranes. We suggest that this is due to the different dominant factors determining the hydration and dehydration time constants. While the time constant for membrane

hydration is mainly determined by the rate of water generation and how fast water diffuses across the membrane, the time constant for membrane dehydration is mainly determined by how fast water diffuses across the membrane and how fast water (either vapor or liquid) equilibrating with the membrane reaches steady state.

In Figure 3.6b, when the voltage is stepped up from 0.5V to 0.8V at 0s, the water content at the anode side of the membrane increases with an overshoot. The peak of the overshoot occurs first in Nafion® 112, followed by Nafion® 115 and then by Nafion® 117. When the voltage is stepped up, current decreases and less water is dragged from anode to cathode. However, water produced at the cCL before the voltage is stepped up continues to diffuse to the anode. Because back diffusion of water to the anode is more than that of the electro-osmotic drag, the water content at the anode increases until it reaches peak value. Electro-osmotic drag balances back diffusion when the water content reaches the peak value. The water content at the anode decreases after reaching the peak value because the amount of water dragged from anode with hydrogen ion becomes greater than the amount of water that diffuses back to the anode. The water content at the anode reaches peak value in thinner membranes first because water diffuses faster in these membranes.

After 800s, the voltage is stepped down and the current density increases as shown Figure 3.6. Because of the increase in current density, more water is dragged from anode to cathode and the water content at the anode side of the membrane decreases with an undershoot as shown in the second half of Figure 3.6b. We observe an undershoot because of the increased electro-osmotic drag when the voltage is stepped up. The water content reaches the lowest value when the back-diffusion of water balances that of the electro-osmotic drag. The water content at the anode rises slightly because more water continues to diffuse back to the anode.

Also in Figure 3.6 (b&c), it can be seen that more water diffuses back to the anode in Nafion® 112 when the voltage is increased because of its smaller thickness compared to Nafion® 115 and 117. Similarly, more water is dragged from anode to cathode in Nafion® 112 when the voltage is decreased because of its lower ionic resistance compared to Nafion® 115 and 117. The water content at the cathode side of Nafion® 112 reaches steady state faster than the water content in Nafion® 115 and 117, especially when the voltage is decreased. The trend of saturation at the cathode side of the membrane is essentially the same as that of water content at the membrane side. The time it takes the saturation at the cathode side to reach steady state when the voltage is increased is longer than when the voltage is decreased. The saturation at the cathode side of Nafion® 112 decreases more compared to that of Nafion® 115 and 117 when the voltage is increased. Also, the saturation at the cathode side of Nafion® 112 increases more compared to that of Nafion® 115 and 117 when the voltage is decreased.

In Figure 3.6 (c & d), we have seen that both the water content and the saturation at the cathode side of the membrane follow similar trend. In Figure 3.7 (a & b), we explore further the relationship between the various phases of water at both membrane anode and cathode interfaces respectively. In all the cases considered, the modeling results only show liquid water at the cathode side of the membrane. At the anode side in Figure 3.7a, where there is no liquid water, the water content and the vapor pressure follow a similar trend. When the voltage is increased, they both increase rapidly to the peak values and then decrease before reaching the steady state. Also, when the voltage is decreased, both the water content and the vapor pressure decrease rapidly until they reach minimum values, after which they both increase before reaching the steady state.

However, at the cathode side in Figure 3.7b where there is liquid water, the vapor pressure decreases instantaneously when the voltage is increased, while the water content

and the liquid water saturation decrease rapidly at first and then slowly until the steady state is reached. When the voltage is decreased, the vapor pressure at the cathode side increases instantaneously while the water content and saturation increases rapidly at first and they slowly until they reach steady state. Also, because there is liquid at the cCL, the absorption and desorption of water in the membrane phase is determined by the fraction of the pores in the cCL that is filled with liquid water as the vapor pressure is already saturated. Therefore, how quickly liquid water in the CL pores is removed determines how fast the water content and hence the ionic resistance in the membrane reaches steady state. The water content in the membrane will not reach steady state as long as the water in contact with the membrane, which can be water vapor or liquid water, is not at steady state.

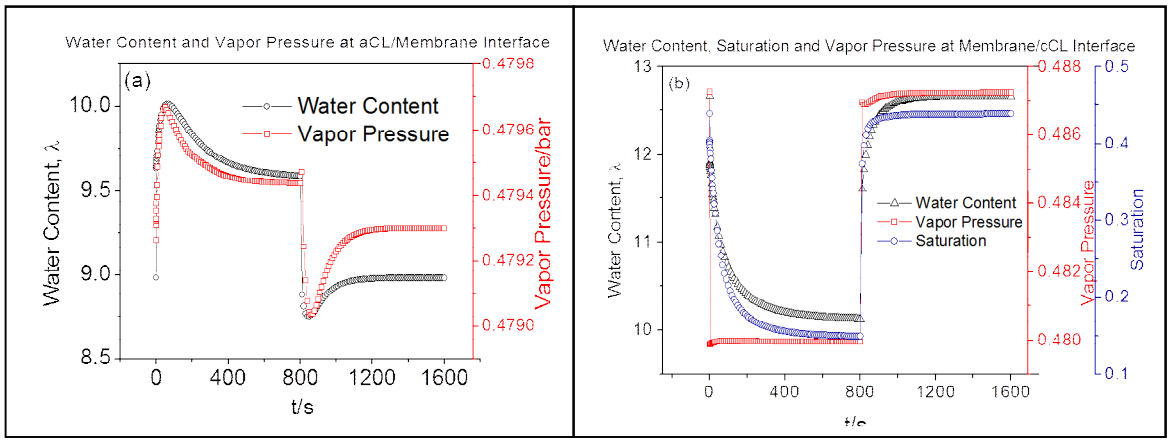

Figure 3.7: Comparison of various water phases at membrane interface (T = 80 ^{o}C, P = 1bar, RH_a/RH_c = 100%/100%, 0.5V to 0.8V from t = 0 to 800s and 0.8V to 0.5V from 800s to 1600s, Nafion® 112).

The current density profiles for Nafion® 112, 115 and 117 under the operating conditions used in Figures 3.6 and 3.7 are shown in figure 3.1. The current density

increases as the thickness of the membrane decreases because the ionic resistance in the membrane increases with membrane thickness.

3.1 THE EFFECTS OF DIFFERENT CL CAPILLARY PRESSURE

In this dissertation, we choose as our base case CL capillary pressure to be 1.3 times that of the GDL for both secondary injection and primary withdrawal. Here, we look at how different CL capillary pressure affects the cCL liquid water saturation, water content and hence the ionic resistance in the membrane. We consider two cases: when CL capillary pressure is 1.3 of GDL capillary pressure (CL is more hydrophobic during injection but more hydrophilic during withdrawal) and when CL capillary pressure is 0.8 of GDL capillary pressure (CL is more hydrophilic during injection but more hydrophobic during withdrawal). We should mention that because of the discontinuity in liquid water saturation that occurs when two media of different capillary properties are brought in contact, capillary pressure is continuous at the interface between CL and GDL.

Figure 3.8 shows the ionic resistance in the membrane, the water content at both anode and cathode interfaces of the membrane and the saturation at the cathode interface of the membrane for the two cases of CL capillary pressure considered. Figure 3.8(a) shows that the ionic resistance when CL capillary pressure is 1.3 of GDL capillary pressure is higher than when CL capillary pressure is 0.8 of GDL capillary pressure. The effects of hydrophobicity of CL seem to be more pronounced during injection. The decrease in water content and in liquid water saturation as a result of increasing the hydrophobicity of CL is small during withdrawal compared to that of injection. The case when CL is more hydrophilic during injection has more water content, more liquid water saturation and lower ionic resistance. In the two cases, the time scale for membrane hydration is smaller than that of membrane dehydration. As mentioned earlier, it is

important that more research work be done to determined how CL behaves during liquid water imbibition and withdrawal and also to determine a precise relationship between CL capillary pressure and liquid water saturation.

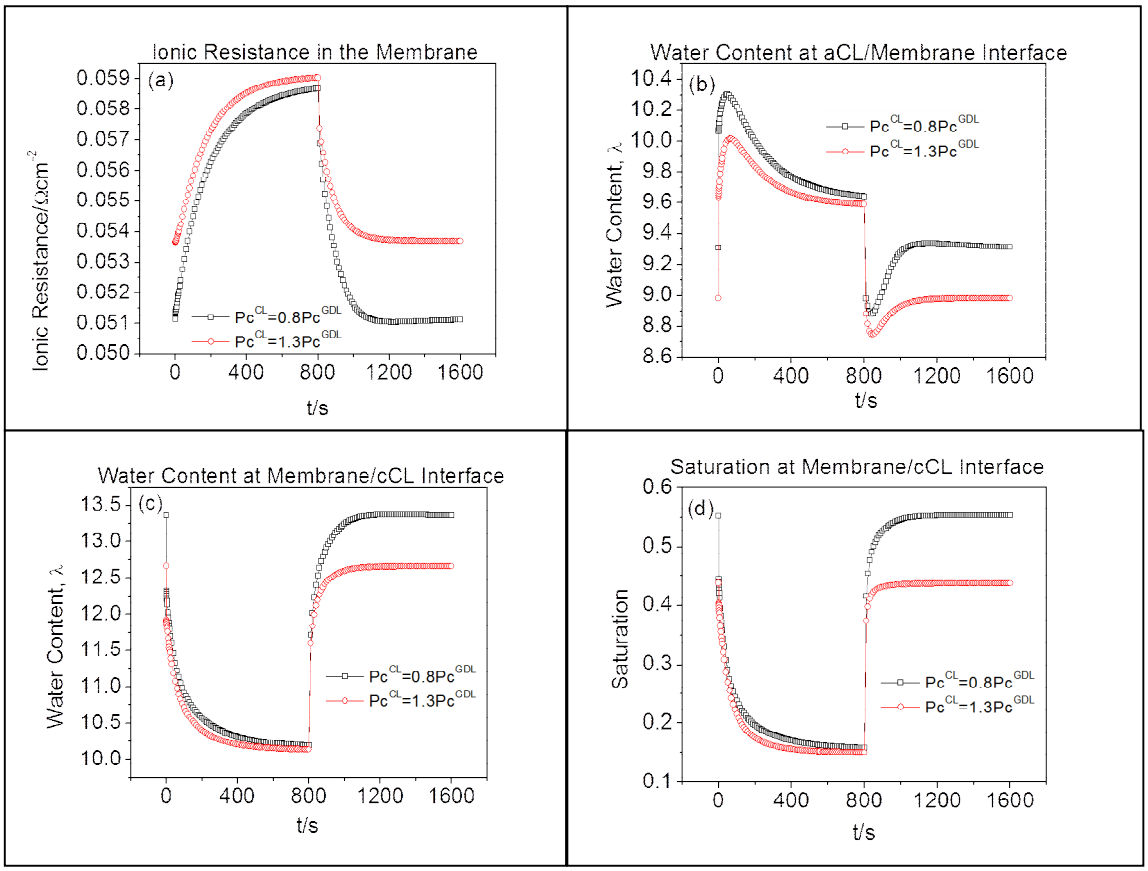

Figure 3.8: Comparison of ionic resistance, water content and saturation for different CL capillary pressure (a) ionic resistance in the bulk membrane during step change in voltage, (b) water content at aCL/membrane interface during step change in voltage, (c) water content at membrane/cCL interface during step change in voltage, (d) liquid water saturation at membrane/cCL interface during step change in voltage. ($T = 80\,^{o}C$, P = 1bar, RH_a/RH_c = 100%/100%, 0.5V to 0.8V from t = 0 to 800s and 0.8V to 0.5V from 800s to 1600s, Nafion® 112).

From Figure 3.8(d), as the hydrophobicity of CL increases during injection, the liquid water saturation in the CL pores goes down at the expense of increased ionic resistance in the membrane. Liquid water saturation in the CL can be reduced by making CL more hydrophobic and this could be accomplished by PTFE addition as suggested by [61]. However, increasing the PTFE content in the CL decreases the proton conductivity. There is therefore a performance trade-off between the increase in oxygen diffusion resulted from decreased liquid water saturation and the decrease in proton conductivity by making CL more hydrophobic.

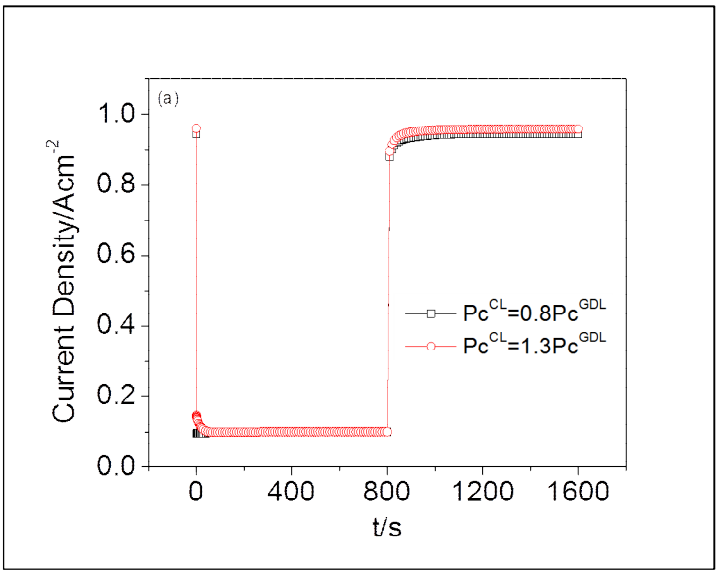

Figure 3.9: Current density profiles for different CL capillary pressure during step change in voltage. ($T = 80^{o}C$, P = 1bar, RH_a/RH_c = 100%/100%, 0.5V to 0.8V from t = 0 to 800s and 0.8V to 0.5V from 800s to 1600s).

Shown in Figure 3.9 is the current density profile for two cases of CL capillary pressure considered. The current density profiles for the two cases are almost the same when the voltage increases. However, when the voltage decreases, the current density of when CL capillary pressure is 1.3 of GDL capillary pressure is slightly more than that of

when CL capillary pressure is 0.8 of GDL capillary pressure. The slight improvement in performance observed in more hydrophobic CL is possibly due to the lower liquid saturation in the CL compared to that in the more hydrophilic CL.

3.2 THE EFFECTS OF DIFFERENT LOAD CHANGES

To study how the proton-exchange membrane responds to different load changes, we change the cell voltage from 0.8 to various lower values. Figure 3.10 shows the comparison of the ionic resistance in the membrane, water content and liquid water saturation at the membrane interface for the various cases considered. The voltage is stepped up from 0.6V, 0.5V, 0.4V, 0.3V and 0.25V to 0.8V; and after 800s, we step the voltage down to 0.6V, 0.5V, 0.4V, 0.3V and 0.25V. As the voltage is increased to 0.8V, the water content at the anode side of the membrane increases as a result of reduced electro-osmotic drag while the water content and the liquid water saturation at the cathode side of the membrane decreases because less water is dragged from the anode and less water is generated by the ORR. The ionic resistance in the membrane increases when voltage is increased to 0.8V because the average water content in the membrane goes down. When voltage is stepped down from 0.8V to 0.6V, the ionic resistance in the membrane decreases because more water is generated at the cathode side and the increase in electro-osmotic drag effect is not sufficient enough to cause the water content at the anode side to go down to a low value.

Likewise, when the voltage is stepped down from 0.8V to 0.5V, the ionic resistance decreases to a much lower value compared to when the voltage is decreased from 0.8V to 0.6V. This is because the average water content in the membrane goes up when the voltage is stepped down to 0.5V compared to when it is stepped down to 0.6V and at the same time, the water content at the anode side is still moderately high, 8.9.

When the voltage is stepped down to 0.4V, the ionic resistance decreases to a slightly lower value to when it is stepped down to 0.5V. This is because the water content on the anode side is still moderately high and the average water content in the membrane goes up.

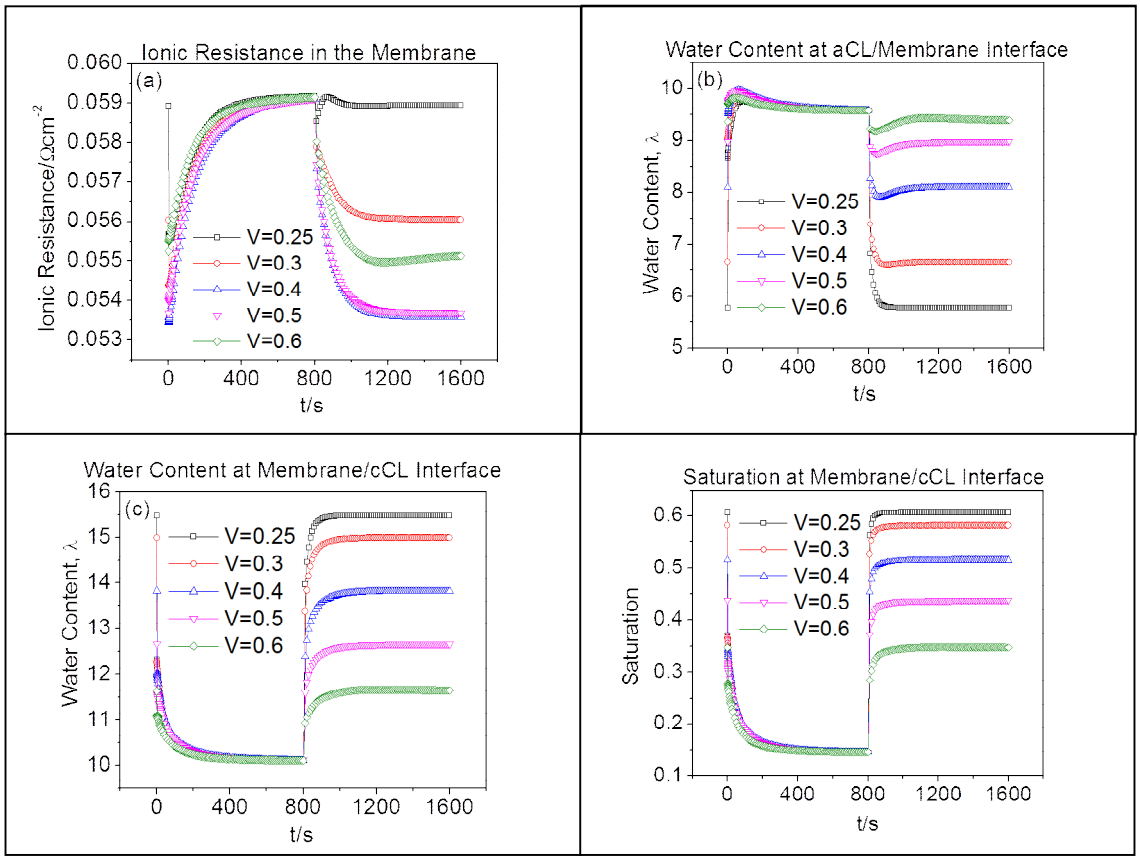

Figure 3.10: The effects of different load changes (a) ionic resistance in the bulk membrane during step change in voltage, (b) water content at aCL/membrane interface during step change in voltage, (c) water content at membrane/cCL interface during step change in voltage, (d) liquid water saturation at membrane/cCL interface during step change in voltage. (T = $80\,^{o}C$, P = 1bar, RH_a/RH_c = 100%/100%, Nafion® 112).

When the voltage is stepped down from 0.8V to 0.3V, the ionic resistance still decreases but to a higher value compared to when the voltage is stepped down from 0.8V

to 0.4V. Even though more water is generated at the cathode side when the voltage is stepped down to 0.3V compared to when it is stepped to 0.4V, the water content at the anode side has gone down considerably, to a value of 6.6, as a result of increased electro-osmotic drag. The lower water content at the anode side increased the average ionic resistance in the membrane.

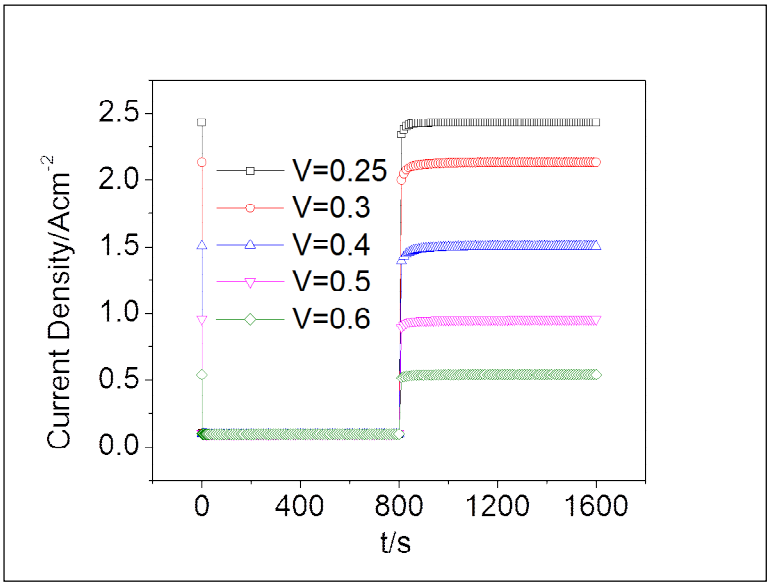

Figure 3.11: Current density profiles for different load changes (T = 80^{o}C, P = 1bar, RH_a/RH_c = 100%/100%, Nafion® 112).

When the voltage is stepped down to 0.25V, the ionic resistance goes up to a slightly higher value because the increased electro-osmotic drag causes the water content at the anode to be reduced to a much lower value, $\lambda = 5.7$. Besides the increased ionic resistance observed at low voltage, the liquid water saturation value at the cathode CL increases considerably, to 0.61 when the voltage is stepped down to 0.25V. The increased liquid water saturation reduces the path available for the transport of reactant gases and leads to a significant concentration overpotential loss. We noticed that the use of hysteresis in capillary pressure does not correctly capture the liquid water saturation

profile when the load change involves low voltage/high current, we only use injection capillary pressure for both increase and decrease in voltage in this section to capture the saturation profile correctly.

Figure 3.11 shows the current density profile for different load changes under the operating conditions used in figure 3.10. As expected, the lower the voltage that the cell is stepped down to, the higher the current density in the membrane.

3.3 THE EFFECTS OF DIFFERENT SATURATION AT GAS CHANNEL AND CATHODE GDL INTERFACE

In this section, we examine how choosing different saturation value at the gas channel/GDL interface affects the saturation in the cCL, the water content and hence the ionic resistance in the membrane. The boundary condition at the gas channel/GDL interface depends on GDL pore sizes and shape, GDL permeability, and flow condition in the gas channel. For simplification purposes, we choose the liquid water saturation at the gas channel/GDL interface to be a constant value, s_o. The s_o at the anode gas channel/GDL is kept at zero value while we vary the value of s_o at cathode gas channel/GDL.

From Figure 3.12, we see that increasing the value of s_o at cathode gas channel/cathode GDL interface increases the lowest steady state value of saturation in the cCL when voltage is stepped up. However, when voltage is stepped down, the amount of liquid water in the cCL seems not to be affected by the value of s_o. It therefore seems that increasing the value of s_o only increases the amount of liquid water retained in the CL and GDL after most of the liquid water formed has been removed by capillary forces. We only consider cases where the value of s_o is very small, i.e., $s_o<0.08$. Liu et al., in their steady state work, [124] saw that a higher value of s_o has more profound effect on the level of saturation in the CL.

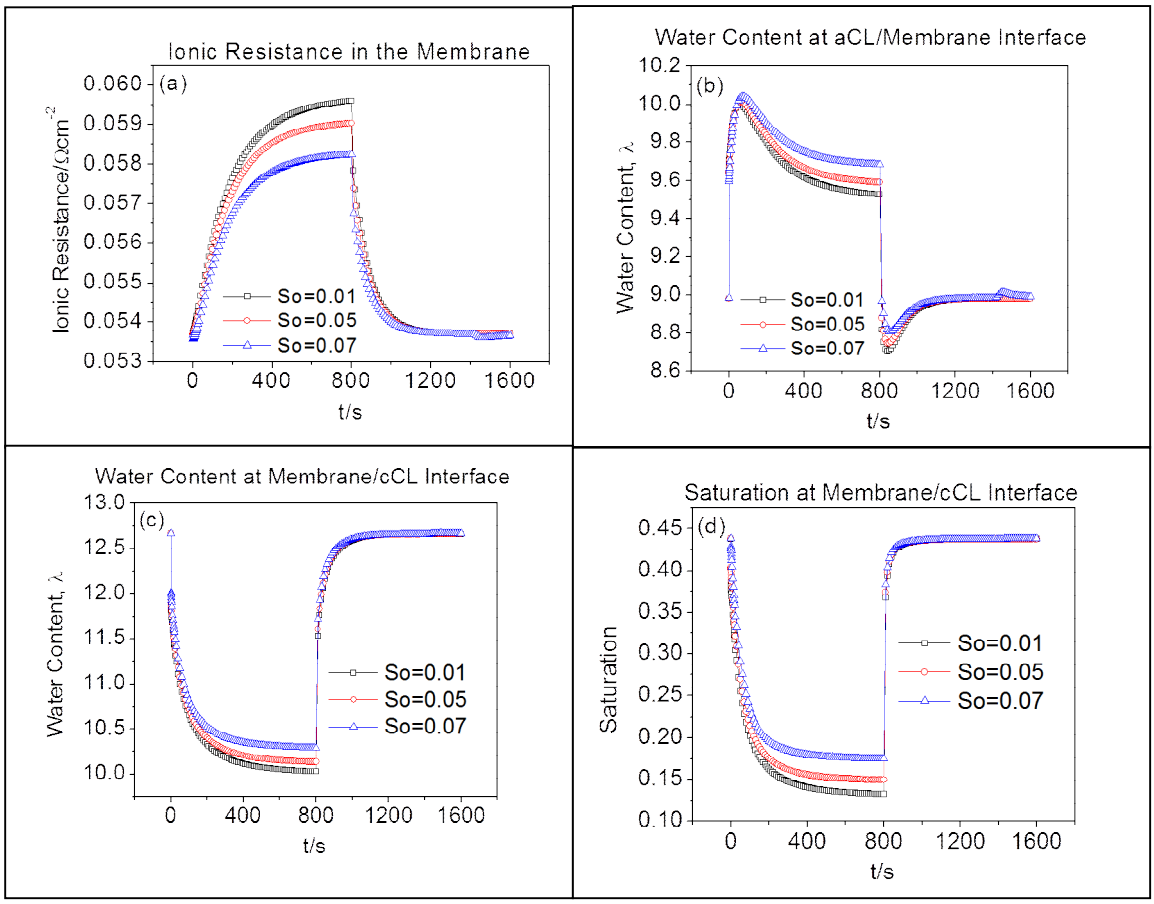

Figure 3.12: The effect of different value of saturation at cGDL/cGC interface (a) ionic resistance in the bulk membrane during step change in voltage, (b) water content at aCL/membrane interface during step change in voltage, (c) water content at membrane/cCL interface during step change in voltage, (d) liquid water saturation at membrane/cCL interface during step change in voltage. (T = 80ºC, P = 1bar, RH_a/RH_c = 100%/100%, 0.5V to 0.8V from t = 0 to 800s and 0.8V to 0.5V from 800s to 1600s, Nafion® 112).

The effect of different value of s_o on water content is similar to that of saturation, especially at the cathode side of the membrane where liquid water is formed. As more liquid water is retained in the CL and GDL, amount of water absorbed by the membrane increases so that the lowest steady state value of water content in the membrane goes up.

Because the average lowest steady state value of water content in the membrane increases, the highest value of ionic resistance in the membrane goes down.

Figure 3.13 shows the current density profiles for different value of liquid water saturation the interface between the cathode gas diffusion layer and cathode gas channel. The current density profiles are almost the same for the three cases considered in this work. As mentioned earlier, we only considered small saturation value. As observed by Liu et al [124], higher saturation values will have some effects on the current density profiles.

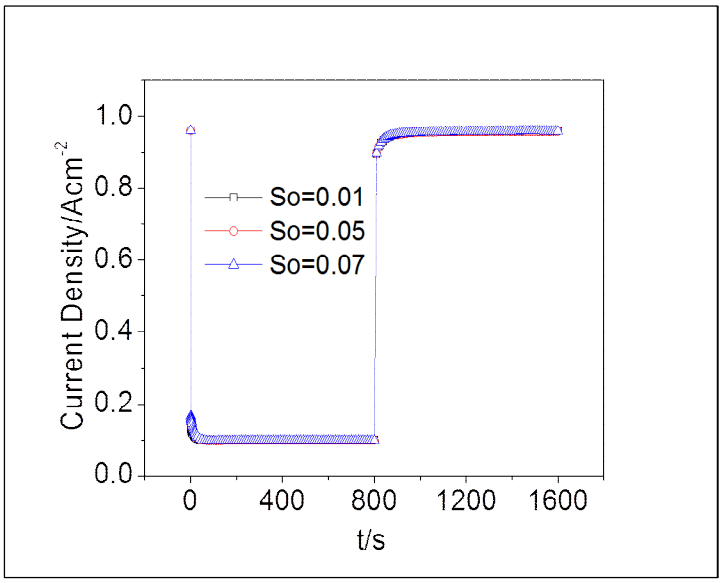

Figure 3.13: Current density profiles for different saturation at gas channel and cathode GDL interface during step change in voltage. (T = 80ºC, P = 1bar, RH_a/RH_c = 100%/100%, 0.5V to 0.8V from t = 0 to 800s and 0.8V to 0.5V from 800s to 1600s, Nafion® 112).

3.4 The Effects of Cathode Side Relative Humidity

In this section, we look at cases where the cathode inlet gas is not fully saturated. For comparison, we also include the case when the cathode inlet gas is fully saturated.

Zero saturation is chosen for both anode and cathode side of gas channel interface. The voltage is stepped up from 0.5V to 0.8V and then back to 0.5V. No liquid water is seen at the cCL when the relative humidity is 0.5, 0.4, 0.3 and 0.2.

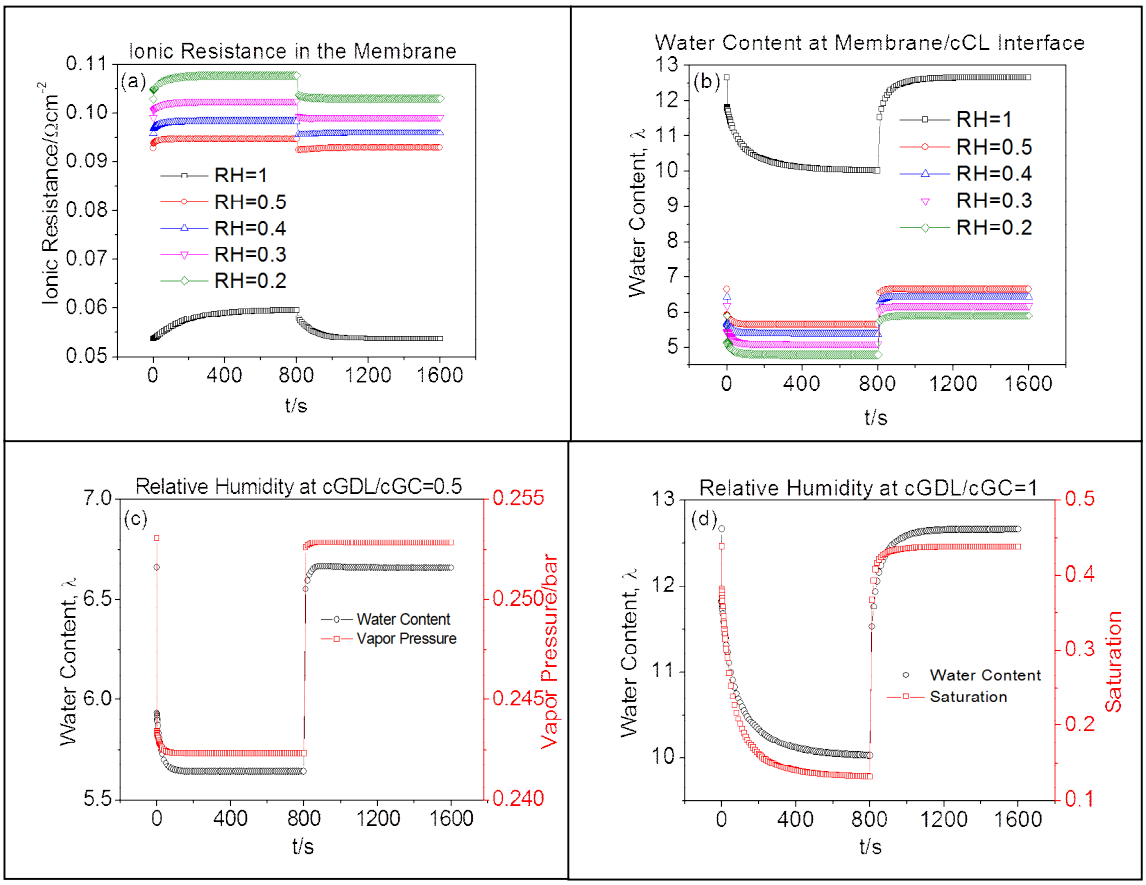

Figure 3.14: The effects of different cathode side relative humidity (T = 80^{o}C , P = 1bar, RH_a = 100%, 0.5V to 0.8V from t = 0 to 800s and 0.8V to 0.5V from 800s to 1600s, Nafion® 112).

Figures 3.14 (a & b) show the ionic resistance in the membrane and the water content at the cathode side of the membrane respectively. Also shown in Figure 3.14 are a combined plot of the water content and the vapor pressure for partially saturated cathode inlet conditions and a combined plot of the water content and the saturation for fully saturated cathode inlet condition at the cathode side of the membrane.

From Figure 3.14, the time constant for membrane hydration and dehydration for fully saturated cathode inlet condition is longer than those of partially saturated cathode inlet conditions. As shown in Figure 3.7(b), the liquid water saturation and the water content at the cathode interface of the membrane vary in a similar fashion while vapor pressure decreases instantaneously when the voltage is stepped up and also increases instantaneously when the voltage is stepped down. However, for partially saturated cathode inlet condition, where there is no liquid water at the cCL, the vapor pressure at the cathode interface of the membrane varies in a similar fashion to the water content at the same interface.

As mentioned earlier, when there is liquid at the cCL, the absorption and desorption of water in the membrane phase is determined by the fraction of the pores in the cCL that is filled with liquid water as vapor pressure is already saturated. However, when there is no liquid water in the cCL, the absorption and desorption of water in the membrane is determined by vapor pressure in contact with the membrane. Figure 3.14 shows that the vapor pressure at cathode side of the membrane for partially saturated inlet condition has smaller time constant compared to that of the liquid water saturation at the cathode side of the membrane for fully saturated cathode inlet condition. Since the vapor pressure in contact with the membrane for partially saturated cathode inlet condition reaches steady state faster than the liquid water in the cCL for fully saturated cathode inlet condition, the time for membrane hydration and dehydration for fully saturated cathode inlet condition is longer than those of membrane hydration and dehydration for partially saturated cathode inlet condition.

The comparison of the cases where the cathode reactant gas is not fully saturated shows that the time it takes the water content and hence the ionic resistance in the membrane to reach steady state increases as the relative humidity decreases when the

voltage is stepped up. When the voltage is stepped down, the ionic resistance decreases almost instantaneously when relative humidity at the interface between the GDL and gas channel is 0.5. The time to reach steady state increases as the relative humidity decreases. This is because the water in the membrane becomes more bound to the sulfonic acid group as the water content decreases and the time constant for water diffusion across the membrane increases [3]. The increase in diffusion time as water content in the membrane decreases accounts for the increase in time constant as the cathode relative humidity decreases.

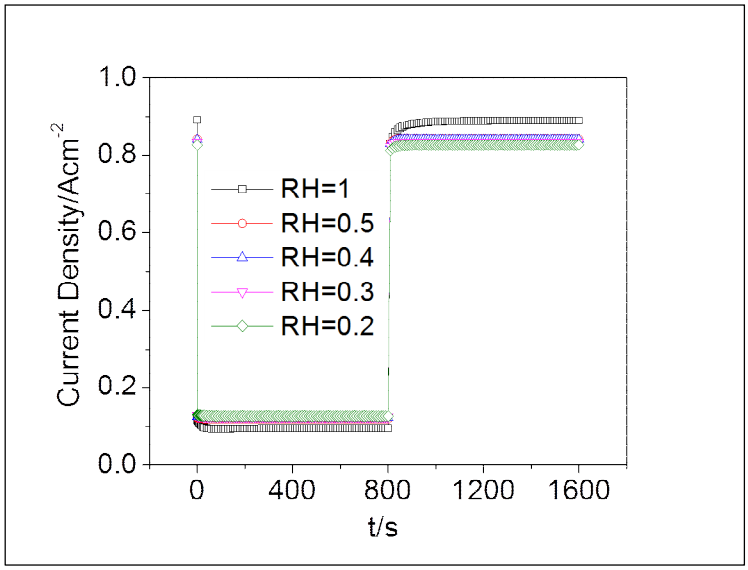

Figure 3.15: Current density profiles for different cathode side relative humidity during step change in voltage. (T = 80^{o}C, P=1bar, RH_a = 100%, 0.5V to 0.8V from t = 0 to 800s and 0.8V to 0.5V from 800s to 1600s, Nafion® 112).

Figure 3.15 shows the current density profiles for different cathode side relative humidity. In all the cases considered, the relative humidity at the anode side of the membrane is 100%. For partially saturated cathode feeds, increase in cathode side relative humidity leads to only minimal increase in current density. Even for fully saturated feed, we only significant increase in current density when voltage is decreased.

3.5 CONCLUSION

A 1-D, two-phase transient model that uses experimentally measured capillary pressure has been developed. The model shows that including permanent hysteresis observed in the capillary pressure of GDL has only minimal effect on the liquid water saturation and on the water content in the membrane. However at low voltage, the inclusion of hysteresis in capillary pressure does not give correct saturation profile. In the HFR experiment with 18μm Gore-select membrane, MEA hydration takes approximately 100s while the dehydration of the MEA takes about 550s. Similarly in the model with Nafion® 112, MEA hydration takes 250s while the dehydration of the MEA takes more than 600s. Nafion® 112 is more than two times thicker than 18μm Gore-select membrane. As water diffuses faster in thinner membrane compared to thicker one, the thickness difference of the two membranes accounts for the difference in the hydration and dehydration time constants.

It should be noted that the model in this section does not treat the MPL, though the MPL is included in the HFR experiment. Also, the model is assumed to be isothermal while phenomena like joule heating effect, evaporation and condensation will cause the temperature in the PEMFC sandwich to be slightly higher than the operating temperature. The effects of MPL on the transient model are considered in the next section. It is our belief that including the MPL will enable us to make the LANL data more closely.

The model shows that when voltage decreases/current increases, the hydration time constant is mainly determined by the rate of reaction and how fast water diffuses across the membrane. Also, when voltage increases/current decreases, the dehydration time constant is determined by how fast water phase (liquid or vapor) in contact with the membrane reaches steady state and by how fast water diffuses across the membrane. For instance, when there is liquid water at the cCL, because vapor is already saturated, the

time it takes the water content in the membrane to reach steady state is closely tied to that of liquid water saturation in the cCL. Both the profiles of water content and the liquid water saturation at cathode side interface of the membrane show similar trend when voltage is stepped up and down while vapor pressure drops instantaneously when the voltage is stepped up. As long as the liquid flows in the cCL is not at steady state, the water content in the cCL and hence in the membrane will continue to change. Thus, water content in the membrane will not reach steady state until the liquid water saturation reaches steady state. The hydration and dehydration time constants are shorter for thinner membrane because the time constant for water diffusion across the membrane is shorter in thinner membrane compared to thicker one. For instance time constant for water diffusion across Nafion® 117 is more than an order of magnitude longer than that of Nafion® 112. Unlike Nafion® 112, water content at the electrode interface in the case of Nafion® 117 reaches steady state faster than the water content in the bulk membrane because of the longer diffusion time constant in Nafion® 117.

When there is no liquid water in the cCL, the water content profile in the cCL follows that of vapor pressure in the cCL. Also, the time it takes the vapor pressure in the cCL, when there is no liquid water, to reach steady state is shorter than the time it takes the saturation in the cCL to reach steady state when there is liquid in the cCL. The absorption and desorption of water in the membrane is determined by vapor pressure in the electrodes when there is no liquid water, while the absorption and desorption of water content in the membrane is determined by liquid water saturation when there is liquid water in the cCL. The time constant for water content to reach steady state in the membrane is longer when there is liquid water compared to when there is no liquid water. The model also predicts that at low cell voltage there is an increased ionic resistance in the membrane accompanied by high liquid water saturation.

Chapter 4: Result and Discussions Part II: the Effects of MPL on the Transient Response of PEMFC under load change

In this section, we investigate how placing the MPL between the CL and the GDL affects the transient response of PEMFCs to load changes. Capillary pressure measured by Gostick et al. [81] for compressed Toray 120C is used for GDL in this model. Injection capillary pressure is used when the cell voltage is increased as well as when the cell voltage is decreased. As observed in chapter 3, withdrawal capillary pressure does not capture the saturation profile accurately at low voltage.

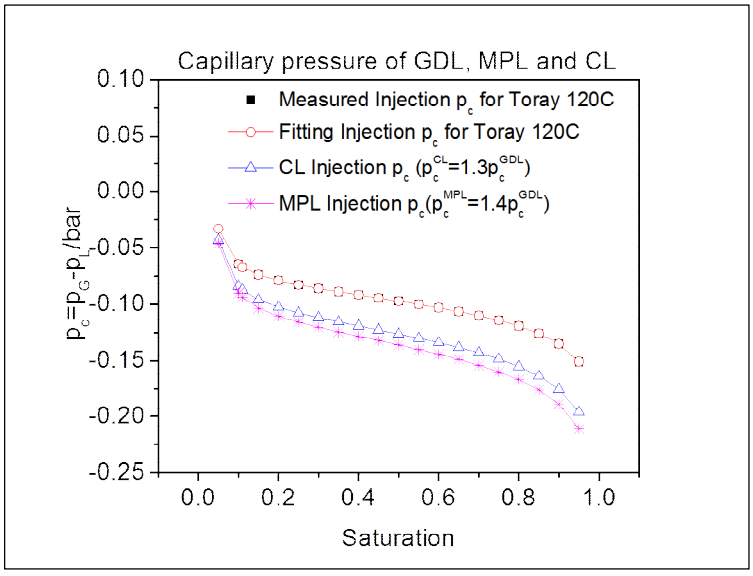

Figure 4.1: Experimentally measured capillary pressure of compressed Toray 120C, CL capillary pressure and based case MPL capillary pressure.

Weber [83] also suggested that injection capillary pressure should be valid whether load is increased or decreased. As there are no suitable experimentally measured capillary pressures for CL and MPL in the literature, we use an approach similar to that of Leverrett J-function where the capillary pressures of CL and MPL are constant

multiplied by that of GDL. This approach is explained in detail in chapter 3. Figure 4.1 shows the base capillary pressured used to both CL and MPL in this section.

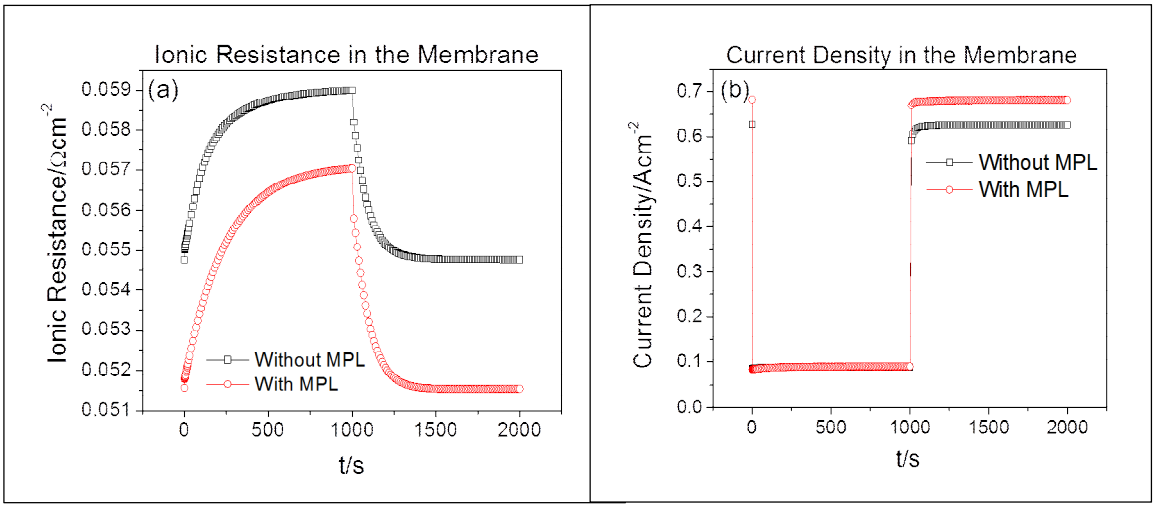

Figure 4.2: The plot of ionic resistance and the current density in the bulk membrane for when there is cMPL and no MPL is used (Nafion 112 membrane, T = 80 °C, P = 1bar, RH_a/RH_c = 100%/100%, 0.5V to 0.8V from t = 0 to 1000s and 0.8V to 0.5V from 1000s to 2000s).

The plot of ionic resistance in the bulk membrane shown in figure 4.2a shows that in the case where no MPL is used, more than 70% of the transient process occurs within the first 200s after the step change in change from 0.5V to 0.8V while about 50% of the transient process occurs during the same period when cMPL is used. In the case when no MPL is used, because most of the transient process occurs within the first 200s the transient process slows down considerably thereafter as the steady state is approached. However in the case with cMPL, the transient process does not slow down significantly until after 600s. The use of cMPL does not show any significant effect when the voltage is stepped down from 0.8V to 0.5V after 1000s. We also observed that the ionic resistance of the case with cMPL is lower than that with no MPL. Figure 4.2b shows the current density in the membrane increases with the use of cMPL. As it has been

mentioned in the literature, the use of MPL not only hydrates the membrane better but also creates an intimate contact between the MPL and adjacent layers (GDL and CL) which results in reduced contact resistance between the layers [28]. It is the combination of these effects that leads to the increase in current density in the membrane when cMPL is used.

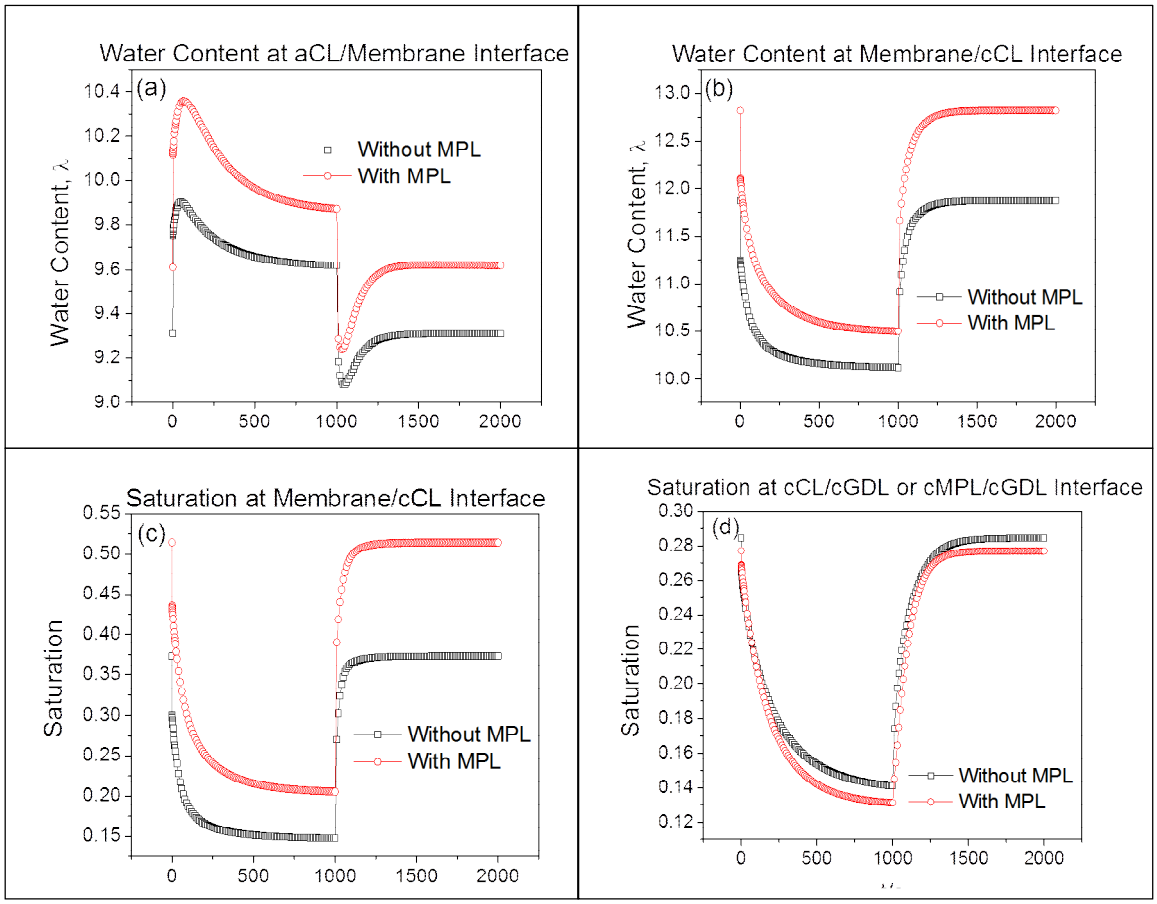

Figure 4.3: The plot of water content at anode side and cathode side membrane interfaces and liquid water saturation at cathode side membrane and cGDL interfaces for when cMPL is used and when no MPL is used (Nafion 112 membrane, T = 80 °C, P = 1bar, RH_a/RH_c = 100%/100%, 0.5V to 0.8V from t = 0 to 1000s and 0.8V to 0.5V from 1000s to 2000s).

Next we explore the transport of water phases in the PEFC sandwich as a means of explaining the observed differences in ionic resistance between cases with cMPL and that with no cMPL. Figures 3.3 (a & b) show the plots of water content at anode side and cathode side of the membrane interfaces respectively. Also, Figures 4.3 (c & d) show the plots of liquid water saturation at cathode side and cGDL interfaces. From the plots of water content at the anode side of the membrane shown in figure 4.3a, the water content at the anode side of the membrane is more for the case with cMPL compared to the case with no MPL. After the cell voltage is increased from 0.5V to 0.8V, the water content at the anode side of the membrane increases almost immediately because of the decrease in electro-osmotic drag. The increase in the water content in the case with cMPL is more than that with no MPL. The water content profiles at the anode side peak after the increase because the back diffusion force balances that of the electro-osmotic drag. The decrease in water content after reaching the peak value occurs because the electro-osmotic drag becomes dominant [15].

Similarly, when the cell voltage is stepped down from 0.8V to 0.5V at 1000s, the water content at the anode side of the membrane decreases almost immediately in case with no MPL as well as in case with cMPL because of the increase in electro-osmotic drag. The water content profile on the anode side of the membrane reaches minimum value when the back diffusion force balances that of the electro-osmotic drag. Other than the increase in water content at the anode side of the membrane, the use of cMPL does not significantly affect the transient process at the anode side of the membrane.

Comparing our modeling prediction for the case with cMPL as well as the case with no MPL to the MEA HFR measured in cell with MPL shown in Figure 3.3 in chapter 3, the trend of our model with cMPL appears to closely match that of the measured MEA HFR. When current density decreases/voltage increases, the increase in

the HFR and the ionic resistance in the case with cMPL appear to be gradual unlike the modeling prediction for the case with no MPL where most of the transient process occurs within the first few hundred seconds after the voltage increase. The use of cMPL lowers the saturation in the cGDL, however it does not have any major on the transient process of the liquid water in the cGDL.

From the water content profiles shown in Figure 3.3b, we observe that more than 80% of the decrease in water content when the cell voltage is stepped up from 0.5V to 0.8V occurs within the first 200s in the case when there no MPL. The decrease in water content at the cathode side of the membrane slows down considerably thereafter. However in the case with MPL, the water content at the cathode of the membrane continues to show significant decrease up until 600s. The use of MPL does not show significant effect when the cell voltage is decreased from 0.8V to 0.5V at 1000s. Similar to the profiles of water content at cathode side of the membrane, the liquid water saturation profile shows that more than 90% of the decrease in liquid saturation when the cell voltage is increased from 0.5V to 0.8V occurs within the first 200s in the case when there is no MPL. The decrease in liquid water saturation slows down considerably afterward as the saturation reaches steady state. However, in the case with cMPL, the liquid water saturation continues to show significant decrease up until 600s. The use of cMPL does not show any significant effect when the cell voltage is stepped down from 0.8V to 0.5V at 1000s. Besides the difference in transient response observed with the use of cMPL, the water content and the saturation at the cathode side of the membrane increases when cMPL is used. However, the liquid saturation in the cGDL is less when cMPL is used as shown Figure 4.3d. Although our model predicts less liquid water in the cGDL with the use of cMPL, the transient process of liquid water in the cGDL seems not to be affected by the presence of cMPL.

Figure 4.3c shows that when cMPL is used, the transport of liquid water generated by the electrochemical reaction from the cCL is slowed down especially during the first few hundred seconds when the cell voltage is increased (current density decreases). However when the cell voltage is decreased (current density increases), the use of cMPL does not have any significant effects on the rate of transport of liquid water. When the cell voltage is increased, the decrease in the electro-osmotic drag and in the rate of water generation lead to a decrease in liquid water saturation in the cCL since the liquid water moves out of the cCL by capillary action. On the other hand, when the cell voltage is decreased, the increase in electro-osmotic drag and rate of water generation combines to instantaneously increase the liquid water saturation in the cCL. As explained in our previous work [15], while how fast the liquid water is transported out of the cCL and the rate of water diffusion across the membrane mainly determine the transient response when the voltage is increased, the rate of water generation and diffusion across the membrane largely determine the transient response when the cell voltage is decreased. The water generation occurs almost instantly in the cCL and more water is generated when the cell voltage decreases (current increases), the transport of water may therefore not be as nearly as important as the rate of water generation in determining the transient process when the cell voltage is decreased. MPL has been shown to partially restrict the transport of liquid water from the cCL to the cGDL [28]. This is why the use of cMPL does not show significant effect on the transient process when the cell voltage is decreased. On the other hand, less water is generated when the cell voltage is increased while the water already in the cCL is being transported out of the cCL, the rate at which water is being transported out of the cCL may therefore be more important than the rate of water generated. Because the rate at which water is being transported out the cCL is mostly important when the voltage is increased and the use of cMPL partially restricts the

transport of the liquid water out of the cCL, the use of cMPL slows down the transport of liquid water out of the cCL when the cell voltage is increased but shows no significant effect on the transient process when the cell voltage is decreased.

Since the dissolved water in the membrane will not reach equilibrium as long as the water in contact with the membrane (whether liquid or vapor) is not at steady state [15], the transient process in the membrane is also prolonged by the use of MPL. Besides increasing the liquid pressure at the cCL which forces water through the membrane [28, 61], the slowing down of the liquid water being transported out of the cCL will also cause the membrane to be equilibrated with the water generated for a longer time. The prolonged equilibration of the water generated with the membrane and the ionomer in the cCL will reduce the ionic resistance.

4.1 Effects of MPL Absolute Permeability

In this section, we examine the effects of MPL absolute permeability on the transient process in the proton-exchange membrane. A value of $1e-11cm^2$ is chosen as the base case for the MPL absolute permeability in this study. We choose values of MPL absolute permeability within the range of $5e-11cm^2$ to $5e-12cm^2$ for the study in this section. For the sake of comparison, we also include the case where there is no MPL.

Figure 4.4 shows the ionic resistance, water content and saturation at the cathode side of the membrane and also the saturation at the interface between the cMPL and the cGDL for cases with different MPL absolute permeability. As seen in figure 4.2, the use of MPL slows down the transient process especially within the first few hundred seconds especially when the cell voltage is increased. Figure 4.4a shows that MPL absolute permeability has a strong effect in determining how long the transient process is prolonged as a result of the use of cMPL. The GDL absolute permeability used in this

work is $1e-10cm^2$. Since the pore sizes in the MPL is usually smaller than that of GDL, the MPL permeability is expected to be smaller than that of GDL. As we increase the MPL permeability to a value close to that of GDL, the increase in the time it takes the transient process in the membrane to reach steady state as a result of the use of MPL diminishes.

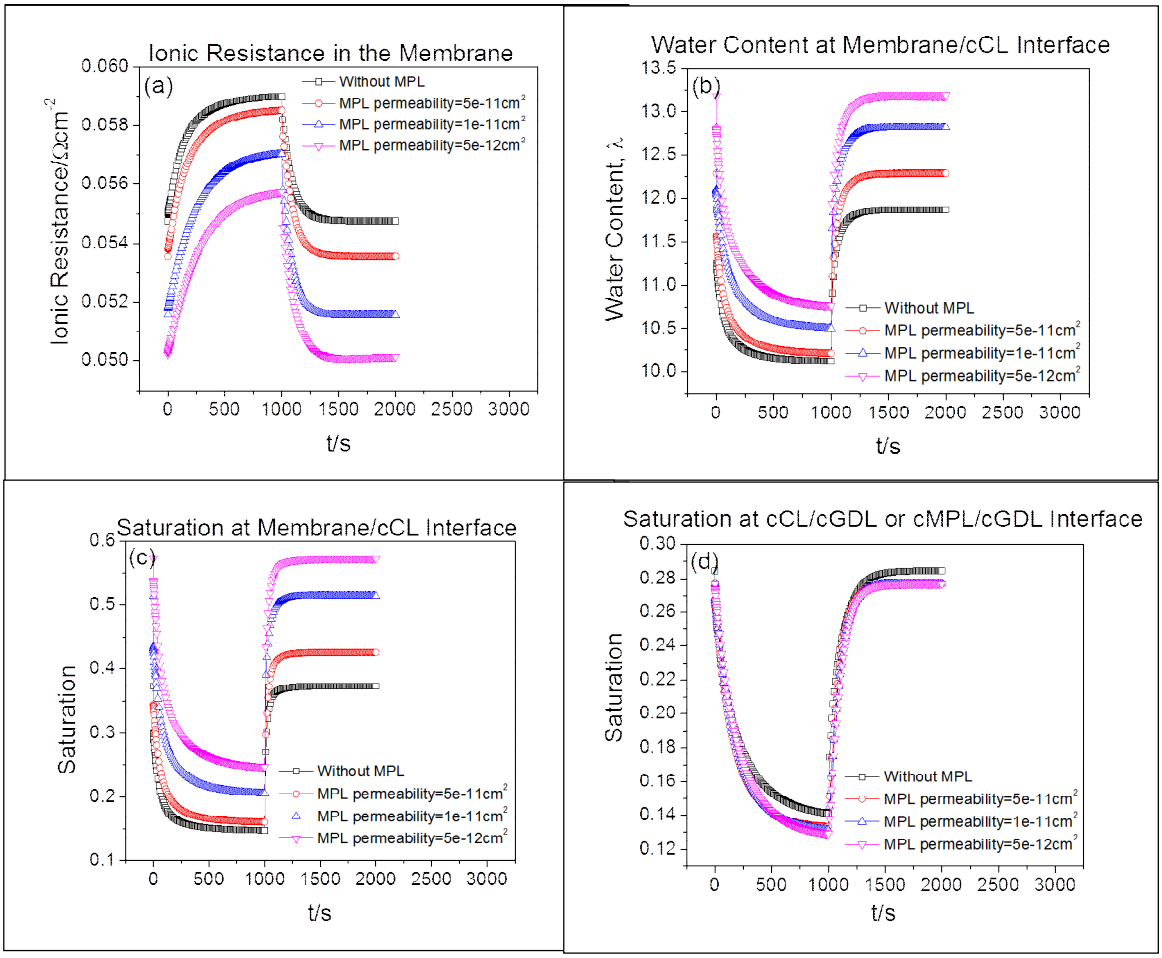

Figure 4.4: The plot of ionic resistance, water content and saturation at the cathode side of the membrane and the saturation at the interface between the cMPL and the cGDL for cases with different MPL absolute permeabillity (Nafion 112 membrane, T = 80 °C, P = 1bar, RH_a/RH_c = 100%/100%, 0.5V to 0.8V from t = 0 to 1000s and 0.8V to 0.5V from 1000s to 2000s).

Similar to what we observed in the ionic resistance shown in figure 4.4a, the figures 4.4(b&c) show that the effect of cMPL on the transient process diminishes as the MPL absolute permeability is increased. The difference in transient process due to the use of cMPL becomes almost negligible compared to the cases with no MPL when the MPL absolute permeability of $5e-11cm^2$. However as we decrease the MPL absolute permeability, the time it takes the water content and liquid saturation to reach steady state increases in addition to increase in water content and saturation level in the cCL.

Figure 4.4d shows that the saturation level in the cGDL is lowered when there is cMPL compared to the case where there is no cMPL. Decreasing the MPL absolute permeability only decreases the saturation in the cGDL slightly. However, figure 4.4c shows that decreasing the MPL absolute permeability leads to a large increase in the saturation level in the cCL.

4.2 EFFECTS OF MPL CAPILLARY PRESSURE

In this section, we investigate the effects of MPL capillary pressure on the transient response of the proton-exchange membrane. As mentioned earlier, because there is lack of suitable experimentally measured MPL capillary pressure in the literature, we choose an approach similar to that of Leverett-J function where MPL capillary pressure is a constant multiplied by that of the GDL. Details of this approach is in our previous work [15]. Based on the assumption that the MPL is more hydrophobic that GDL, we choose as base case MPL capillary pressure, Pc^{MPL} shown below:

$$Pc^{MPL} = 1.4Pc^{GDL} \tag{3.2}$$

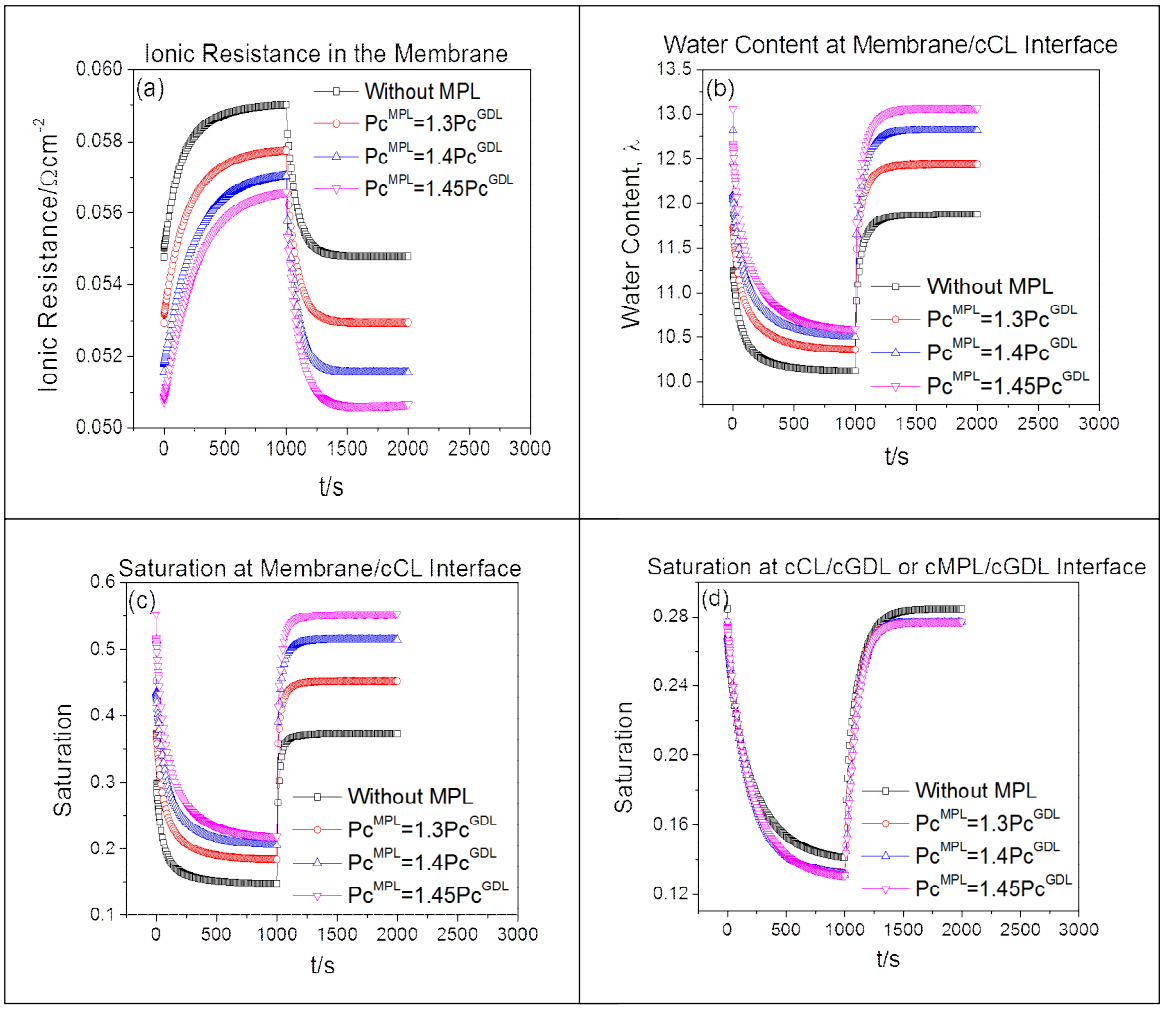

Figure 4.5: The plot of ionic resistance, water content and saturation at the cathode side of the membrane and the saturation at the interface between the cMPL and the cGDL for cases with different MPL capillary pressure (Nafion 112 membrane, T = 80 °C, P = 1bar, RH_a/RH_c = 100%/100%, 0.5V to 0.8V from t = 0 to 1000s and 0.8V to 0.5V from 1000s to 2000s).

Figure 4.5 shows the ionic resistance, water content and saturation at the cathode side of the membrane and also the saturation at the interface between the cMPL and the cGDL for cases with different MPL capillary pressure. The case where there is no MPL is included for comparison. Figure 5a shows that as the MPL capillary pressure decreases (MPL becomes less hydrophobic), the ionic resistance increases and the difference in the

transient process in the membrane between the case with no MPL and that with cMPL diminishes. As the hydrophobicity of the MPL decreases, the restriction to the movement of the liquid water through the cMPL decreases and the transient process in the membrane within the first few hundred seconds becomes faster compared to the cases with more hydrophobic MPL.

Figures 4.5 (b&c) show that the water content and saturation at the cathode side of the membrane increases as the MPL hydrophobicity increases (MPL capillary pressure increases). Also, during the first 1000s when the cell voltage decreases, the time it takes the water content and the saturation at the cathode of the membrane to reach steady state increases as the hydrophobicity of the MPL increases. However, no significant difference is observed in the transient process of the second 1000s where the cell voltage decreases from 0.8V to 0.5V. As explained above, how fast water moves out of the cCL is mostly important when voltage increases/current decreases and the use of MPL partially blocks the transport of water out of the cCL. Therefore the increase in the hydrophobicity of the cMPL only has effects on the transient process when the cell voltage increases.

Figure 4.5d shows that the liquid water saturation in the cGDL is lower when there is MPL compared to where is no MPL. Also, increasing the hydrophobicity of the MPL decreases the liquid water saturation in the cGDL slightly. As the hydrophobicity of the MPL increases, the liquid pressure on the cathode side of the membrane increases [61]. Because of the increase in the liquid pressure at the cCL, some of the liquid water formed from the water generated by the electrochemical reaction is forced to go through the membrane. The restriction on the transport of the liquid water out of the cCL leads to decrease in the liquid water saturation in the cGDL and also the increase in the time it takes the liquid water in the cCL to reach steady state when MPL is used.

4.3 CONCLUSION

In this section, we added cMPL to the model developed in chapter 3. The use of cMPL slows down the transient process considerably when the cell voltage increases (current decreases) especially during the first few hundred seconds after the step change in voltage. However, the use of cMPL does not have any significant impact on the transient response when the cell voltage is decreased. As shown in our previous model [15], how fast water is transported out the cCL is mostly important to the transient process when the cell voltage is increased and the use of cMPL has been shown to partially block the transport of liquid water in the cCL [28]. Thus, our model predicts that the use of cMPL slows down transient process when the cell voltage is increased but no significant effect when the cell voltage is decreased. Comparing our modeling prediction for the case with cMPL as well as the case with no MPL to the MEA HFR measured in cell with MPL, the trend of our model with cMPL appears to closely match that of the measured MEA HFR. When current density decreases/voltage increases, the increase in the HFR and the ionic resistance in the case with cMPL appear to be gradual unlike the modeling prediction for the case with no MPL where most of the transient process occurs within the first few hundred seconds after the voltage increase. The use of cMPL lowers the saturation in the cGDL, however it does not have any major on the transient process of the liquid water in the cGDL.

The model also predicts that as the MPL absolute permeability is decreases, the transient process in the membrane becomes prolonged. Also, the ionic resistance in the membrane decreases as the MPL absolute permeability is decreases. As the MPL capillary pressure decreases (MPL becomes less hydrophobic), the transient process in the proton-exchange membrane becomes faster and the ionic resistance in the membrane increases.

Chapter 5: Results and Discussions Part III: Optimization of the Morphological Proprieties of HT-PEMFC Components for Effective Membrane Hydration

We compared our modeling results with experimental data from Sousa et al. [100] to validate the accuracy of the model. Figure 5.1 shows the comparison between the experimental data and the prediction from our model, which indicates a reasonably good agreement.

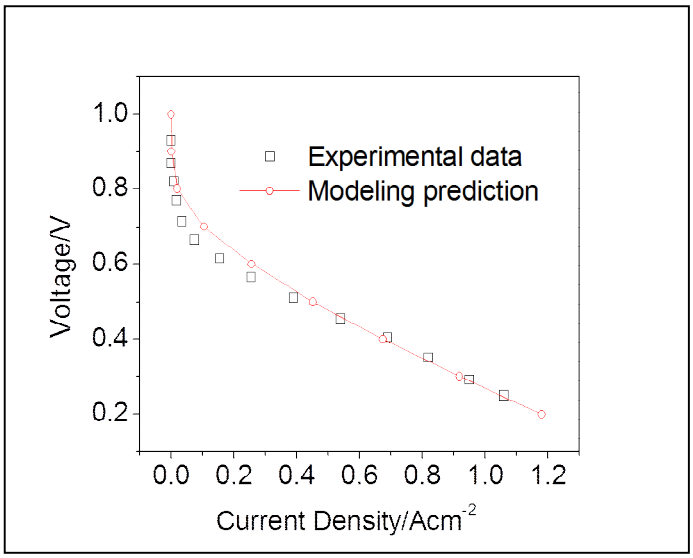

Figure 5.1: Comparison between the model prediction and experimental data[100] (operating temperature is 150℃, cell operates with hydrogen and air at 0.38% relative humidity and operating pressure of 1atm, acid doping level is 5.6).

The data shown in Figure 5.1 is at 150℃. The cell operates with hydrogen and air at 0.38% relative humidity and atmospheric pressure. An acid doping level of 5.6 is used for the modeling prediction because the proton conductivity in Sausa et al. [100, 101] is computed at an acid doping level of 5.6. All the design parameters provided in Sousa et al. [100] are incorporated in t he model and representative values are used for the parameters that are not given Sousa et al. [100].

As mentioned in chapter 1, the saturation pressure of water increases sharply at high temperature and this makes membrane hydration difficult without increasing the total pressure of the feed gas. It is helpful to develop cell design guidelines that allow water produced by oxygen reduction reaction and that carried into the cell by the feed gas to be retained as close as possible to the membrane to improve the conductivity of the membrane without increasing the vapor pressure in the feed gas. The is the focus of this work is to define optimum values of morphological properties of PEMFC components, that will help keep water in the CL as much as possible, to prevent membrane dehydration and consequently reduce ionic resistance.

5.1 INLET RELATIVE HUMIDITY

We choose as our base case an inlet relative humidity of 3.8% at an operating temperature of 190°C, which is equivalent to fully humidified feed gases at 80°C. Figure 5.2 shows the ionic resistance in the membrane and vapor pressure at both anode and cathode membrane interfaces for cells with different inlet relative humidity. Inlet relative humidity of 0.25% in Figure 5.2 is equivalent to fully humidified feed gases at room temperature. Figure 5.2 (b &c) shows that the difference between the vapor pressure at the membrane anode and cathode interface for cell with no humidification and that in which the feed gases are humidified at room temperature is very small. Significant increase in vapor pressure at membrane interface is only observed when the feed gases are humidified at higher temperatures.

Similarly, Figure 5.2a shows that humidifying feed gases at room temperature has minimal impact on the ionic resistance in the membrane. For the humidification of feed gases to have a meaningful effect on the ionic resistance in the membrane and on cell performance, the humidification should be carried out at higher temperature. However,

humidifying feed gases at 80°C or at higher temperature will require complex system design and additional power consumption [102].

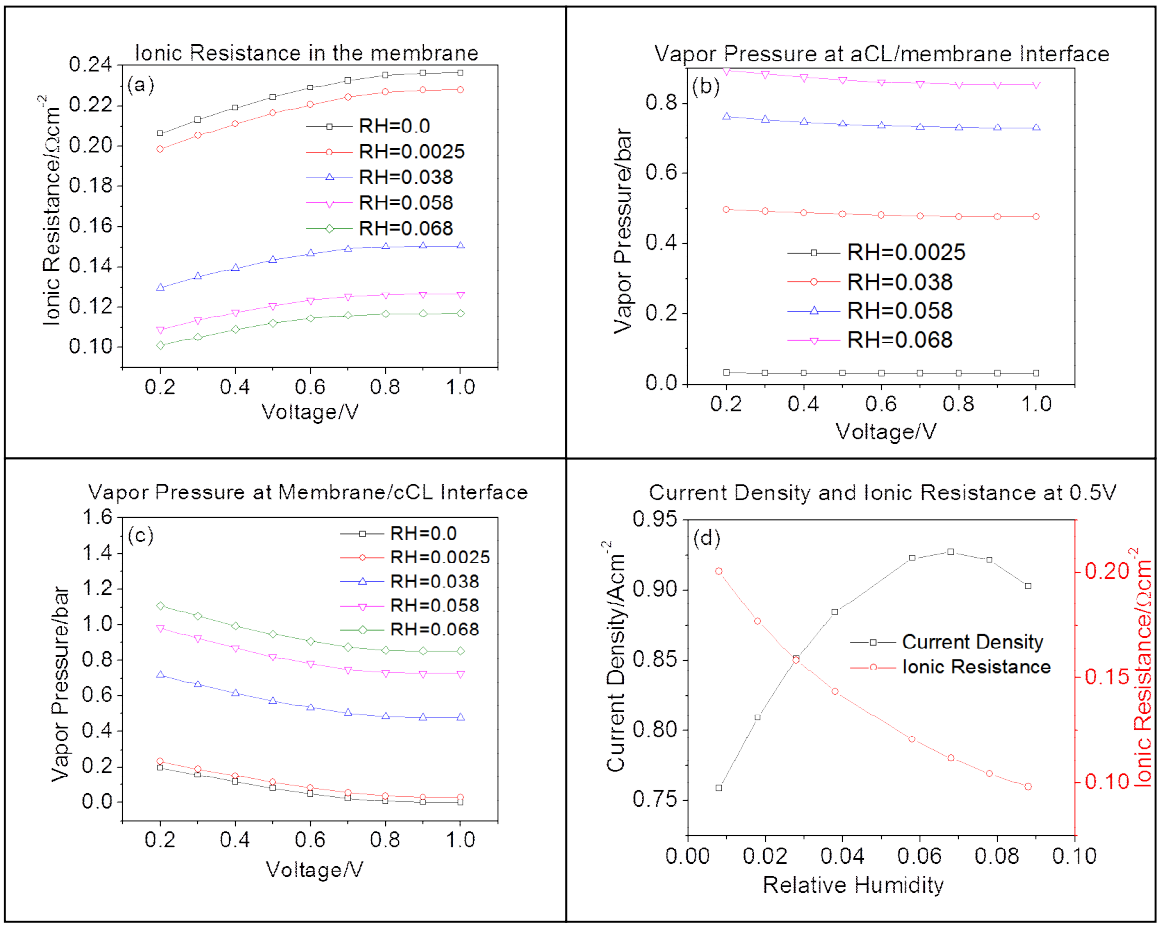

Figure 5.2: Effects of relative humidity on current density and the ionic resistance in the membrane (operating temperature is 190°C, the cell operates with hydrogen and oxygen 2 bar with an acid doping level of 6).

Figure 5.2d shows the plots of ionic resistance and current density in the membrane as a function of inlet relative humidity. We observe that even though ionic resistance in the membrane continue to decrease as the inlet relative humidity increases, the current density peaks at around inlet relative humidity of 6% and afterward decreases

with increasing inlet relative humidity. The decrease in current density with increasing inlet relative humidity is due to dilution of reactant gases. Lowered concentrations of the reactant gases lower the overall transport rates of gases and the partial pressure of reactants at the electrocatalyst surface, and thus decrease the rate of charge transfer reaction.

Considering the complexity of system design and addition power consumption required for feed gas humidification at high temperature, coupled with the possibility of reactant gas dilution, increasing relative humidity of the feed gases might not be viable for improving the performance of HT-PEFC's. Rather than increasing the inlet relative humidity of the feed gases, the water vapor generation by the oxygen reduction reaction should be retained as much as possible in the CL to help improve the proton conductivity of the membrane. Adjusting the morphological properties of the HT-PEMFC components like the MPL and GDL will help retain the water generated by the electrochemical reaction in the CL.

5.2 EFFECTS OF INCLUDING MPL

In the low-temperature PEFC, the MPL has been shown to partially block the movement of liquid water from the CL to the GDL, and forces the liquid water back through the membrane, thereby keeping the membrane hydrated [28, 61]. Here we study how including an MPL in HT-PEMFC components helps retain water vapor in the CL. Figure 5.3 shows the ionic resistance in the membrane for cells without any MPL, with a microporous layer only on the cathode, and with both cathode and anode MPLs. Figure 5.3 shows that the inclusion of MPL does help reduce the ionic resistance in the membrane; the reduction in ionic resistance in the presence of a MPL increases as cell voltage decreases.

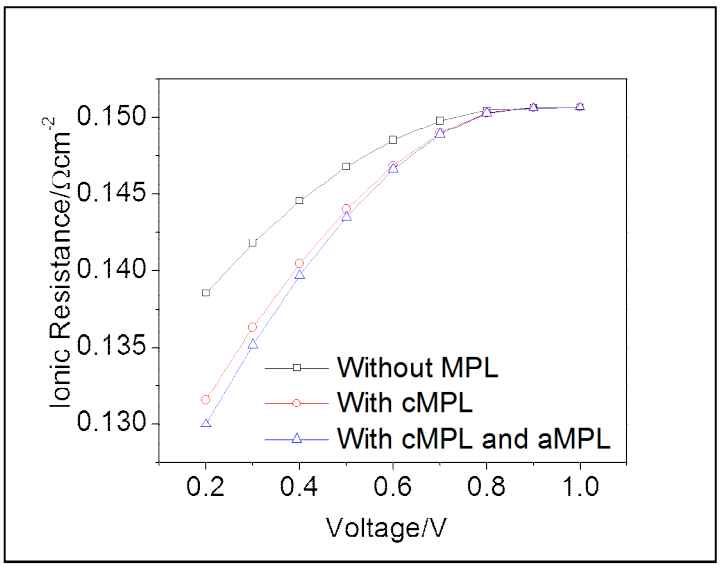

Figure 5.3: The plot of ionic resistance in the cell with and without MPL (operating temperature is 190℃, the cell operates with hydrogen and oxygen at 3.8% relative humidity and operating pressure of 2 bar, acid doping level of 6).

Comparison of the ionic resistance of the cell with cathode MPL and that with both MPLs shows that the beneficial effect of including an MPL on the anode is minimal in comparison to that of including the cathode MPL. Most of the reduction in ionic resistance occurs due to the inclusion of the cathode MPL, which helps retain the water generated by the electrochemical reaction in the CL as much as possible.

The plots of partial vapor pressure at both anode and cathode membrane interfaces are shown in Figure 5.4. Figure 5.4a shows the plot of the vapor pressure at the anode interface of the membrane while Figure 5.4b shows the plot of the vapor pressure at the cathode interface of the membrane. The water vapor at the anode interface of the membrane goes up with the addition of aMPL. Because the PBI membrane is assumed to be impermeable to gases, the addition of cMPL does not have any noticeable effects on the water vapor at anode interface of the membrane. As the reactant gases diffuse to the

aCL, hydrogen is oxidized, leaving water vapor from the feed gas behind. Since the gas permeability of MPL is lower than that of GDL, the use of MPL at the anode restricts the diffusion of the water vapor back to the GDL. Because more hydrogen is consumed when the cell voltage decreases, the amount of water vapor left behind by the oxidized hydrogen gas increases.

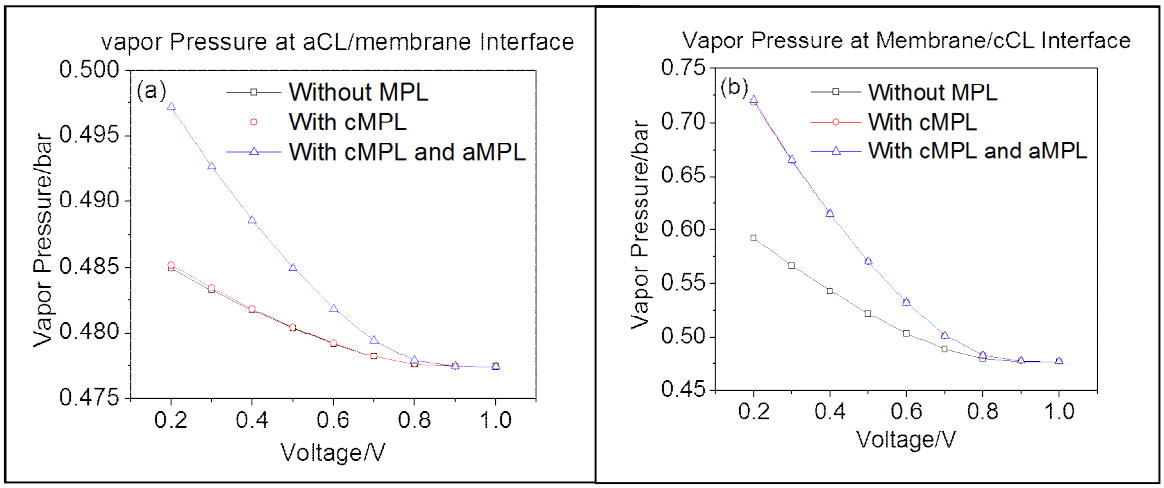

Figure 5.4: The plot of water vapor partial pressure in a cell with and without MPL (a) vapor pressure at aCL/membrane interface, (b) vapor pressure at membrane/cCL interface. (Operating temperature is 190°C, the cell operates with hydrogen and oxygen at 3.8% relative humidity and operating pressure of 2 bar, acid doping level of 6).

Similarly, Figure 5.4b shows that the use of cMPL helps retain more water at the cCL. The amount of water retained increases as the cell voltage decreases. At the cCL, in addition to the water vapor left behind when oxygen is reduced, water is also produced by the oxygen reduction reaction. This is why the vapor pressure at the cathode side of the membrane is significantly higher than that at the anode side as shown in Figure 5.4. Because there is more water vapor at the cathode, the use of cMPL helps retain more water in the cCL. This explains the result of Figure 5.3, which shows that most of the

reduction in the ionic resistance resulted from the use of MPL comes from the use of cMPL.

5.3 EFFECTS OF MPL PORE SIZES

To examine how changing the MPL pore size affects the effectiveness of MPL in retaining water vapor in the CL, we vary the MPL pore radius. In this study we choose as our base an MPL mean pore radius of 0.03μm. Figure 5.5 shows the plot of ionic resistance in the membrane of cell with different MPL pore sizes. As seen from figure 5.5, the ionic resistance in the membrane decreases as the MPL pore size (mean pore radius) decreases. The decrease in ionic resistance with decreasing MPL pore size increases as the MPL mean pore radius gets smaller. The decrease is ionic resistance when the MPL mean pore radius decreases from 0.03μm to 0.01μm is more than twice the decrease in ionic resistance when the MPL mean pore size decreases from 0.06μm to 0.03μm. Also, as the cell voltage decreases, the magnitude of the decrease in ionic resistance as a result of the decrease in the MPL pore size increases.

Shown in Figure 5.6 are the plots of partial vapor pressure at both the anode and cathode interfaces of the membrane in cells with different MPL pore sizes. Figure 5.6a shows the vapor pressure at the anode interface of the membrane while Figure 5.6b shows the vapor pressure at the cathode interface of the membrane. Figure 5.6a shows that changing MPL pore sizes has little effect on the water vapor at the anode interface of the membrane. However, the vapor pressure at the cathode interface of the membrane increases as the MPL mean pore radius decreases. Since the vapor pressure at aCL is only from the feed gas while that at cCL is from both feed gas and by-product of oxygen reduction reaction, one can infer that changing the MPL pore size will mainly affect the

effectiveness of the MPL in retaining the water generation by electrochemical reaction in the CL.

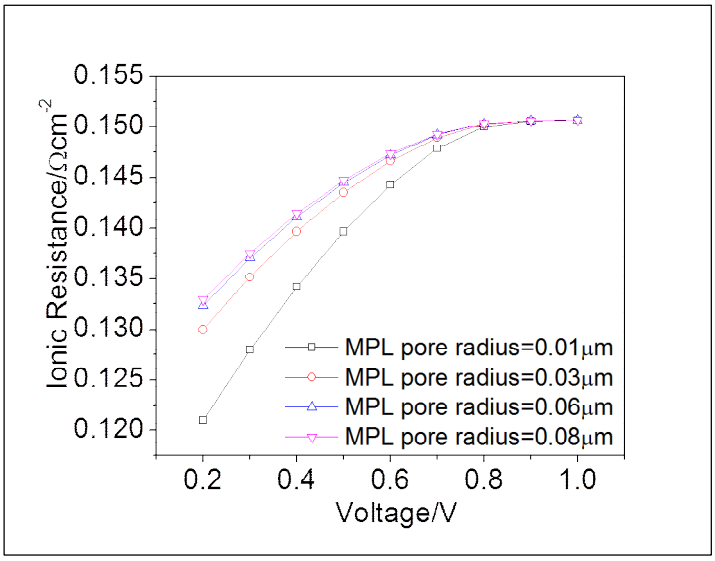

Figure 5.5: The plot of ionic resistance for cells with different MPL pore radius (operating temperature is 190℃, the cell operates with hydrogen and oxygen at 3.8% relative humidity and operating pressure of 2bar, acid doping level of 6).

Also, we observe that the increase in vapor pressure at the cathode interface of the membrane when the MPL mean pore radius decreases from 0.03 μm to 0.01μm is more than the increase in vapor pressure when the MPL mean pore radius decreases from 0.06μm to 0.03μm. Similarly, the increase in vapor pressure when MPL mean pore radius decreases from 0.06μm to 0.03μm is more than twice the increase observed when the MPL mean pore radius decreases from 0.08μm to 0.06μm. As the MPL pore size becomes smaller, the effectiveness of the MPL in retaining water vapor in the CL is enhanced significantly.

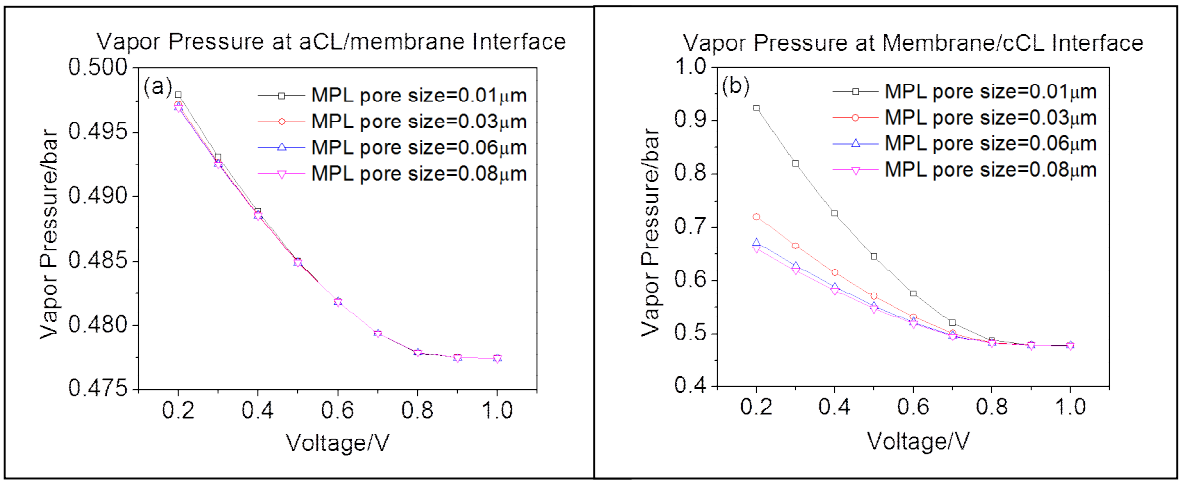

Figure 5.6: The plot of water vapor partial pressure for cells with different MPL pore radius (a) vapor pressure at aCL/membrane interface, (b) vapor pressure at membrane/cCL interface. (Operating temperature is 190°C, the cell operates with hydrogen and oxygen at 3.8% relative humidity and operating pressure of 2bar, an acid doping level of 6).

5.4 Effects of MPL Porosity

In this section, an MPL porosity of 0.3 is chosen as our base. In this section, we study the optimum MPL porosity that helps retain water in the CL. Figure 5.7 shows the ionic resistance in the membrane for cells with different MPL porosity. As the porosity of the MPL decreases, the ionic resistance in the membrane decreases. The decrease in ionic resistance increases as the MPL porosity decreases to small values. The decrease in ionic resistance when MPL porosity is decreased from 0.5 to 0.4 is less than that when MPL porosity decreases from 0.4 to 0.3. Similarly, the decrease in ionic resistance when the MPL porosity decreases from 0.4 to 0.3 is less than that when MPL porosity decreases from 0.3 to 0.2.

The partial vapor pressure at both anode and cathode interfaces of the membrane is shown in Figure 5.8. Figure 5.8a shows the vapor pressure at the anode interface while Figure 5.8b shows the vapor pressure at the cathode interface of the membrane. Unlike the effect of MPL pore size, the vapor pressure at both anode and cathode interfaces of

the membrane increases as the MPL porosity decreases. Decreasing MPL porosity helps retain both the water vapor left behind by the reactant gases and the water vapor generated by the oxygen reduction reaction.

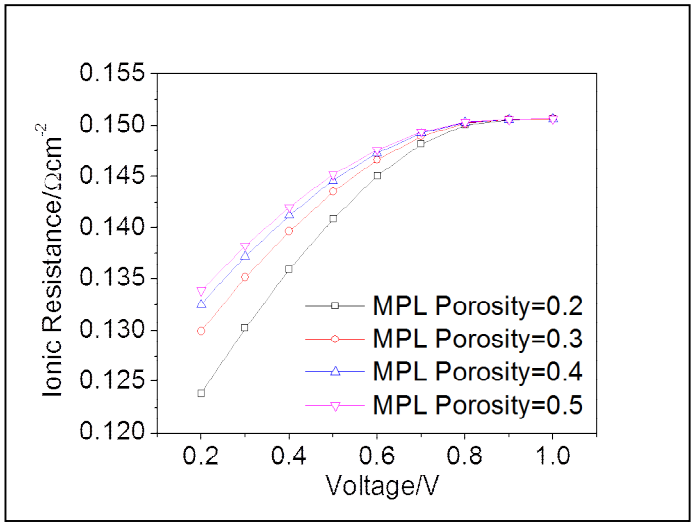

Figure 5.7: The plot of ionic resistance for cells with different MPL porosity (operating temperature is 190℃, the cell operates with hydrogen and oxygen at 3.8% relative humidity and 2 bar and acid doping level of 6).

The vapor pressure increases a lot more as the MPL porosity decreases to small value. The increase in vapor pressure when the MPL porosity decreases from 0.5 to 0.4 is less than that when the MPL porosity decreases from 0.4 to 0.3. Similarly, the increase in vapor pressure when the MPL porosity decreases from 0.4 to 0.2 is less than that when the MPL porosity decreases from 0.3 to 0.2. However, it should be noted that decreasing the MPL porosity to a small value might lead to concentration overpotential due to reduced partial pressure of O_2.

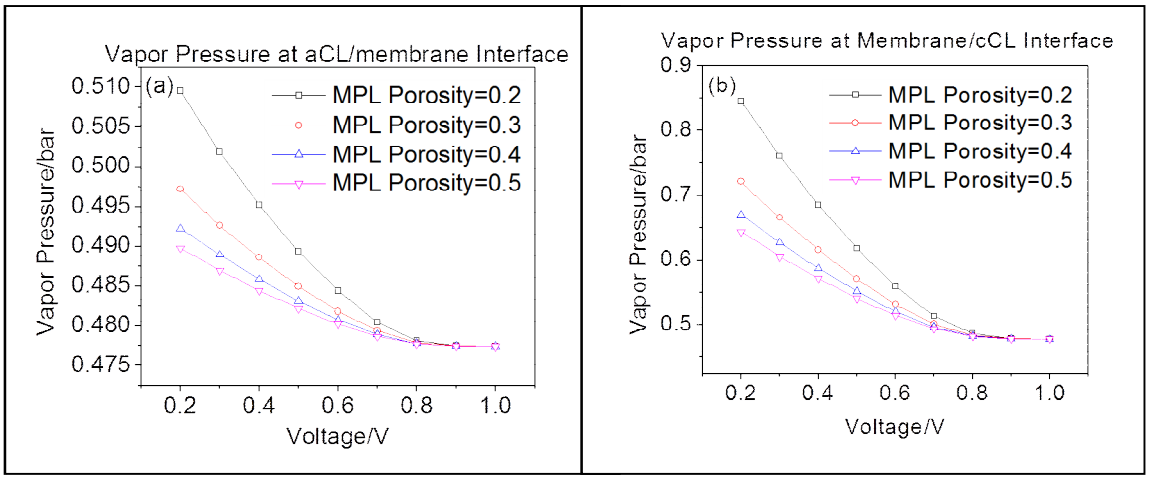

Figure 5.8: The plot partial vapor pressure for cells with different MPL porosity (a) vapor pressure at aCL/membrane interface, (b) vapor pressure at membrane/cCL interface. (operating temperature is 190℃, the cell operates with hydrogen and oxygen at 3.8% relative humidity and operating pressure of 2bar, an acid doping level of 6).

Figure 5.9 shows the current density in the membrane when the operating pressure is 1 and 2 bar respectively while the partial pressure of inlet water vapor is the same in both cases. The volume fraction of inlet water vapor when the operating pressure is 1bar is 0.4772 while the volume fraction of water vapor when the operating pressure is 2bar is 0.2386. From Figure 5.9, we observe that the optimum value of MPL porosity depends on the volume fraction of water vapor at the inlet condition and the cell voltage. For the case of when the volume fraction of water vapor at the inlet condition is 0.4772 and the cell voltage is 0.5V, the optimum value of MPL porosity is around 0.45. However, when the volume fraction of water vapor at the inlet condition is 0.2386 and the cell voltage is 0.5V, the current density in the membrane continues to increase even at low MPL porosity.

Overall, the additions of MPL to HT-PEMFC components help retain more water in the MPL and reduce the ionic resistance in the membrane. The effectiveness of the

MPL in retaining water in the CL increases as its mean pore radius decreases and also as its porosity decreases. However, the reducing the mean pore radius or the porosity to a low value might lead to dilution of the reactant gases. The dilution of the reactant gases leads to increased concentration overpotential and decreased current density in the membrane. The optimum value of MPL porosity depends on the cell operating condition such as cell voltage, operating pressure and inlet RH. The operating pressure and inlet RH determines the volume fraction of the water vapor at the inlet condition. The higher the volume fraction of water vapor at the inlet condition, the bigger the optimum value of the MPL porosity.

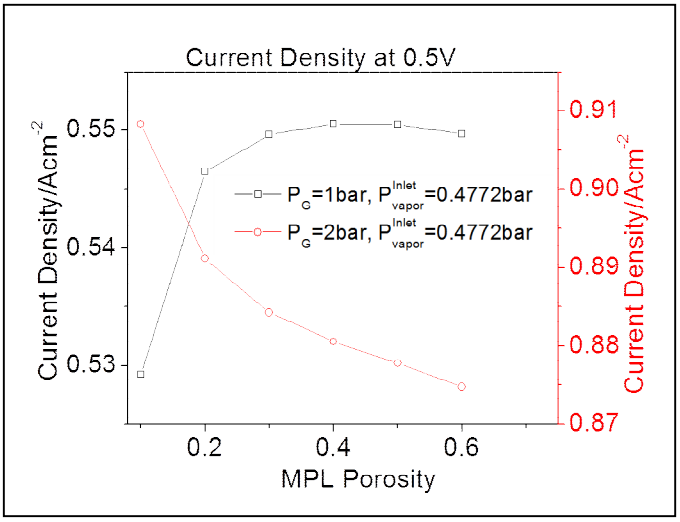

Figure 5.9: The plot of current density for varying MPL porosity at different operating pressure (operating temperature is 190°C, the cell operates with hydrogen and oxygen at 3.8% relative humidity and acid doping level of 6).

5.5 EFFECTS OF GDL POROSITY

We choose as our base case a GDL porosity of 0.6 in this study. Here, we look at how changing GDL porosity affects the amount of water retained in the CL and hence the ionic resistance in the membrane. Figure 5.10 shows the ionic resistance in the membrane

of cells with different GDL porosity. The ionic resistance of the membrane decreases as the porosity of the GDL decreases. The ionic resistance decreases with decreasing GDL porosity a lot more at lower cell voltage.

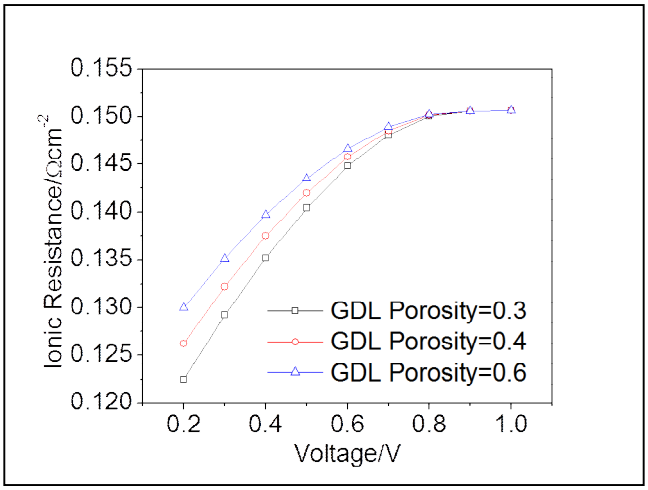

Figure 5.10: The plot of ionic resistance for cells with different GDL porosity (operating temperature is 190℃, the cell operates with hydrogen and oxygen at 3.8% relative humidity and operating pressure of 2bar, an acid doping level of 6).

At low cell voltages, the current increases and more reactant gases are consumed leaving behind water vapor from the feed gas and more water is also produced by the oxygen reduction reaction. The bigger the GDL porosity, the easier it is for the water vapor in the CL to diffuse through GDL to the gas channel. Reducing the porosity of GDL will help restrict the diffusion of water in the CL back to the gas channel through the GDL.

The plots of partial vapor pressure at both anode and cathode interface of the membrane are shown in figure 5.11. Figure 5.11a shows the plot of vapor pressure at the anode interface of the membrane while Figure 5.11b shows the plot of vapor pressure at the cathode interface of the membrane. We observe that the vapor pressure at both anode and cathode membrane interface increases as the GDL porosity is decreased. Unlike in

low temperature PEMFCs, where it is desirable that GDL helps transport liquid water produced by the oxygen reduction reaction, in HT-PEMFC, GDL porosity should not be too large as to allow unrestricted movement of water vapor in the CL but not too small as to restrict the transport of reactant gases to the CL. Restricting the transport of reactant gases to the CL will lead to increased concentration overpotential.

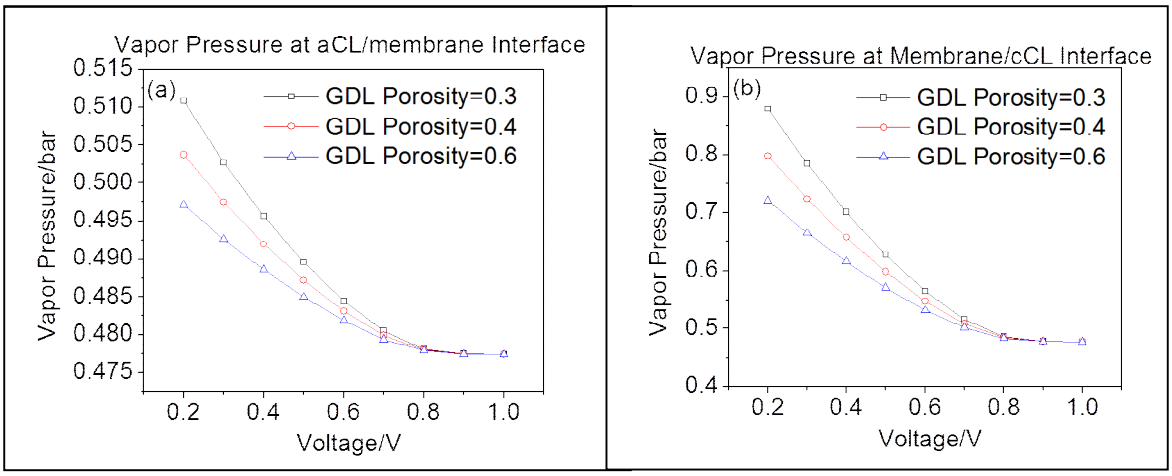

Figure 5.11: The plot partial vapor pressure for cells with different GDL porosity (a) vapor pressure at aCL/membrane interface, (b) vapor pressure at membrane/cCL interface. (operating temperature is 190℃, the cell operates with hydrogen and oxygen at 3.8% relative humidity and operating pressure of 2bar, an acid doping level of 6).

Higher GDL porosity means higher gas permeability and better reactant gas flow to the CL. At the same time, higher porosity allows an unrestricted flow of the water generated by oxygen reduction reaction from CL to the GDL. Also, higher GDL porosity means less solid region and hence lower effective electronic and thermal conductivities. Lower effective electronic conductivity increases the ohmic potential drop in the cell. Similarly, lower effective thermal conductivity means reduces the ability of the cell to dissipate the heat generated and result in higher temperature gradients within the cell. The optimum GDL porosity should be a value that is not too big or too small. It should not be

too small that it increases the concentration overpotential but not too big that it cannot help in restricting the diffusion of water generated by electrochemical reaction from CL back to the gas channel.

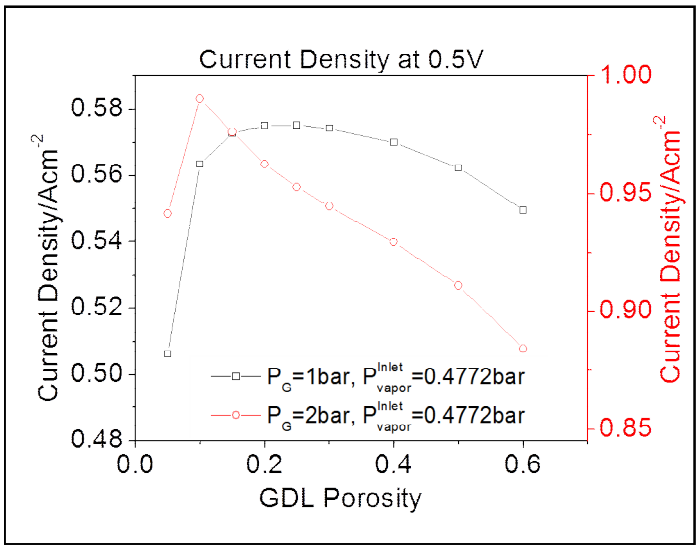

Figure 5.12: The plot of current density for varying GDL porosity at different operating pressure (operating temperature is 190℃, the cell operates with hydrogen and oxygen at 3.8% relative humidity, an acid doping level of 6).

Figure 5.12 shows the current density for varying GDL porosity for two different operating pressures while the vapor pressure at the inlet condition is the same. In Figure 5.12, for the case when the operating pressure is 1bar, the volume fraction of water vapor at inlet condition is 0.4772 while for the case of when the operating pressure is 2 bar, the volume fraction of water vapor at the inlet condition is 0.2386. Figure 5.12 shows that the optimum value of the GDL depends on the operating conditions such as the volume fraction of water vapor at the inlet condition. From Figure 5.12, the optimum value of GDL porosity is around 0.25 when the volume fraction of water vapor at the inlet condition is 0.4772 and the cell voltage is 0.5V while the optimum value of the GDL is

around 0.1 when the volume fraction of the water vapor at the inlet condition is 0.2386 and the cell voltage is 0.5V.

5.6 Effects of Mass-Transport in the Agglomerate of the CL on the Optimization of HT-PEMFC for Effective Membrane Hydration

In the model developed for the optimization of HT-PEMFC, the effectiveness factor of the agglomerate in the CL is assumed to be unity. In this section, the effectiveness factors of the agglomerate of both aCL and cCL are computed and the current density from the model with computed effectiveness factor is compared to cases where the effectiveness factor is assumed to be unity. The effectiveness factor accounts for mass transport and kinetic limitation within each agglomerate [28]. The assumption of effectiveness factor to be unity means that diffusion of the reactant gases in the agglomerate is fast and that electrochemical reaction in the CL is also fast. In practice, while the hydrogen oxidation reaction at the aCL is relatively fast, the oxygen reduction reaction at the cCL is known to be slow because of the four electrons involved in the reaction.

Figure 5.13 shows the comparison of the current density of cases with computed effectiveness factor and that where effectiveness factor is assumed to be unity. We observe that the current density of the model with computed effectiveness factor is significantly- smaller than that of the model where the effectiveness factor is assumed to be unity. This is not unexpected because the diffusion of oxygen and hydrogen in the phosphoric acid has been shown to be small [23] and the oxygen reduction reaction is generally slow. We also observe in Figure 5.13 that the optimum MPL and GDL porosity are higher for model with computed effectiveness factor compared to that where the effectiveness factor is assumed to be unity. For total gas pressure of 2bar, the MPL porosity is still increasing at MPL porosity of 0.1 when the effectiveness factor is

assumed to be unity. However, the optimum MPL porosity appears to be 0.35 when the effectiveness is computed for both aCL and cCL. Similarly, the optimum GDL porosity seems to be 0.1 for the case where effectiveness factor is assumed to be unity while the optimum GDL porosity appears to be 0.2 when the effectiveness factor is calculated.

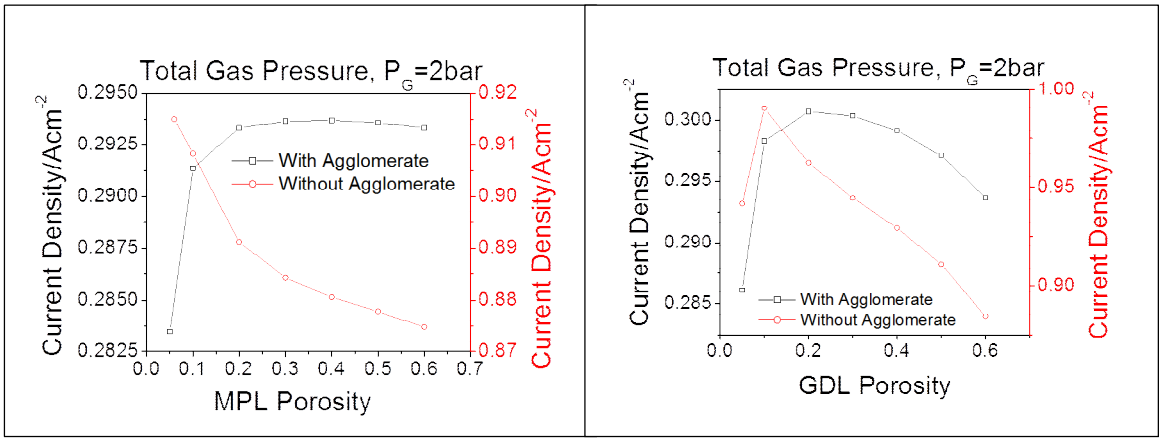

Figure 5.13: The plot of current density for cases with agglomerate and that without agglomerate for various MPL and GDL porosity (operating temperature is 190°C, the cell operates with hydrogen and oxygen at 3.8% relative humidity and operating pressure of 2bar, an acid doping level of 6).

When the effectiveness factor is assumed to be unity, optimum GDL and MPL porosity are determined by a balance between hydrating the membrane and having enough reactant gases on the surface of the agglomerate since diffusion of gases in the agglomerate is assumed to be fast. However, when the effectiveness factor is computed, the optimum GDL and MPL porosity are determined by a balance between hydrating the membrane and having enough reactant gases diffusing into the agglomerate. The mass transport in the agglomerate is the reason for the increase in the optimum GDL and MPL porosity when the effectiveness factor is computed.

Figure 5.14 shows the plot of current density for two different total gas pressure and varying GDL porosity. The total gas pressure varies while the vapor pressure is kept

constant. We observe from Figure 5.14 that optimum GDL porosity decreases as the total gas pressure increases. Increasing total gas pressure while keeping the vapor pressure constant implies an increase in the concentration of the reactant gases. Increasing the concentration of the reactant gases means more gases will be available for reaction but less water will be available to hydrate the membrane. As we decrease the GDL porosity, more of the water produced by electrochemical reaction is retained in the cCL but the transport of the reactant gases to the CL is restricted.

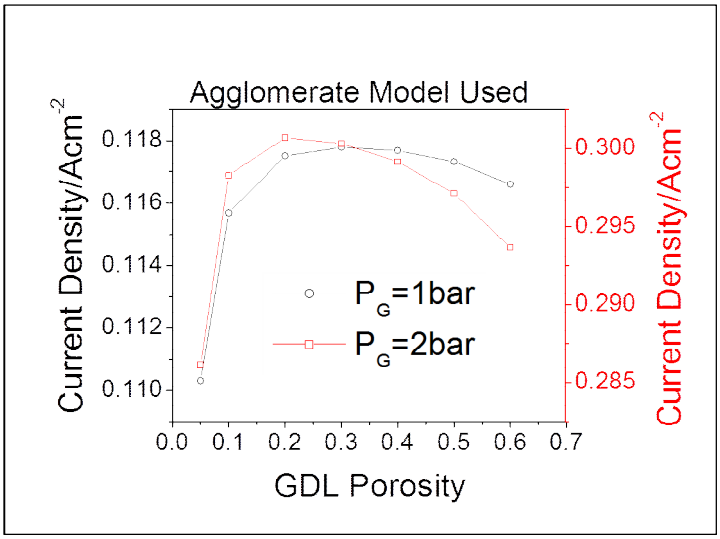

Figure 5.14: The plot of current density when agglomerate model is used for two different total gas pressure and varying GDL porosity (operating temperature is 190°C, the cell operates with hydrogen and oxygen at 3.8% relative humidity, acid doping level of 6).

As mentioned earlier, even though more water is retained in the CL as the GDL porosity decreases, the restriction on the gas transport limits the amount of gas available for reaction and increases mass transport losses. At higher gas pressure, more reactant gases will be available for reaction compared to cases with low gas pressure. Therefore

the mass transport limitation sets in early in low gas pressure compared to cases with higher gas pressure.

In this section, we have seen that the assumption of effectiveness factor to be unity over-predicts current density, optimum values of GDL and MPL porosity. However, the trends observed for model with computed effectiveness factor is the same as for model where the effectiveness factor is assumed to be unity. The optimum values of GDL and MPL porosity depends on the operating conditions such as operating pressure, temperature and cell voltage. Also, as we increase the gas concentration, the optimum values of GDL and MPL are observed to decrease.

5.7 CONCLUSION

We have developed a 1D non-isothermal model to study the optimum morphological properties of HT-PEMFC components that will help retain water in the CL by using a control- volume based approach to simulation. For the condition considered in this work: operating temperature of 190℃, operating pressure of 2 bar, an acid doping level of 6, it is found that an inlet gas composition equivalent of 100% RH at room temperature imparts only a minimal effect on the ionic resistance of the acid doped PBI membrane under high-temperature operating conditions. Humidification of the feed gases at higher temperature would be needed for humidification to make a significant impact on the ionic resistance of the membrane, and this requires complex system design and additional power consumption. We also found that increasing the inlet relative humidity beyond 6% leads to a decrease in the current density attained at a given cell potential, caused by the dilution of the reactant gases.

The additions of an MPL to HT-PEMFC components help retain more water in the MPL and reduce the ionic resistance in the membrane. The effectiveness of the MPL

in retaining water in the CL increases as its mean pore radius decreases and also as its porosity decreases. However, the MPL pore size and porosity should not be too small so that the transport of the reactant gases to the CL will be restricted; as this can lead can lead to increased concentration overpotential. The optimum value of MPL porosity depends on the operating conditions such as volume fraction of water vapor at inlet condition, cell voltage and the operating condition. When the operating pressure is 1 bar, the optimum value of MPL porosity is around 0.45. Reducing GDL porosity is also found to increase the vapor pressure in the CL. Similar to the MPL porosity, the optimum value of GDL porosity depends on the operating conditions such as volume fraction of the water vapor and the operating pressure. When the operating pressure of 1bar, the cell voltage is 0.5V and the volume fraction of the water vapor is 0.4772, the optimum GDL porosity is 0.25.

The effectiveness factor of the agglomerate in the CL is assumed to be unity is the model for the optimization of HT-PEMFC. To ascertain the effects of the assumption, we computed the effectiveness factor and then compare the current from model with computed effectiveness factor to that where the effectiveness is assumed to be unity. The assumption of effectiveness factor to be unity over-predicts current density, optimum values of GDL and MPL porosity. However, the trends observed for model with computed effectiveness factor is the same as for model where the effectiveness factor is assumed to be unity. The optimum values of GDL and MPL porosity depends on the operating conditions such as operating pressure, temperature and cell voltage. Also, as we increase the gas concentration, the optimum values of GDL and MPL are observed to decrease.

Chapter 6: Summary and Future Works

In this dissertation, we developed two major lines of numerical investigations: understanding water management in typical PEM materials operating at less than 100°C under transient condition, and evaluating how to retain water in the separator for high-temperature operation with a different class of materials. In the model for low-temperature PEMFC, we use experimentally measured capillary pressure as opposed to the Leverett-J function originally derived for isotropic and homogeneous soil used in almost all the models in the literature. The effects of hysteresis observed in the experimentally measured capillary pressure is investigated and shown to have minimal effects on the modeling predictions.

With the low-temperature model, we are also able to explain the observed difference in the time constant between membrane hydration (occurs when current increases/voltage decreases) and membrane dehydration (occurs when current decreases/voltage increases) in response to transient input. MEA HFR measured at Los Alamos National Laboratory shows that membrane hydration occurs very fast while membrane dehydration occurs rather slowly. Our model predicts that the dominating factors responsible for membrane hydration time constant are different from those responsible for membrane dehydration time constant. The membrane hydration time constant is mainly determined by the rate of the electrochemical reaction, and how fast the water diffuses across the membrane. Because water is generated in the CL, increased water generation, which occurs when current increases quickly increases the average water content of the membrane and thus results in a membrane hydration time constant that is related to water diffusing back across the membrane. On the other hand, the membrane dehydration time constant is mainly determined by how quickly the water

phase (vapor or liquid) in contact with the membrane reaches steady state, in series with water redistributing in the membrane. When current decreases, less water is produced in the CL and the water already in the CL moves slowly out of the catalyst layer. As long as the water is still moving out of the CL, membrane water content will not be at steady state and thus we observe the slower membrane dehydration time constant.

Our model also predicts that the use of MPL slows membrane dehydration, especially in the first few hundred seconds when current decreases. However, the use of MPL does not show any significant effect on the membrane hydration time constant when current increases. MPL has been shown to partially block the transport of water out of the CL and therefore slows down the transport of water out of the CL. As explained earlier, as long as the water is still moving out of the CL, the water content in the membrane will not reach steady state. However, since increased water generation caused by the increase in current occurs in the CL, the use of MPL does not have significant effects on the membrane hydration time constant.

In our second model developed for the optimization of HT-PEMFC, we obtain a fairly good match with experimental data from Sousa et al. [100]. Our model predicts that humidification of the feed gas at room temperature has minimal effects on the ionic resistance of the membrane used in the HT-PEMFC. Feed gases must be humidified at higher temperature to have effects on the ionic resistance. However, Humidification at such a higher temperature will require complex system design and additional power consumption. It is therefore important to keep the water generated by the electrochemical reaction as close as possible to the membrane to hydration the membrane so as to reduce the ionic resistance and thereby increase cell performance. Our model also predicts increasing inlet relative humidity beyond some values which will depend on other cell

parameters might lead to dilution the reactant gases and consequently low cell performance.

The use of cathode MPL helps keep the water generated close to the membrane and decreasing the MPL porosity and pore size will increase the effectiveness of the MPL in keep the water generated close to the membrane. However, because decreasing the MPL porosity and pore size will restrict the gas transport to the CL where the electrochemical reaction takes place; there must be an optimum value for both MPL porosity and pore size. Our model predicts that the optimum value of the MPL porosity depends on the operating conditions of the cell. Similarly, the decreasing the GDL porosity helps keep water close to the membrane and the optimum value of the GDL porosity depends on the operating conditions of the cell.

While isothermal condition assumed in the model for low-temperature is valid for a single cell, accounting for the temperature variation in the cell will be important in the cell stacks. The effects of non-isothermal on transient response of PEMFC to transient input will be considered in the future model.

Appendix

APPENDIX A: POLYNOMIALS FITTED TO THE EXPERIMENTALLY MEASURED CAPILLARY PRESSURE OF COMPRESSED TORAY 120C

The polynomials fitted to the experimentally measured capillary pressure of compressed Toray 120C by Gostick *et al.*[81] are as follows:

Secondary injection: Compressed Toray 120C

$$p_c = -6.815853557x + 9476.607940x^4 + 114.8427251x^2 - 1245.668744x^3 - 53235.90920x^5$$
$$+2.278741162e5x^6 - 7.579214265e5x^7 + 1.981630094e6x^8 - 4.094976567e6x^9 + 6.688276451e6x^{10}$$
$$-8.586342162e6x^{11} + 8.560416009e6x^{12} - 6.490861587e6x^{13} + 3.616006831e6x^{14}$$
$$-1.395166990e6x^{15} + 3.329950426e5x^{16} - 37033.19125x^{17} + .1306720762$$

Primary withdrawal: Compressed Toray 120C

$$p_c = -11.21390501x + 15417.52950x^4 + 190.4837207x^2 - 2051.851672x^3 - 85246.91137x^5$$
$$+3.582225366e5x^6 - 1.167147588e6x^7 + 2.983554838e6x^8 - 6.017345300e6x^9 + 9.576060837e6x^{10}$$
$$-1.195942393e7x^{11} + 1.158145141e7x^{12} - 8.517175868e6x^{13} + 4.595434584e6x^{14}$$
$$-1.714842892e6x^{15} + 3.953203277e5x^{16} - 42407.35124x^{17} + .3824473506$$

APPENDIX B: NOMENCLATURES USED IN THE DISSERTATION

a Water vapor activity

$a_{1,2}^{o}$ Specific interfacial reaction area in cm^{-1}

C_s Reactant gas concentration at the catalyst surface

C^* Reference concentration at STP conditions

D_{λ}^{eff} Effective diffusion coefficient in the membrane in $cm^2 s^{-1}$

$D_{k,i}^{eff}$ Knudsen diffusion coefficient in $cm^2 s^{-1}$

$D_{i,j}^{eff}$ Binary diffusion coefficient in $cm^2 s^{-1}$

e_i Volume fraction of the ionomer

e_s Volume fraction of the solid electronically conductive phase

e_G Gas phase volume fraction

e_o Bulk porosity

E Effectiveness factor

E_a Activation energy

F Faraday's constant

H_{H_2} Henry's constant for hydrogen in the phosphoric acid

H_{O_2} Henry's constant for oxygen in the phosphoric acid

i_{cell} Fuel cell total current density in Acm^{-2}

i_o Exchange current density in Acm^{-2}

i_1 Current density carried in the electronic phase in Acm^{-2}

i_m Current density carried in the ionic phase in Acm^{-2}

i_h Transfer current for reaction, h. h can be HOR at the anode catalyst layer or ORR at the cathode catalyst layer

k' Kinetic portion of the Thiele modulus

k_e Evaporation rate constant in $(bar.s)^{-1}$

k_c Condensation rate constant in s^{-1}

k_r Relative permeability

k_{sat} Absolute permeability in cm^2

k_G Permeability of the total gas in cm^2

k_T^{eff} Effective thermal conductivity of the system in $bar.s^{-1}.cm^{-1}.k^{-1}$

$k_{a/d}^{mem}$ Rate of absorption/desorption of water from the membrane in s^{-1}

M_o Molar weight of water in $g.mol^{-1}$

N_{wm} Superficial flux density of water in the membrane in $mol.cm^{-1}.s^{-1}$

N_i Molar flux of gas species i in $mol.cm^{-1}.s^{-1}$

p_{H_2} Partial pressure of the hydrogen gas at the anode in bar

$p_{H_2}^{ref}$ Reference partial pressure of the hydrogen gas in bar

p_{O_2} Partial pressure of the oxygen gas at the cathode in bar

$p_{O_2}^{ref}$ Reference partial pressure of the oxygen gas in bar

p_0 Partial pressure of water vapor in bar

p_0^{sat} Saturate vapor pressure in bar

p_G Total gas pressure in bar

p_L Liquid water pressure in bar

p_c Capillary pressure in bar

r_p Mean pore radius of the porous medium, cm

R Gas constant in $cm^3.bar.k^{-1}.mol^{-1}$

R_{Agg} Radius of the agglomerate in cm

s Liquid water saturation

T Absolute temperature in K

U Thermodynamic equilibrium potential in V

U^{θ} Standard potential in V

$\overline{V}_m$ Molar volume of the dry membrane in $cm^3.mol^{-1}$

$w_{H_3PO_4}$ Mass fraction of the phosphoric acid

$x_{H_3PO_4}$ Mole fraction of the phosphoric acid

Greek

α_a Anodic transfer coefficient

α_c Cathodic transfer coefficient

η Activation overpotential in V

σ_s Electronic conductivity in Scm^{-1}

σ_m Proton conductivity in Scm^{-1}

σ_o pre-exponential factor of proton conductivity for the acid-doped PBI membrane

σ_w Surface tension of water in $dyn.cm^{-1}$

ϕ_1 Electric potential in the electronically conductive solid phase

ϕ_2 Electric potential in the ionomer

ϕ_{mt} Mass transfer portion of the Thiele modulus

ϕ Thiele Modulus for the system

ψ_{Agg}^{β} The permeation coefficient of reactant gas, β into the agglomerate in $mol.bar^{-1}.cm^{-1}.s^{-1}$

$\mu_{\varepsilon}^{\delta}$ Electrochemical potential of species ε in domain δ

μ_L Dynamic viscosity of liquid water in $bar.s$

μ_G Dynamic viscosity of the total gas in $bar.s$

γ Reaction order for the elementary charge transfer step

λ Water content in the membrane

ξ Electro-osmotic drag

ρ_o Density of water in gcm^{-3}

ρ_G Density of the total gas pressure in gcm^{-3}

θ^{Ω} Contact angle in domain Ω

τ Tortuosity of the porous medium

References

1. Goodstein, D., *Out of Gas: The End of the Age of Oil*2005: W.W. Norton & Company. 148.
2. Barbir, F., *PEM Fuel Cells: Theory and Practice Sustainable World Series*2005.
3. Weber, A.Z. and J. Newman, *Transport in polymer-electrolyte membranes. I. Physical model.* Journal of the Electrochemical Society, 2003. **150**(7): p. 1008-1015.
4. Cook, B., *An Introduction to Fuel Cells and Hydrogen Technology*, 2001.
5. Larminie, J. and A. Dicks, *Fuel Cell Systems Explained, Second Edition*. 2nd Edition ed2003: John Wiley & Sons Ltd.
6. Wikipedia. *Apollo 11*. Available from: http://en.wikipedia.org/wiki/Apollo_11.
7. Hickner, M.A., *Transport and Structure in Fuel Cell Proton Exchange Membranes*, in *Dept of Chemical Engineering*2003, Virginia Polytechnic Institute and State University: Blacksburg. p. 237.
8. Zhang, J., ed. *PEM Fuel Cell Electrocatalysts and Catalyst Layers: Fundamentals and Applications* 2008.
9. DOE-FUEL-CELL-TECHNOLOGIES-PROGRAM, *Clean, Efficient, and Reliable Heat and Power for the 21st Century.* 2010.
10. Weber, A.Z., *Modeling water management in polymer-electrolyte fuel cells*, in *Dept of Chemical Engineering*2004, University of California, Berkeley: Berkeley. p. 434.
11. Gerteisen, D., T. Heilmann, and C. Ziegler, *Modeling the phenomena of dehydration and flooding of a polymer electrolyte membrane fuel cell.* Journal of Power Sources, 2009. **187**(1): p. 165-181.
12. Qu, S., et al., *Experimental and modeling study on water dynamic transport of the proton exchange membrane fuel cell under transient air flow and load change.* Journal of Power Sources, 2010. **195**(19): p. 6629-6636.
13. Jain, P., L.T. Biegler, and M.S. Jhon, *Sensitivity of PEFC Models to Cathode Layer Microstructure.* Journal of the Electrochemical Society, 2010. **157**(8): p. B1222-B1229.
14. Mukundan, R. and R.L. Borup, *Visualising Liquid Water in PEM Fuel Cells Using Neutron Imaging.* Fuel Cells, 2009. **9**(5): p. 499-505.
15. Olapade, P.O., et al., *Modeling the Dynamic Behavior of Proton-Exchange Membrane Fuel Cells.* Journal of the Electrochemical Society, 2011. **158**(5): p. B536-B549.
16. Ziegler, C., T. Heilmann, and D. Gerteisen, *Experimental Study of Two-Phase Transients in PEMFCs.* Journal of the Electrochemical Society, 2008. **155**(4): p. B349-B355.
17. Li, Q., et al., *Approaches and Recent Development of Polymer Electrolyte Membranes for Fuel Cells Operating above 100 oC.* Chemistry of Materials, 2003. **15**(26): p. 4896-4915.

18. Zhang, J., et al., *High temperature PEM fuel cells.* Journal of Power Sources, 2006. **160**(2): p. 872-891.
19. Sinha, P.K., C.-Y. Wang, and U. Beuscher, *Transport phenomena in elevated temperature PEM fuel cells.* Journal of the Electrochemical Society, 2007. **154**(1): p. 106-116.
20. Li, Q., et al., *PBI-Based Polymer Membranes for High Temperature Fuel Cells – Preparation, Characterization and Fuel Cell Demonstration.* Fuel Cells, 2004. **4**(3): p. 147-159.
21. Cheddie, D. and N. Munroe, *Mathematical model of a PEMFC using a PBI membrane.* Energy Conversion and Management, 2006. **47**(11-12): p. 1490-1504.
22. Ma, Y.L., et al., *Conductivity of PBI Membranes for High-Temperature Polymer Electrolyte Fuel Cells.* Journal of the Electrochemical Society, 2004. **151**(1): p. A8-A16.
23. Weng, D., et al., *Electro-osmotic Drag Coefficient of Water and Methanol in Polymer Electrolytes at Elevated Temperatures.* Journal of the Electrochemical Society, 1996. **143**(4): p. 1260-1263.
24. Wainright, J.S., et al., *Acid-Doped Polybenzimidazoles: A New Polymer Electrolyte.* Journal of the Electrochemical Society, 1995. **142**(7): p. L121-L123.
25. Wu, H., *Mathematical Modeling of Transient Transport Phenomena in PEM Fuel Cells*, in *Dept of Mechanical Engineering*2009, University of Waterloo: Ontario. p. 188.
26. He, R., et al., *Proton conductivity of phosphoric acid doped polybenzimidazole and its composites with inorganic proton conductors.* Journal of Membrane Science, 2003. **226**(1-2): p. 169-184.
27. Wu, G., et al., *High-Performance Electrocatalysts for Oxygen Reduction Derived from Polyaniline, Iron, and Cobalt.* Science, 2011. **332**(6028): p. 443-447.
28. Weber, A.Z. and J. Newman, *Effects of Microporous Layers in Polymer Electrolyte Fuel Cells.* Journal of the Electrochemical Society, 2005. **152**(4): p. A677-A688.
29. Srinivasan, S., *Fuel Cells- From Fundamentals to Applications*2006: Springer Science+Business Media, LLC
30. Mench, M., *Fuel Cell Engines*2008: John Wiley & Sons, Inc.
31. Newman, J. and K.E. Thomas-Alyea, *Electrochemical Systems*. Third Edition ed2004, New Jersy: John Wiley and Sons.
32. Ticianelli, E.A., et al., *Methods to advance technology of proton exchange membrane fuel cells.* Journal of the Electrochemical Society, 1988. **135**(Compendex): p. 2209-2214.
33. Parthasarathy, A., et al., *Pressure Dependence of the Oxygen Reduction Reaction at the Platinum Microelectrode/Nafion Interface: Electrode Kinetics and Mass Transport.* Journal of the Electrochemical Society, 1992. **139**(10): p. 2856-2862.
34. Parthasarathy, A., et al., *Temperature dependence of the electrode kinetics of oxygen reduction at the platinum/nafion(R) interface - a microelectrode*

investigation. Journal of the Electrochemical Society, 1992. **139**(Compendex): p. 2530-2537.
35. Paganin, V.A., E.A. Ticianelli, and E.R. Gonzalez, *Development and electrochemical studies of gas diffusion electrodes for polymer electrolyte fuel cells.* Journal of Applied Electrochemistry, 1996. **26**(3): p. 297-304.
36. Amphlett, J.C., et al., *Performance modeling of the Ballard Mark IV solid polymer electrolyte fuel cell II. Empirical model development.* Journal of the Electrochemical Society, 1995. **142**(1): p. 9-15.
37. Springer, T.E., T.A. Zawodzinski, and S. Gottesfeld, *Polymer Electrolyte Fuel Cell Model.* Journal of The Electrochemical Society, 1991. **138**(8): p. 2334-2342.
38. Bernardi, D.M. and M.W. Verbrugge, *Mathematical model of a gas diffusion electrode bonded to a polymer electrolyte.* AIChE Journal, 1991. **37**(8): p. 1151-1163.
39. Bernardi, D.M. and M.W. Verbrugge, *Mathematical model of the solid-polymer-electrolyte fuel cell.* Journal of the Electrochemical Society, 1992. **139**(9): p. 2477-2491.
40. Nguyen, T.V. and R.E. White, *Water and heat management model for proton-exchange-membrane fuel cells.* Journal of the Electrochemical Society, 1993. **140**(8): p. 2178-2186.
41. Amphlett, J.C., et al., *Performance modeling of the Ballard Mark IV solid polymer electrolyte fuel cell I. Mechanistic model development.* Journal of the Electrochemical Society, 1995. **142**(1): p. 1-8.
42. Okada, T., Gang Xie, Yoshikazu Tanabe, *Theory of water management at the anode side of polymer electrolyte*

fuel cell membranes. Journal of Electroanalytical Chemistry, 1996. **413**: p. 49-65.
43. Okada, T., G. Xie, and Y. Tanabe, *Theory of water management at the anode side of polymer electrolyte fuel cell membranes.* Journal of Electroanalytical Chemistry, 1996. **413**(1-2): p. 49-65.
44. Okada, T., G. Xie, and M. Meeg, *Simulation for water management in membranes for polymer electrolyte fuel cells.* Electrochimica Acta, 1998. **43**(14-15): p. 2141-2155.
45. van Bussel, H.P.L.H., F.G.H. Koene, and R.K.A.M. Mallant, *Dynamic model of solid polymer fuel cell water management.* Journal of Power Sources, 1998. **71**(1-2): p. 218-222.
46. Yi, J.S. and T.V. Nguyen, *Along-the-channel model for proton exchange membrane fuel cells.* Journal of the Electrochemical Society, 1998. **145**(4): p. 1149-1159.
47. Hsing, I.M. and P. Futerko, *Two-dimensional simulation of water transport in polymer electrolyte fuel cells.* Chemical Engineering Science, 2000. **55**(19): p. 4209-4218.
48. Dannenberg, K., P. Ekdunge, and G. Lindbergh, *Mathematical model of the PEMFC.* Journal of Applied Electrochemistry, 2000. **30**(12): p. 1377-1387.

49. Weber, A.Z. and J. Newman, *Modeling transport in polymer-electrolyte fuel cells.* Chemical Reviews, 2004. **104**(10): p. 4679-4726.
50. Um, S., C.Y. Wang, and K.S. Chen, *Computational Fluid Dynamics Modeling of Proton Exchange Membrane Fuel Cells.* Journal of the Electrochemical Society, 2000. **147**(12): p. 4485-4493.
51. Singh, D., D.M. Lu, and N. Djilali, *Two-dimensional analysis of mass transport in proton exchange membrane fuel cells.* International Journal of Engineering Science, 1999. **37**(4): p. 431-452.
52. Thampan, T., et al., *Modeling of conductive transport in proton-exchange membranes for fuel cells.* Journal of the Electrochemical Society, 2000. **147**(9): p. 3242-3250.
53. Weber, A.Z. and J. Newman, *Transport in Polymer-Electrolyte Membranes III. Model Validation in a Simple Fuel-Cell Model.* Journal of the Electrochemical Society, 2004. **151**(2): p. 326-339.
54. Weber, A.Z. and J. Newman, *Transport in Polymer-Electrolyte Membranes: II. Mathematical Model.* Journal of the Electrochemical Society, 2004. **151**(2): p. 311-325.
55. Janssen, G.J.M., *A Phenomenological Model of Water Transport in a Proton Exchange Membrane Fuel Cell.* Journal of The Electrochemical Society, 2001. **148**(12): p. A1313-A1323.
56. Rowe, A. and X. Li, *Mathematical modeling of proton exchange membrane fuel cells.* Journal of Power Sources, 2001. **102**(1-2): p. 82-96.
57. Weber, A.Z. and J. Newman, *Chapter Two: Macroscopic Modeling of Polymer-Electrolyte Membranes*, in *Advances in Fuel Cells*, K.D.K. T.S. Zhao and N. Trung Van, Editors. 2007, Elsevier Science. p. 47-117.
58. Weber, A.Z., et al., *Modeling Water Management in Polymer-Electrolyte Fuel Cells*, in *Modern Aspects of Electrochemistry*, M. Schlesinger, Editor 2009, Springer: New York. p. 273-416.
59. Wang, X. and T. Van Nguyen, *Modeling the Effects of Capillary Property of Porous Media on the Performance of the Cathode of a PEMFC.* Journal of the Electrochemical Society, 2008. **155**(11): p. B1085-B1092.
60. Wang, X., et al., *A Modeling Study of the Effects of the Properties of Anode Porous Layer on the Performance of a PEM Fuel Cell.* ECS Transactions, 2009. **25**(1): p. 29-38.
61. Wang, X. and T. Van Nguyen, *Modeling the Effects of the Microporous Layer on the Net Water Transport Rate Across the Membrane in a PEM Fuel Cell.* Journal of the Electrochemical Society, 2010. **157**(4): p. B496-B505.
62. Balliet, R.J. and J. Newman, *Cold Start of a Polymer-Electrolyte Fuel Cell I. Development of a Two-Dimensional Model.* Journal of the Electrochemical Society, 2011. **158**(8): p. B927-B938.
63. Yoon, W. and X. Huang, *A Multiphysics Model of PEM Fuel Cell Incorporating the Cell Compression Effects.* Journal of the Electrochemical Society, 2010. **157**(5): p. B680-B690.

64. Wu, H., P. Berg, and X. Li, *Modeling of PEMFC Transients with Finite-Rate Phase-Transfer Processes.* Journal of the Electrochemical Society, 2010. **157**(1): p. B1-B12.
65. Inamuddin, et al., *Three dimensional numerical investigations for the effects of gas diffusion layer on PEM fuel cell performance.* Renewable Energy, 2010. **In Press, Corrected Proof**.
66. Manso, A.P., et al., *Numerical analysis of the influence of the channel cross-section aspect ratio on the performance of a PEM fuel cell with serpentine flow field design.* International Journal of Hydrogen Energy, 2011. **In Press, Corrected Proof**.
67. Wu, H., P. Berg, and X. Li, *Steady and unsteady 3D non-isothermal modeling of PEM fuel cells with the effect of non-equilibrium phase transfer.* Applied Energy, 2009. **In Press, Corrected Proof**.
68. Shah, A.A., et al., *Transient non-isothermal model of a polymer electrolyte fuel cell.* Journal of Power Sources, 2007. **163**(2): p. 793-806.
69. Promislow, K., et al., *Two-phase unit cell model for slow transients in polymer electrolyte membrane fuel cells.* Journal of the Electrochemical Society, 2008. **155**(7): p. A494-A504.
70. Natarajan, D. and T. Van Nguyen, *A Two-Dimensional, Two-Phase, Multicomponent, Transient Model for the Cathode of a Proton Exchange Membrane Fuel Cell Using Conventional Gas Distributors.* Journal of the Electrochemical Society, 2001. **148**(12): p. A1324-A1335.
71. Wu, H., P. Berg, and X. Li, *Non-isothermal transient modeling of water transport in PEM fuel cells.* Journal of Power Sources, 2007. **165**(1): p. 232-243.
72. Meng, H., *Numerical investigation of transient responses of a PEM fuel cell using a two-phase non-isothermal mixed-domain model.* Journal of Power Sources, 2007. **171**(2): p. 738-746.
73. Qu, S., et al., *Experimental and modeling study on water dynamic transport of the proton exchange membrane fuel cell under transient air flow and load change.* Journal of Power Sources, 2010. **In Press, Accepted Manuscript**.
74. Wang, Y. and C.-Y. Wang, *Transient analysis of polymer electrolyte fuel cells.* Electrochimica Acta, 2005. **50**(6): p. 1307-1315.
75. Wang, X.-D., et al., *Transient response of PEM fuel cells with parallel and interdigitated flow field designs.* International Journal of Heat and Mass Transfer, 2011. **In Press, Corrected Proof**.
76. Amphlett, J.C., et al., *Model predicting transient responses of proton exchange membrane fuel cells.* Journal of Power Sources, 1996. **61**(1-2): p. 183-188.
77. Satterfield, M.B. and J.B. Benziger, *Non-Fickian Water Vapor Sorption Dynamics by Nafion Membranes.* The Journal of Physical Chemistry B, 2008. **112**(12): p. 3693-3704.
78. Fuller, T.F., *Solid Oxide Electrolyte Fuel Cell*, in *Department of Chemical Engineering*1992, University of california, Berkeley: Berkeley. p. 254.

79. Kumbur, E.C., K.V. Sharp, and M.M. Mench, *Validated Leverett Approach for Multiphase Flow in PEFC Diffusion Media: III. Temperature Effect and Unified Approach.* Journal of the Electrochemical Society, 2007. **154**(12): p. B1315-B1324.
80. Fairweather, J.D., et al., *A microfluidic approach for measuring capillary pressure in PEMFC gas diffusion layers.* Electrochemistry Communications, 2007. **9**(9): p. 2340-2345.
81. Gostick, J.T., et al., *Wettability and capillary behavior of fibrous gas diffusion media for polymer electrolyte membrane fuel cells.* Journal of Power Sources, 2009. **194**(1): p. 433-444.
82. Harkness, I.R., et al., *The use of a novel water porosimeter to predict the water handling behaviour of gas diffusion media used in polymer electrolyte fuel cells.* Journal of Power Sources, 2009. **193**(1): p. 122-129.
83. Weber, A.Z., *Improved modeling and understanding of diffusion-media wettability on polymer-electrolyte-fuel-cell performance.* Journal of Power Sources, 2010. **195**(16): p. 5292-5304.
84. Qi, Z. and A. Kaufman, *Improvement of water management by a microporous sublayer for PEM fuel cells.* Journal of Power Sources, 2002. **109**(1): p. 38-46.
85. Chen, J., T. Matsuura, and M. Hori, *Novel gas diffusion layer with water management function for PEMFC.* Journal of Power Sources, 2004. **131**(1-2): p. 155-161.
86. Park, G.-G., et al., *Effect of PTFE contents in the gas diffusion media on the performance of PEMFC.* Journal of Power Sources, 2004. **131**(1-2): p. 182-187.
87. Ahn, M., et al., *Influence of hydrophilicity in micro-porous layer for polymer electrolyte membrane fuel cells.* Electrochimica Acta, 2011. **56**(5): p. 2450-2457.
88. Gostick, J.T., et al., *On the role of the microporous layer in PEMFC operation.* Electrochemistry Communications, 2009. **11**(3): p. 576-579.
89. Tseng, C.-J. and S.-K. Lo, *Effects of microstructure characteristics of gas diffusion layer and microporous layer on the performance of PEMFC.* Energy Conversion and Management, 2010. **51**(4): p. 677-684.
90. Karan, K., et al., *An Experimental Investigation of Water Transport in PEMFCs.* Electrochemical and Solid-State Letters, 2007. **10**(2): p. B34-B38.
91. Lin, G. and T. Van Nguyen, *Effect of Thickness and Hydrophobic Polymer Content of the Gas Diffusion Layer on Electrode Flooding Level in a PEMFC.* Journal of the Electrochemical Society, 2005. **152**(10): p. A1942-A1948.
92. Nam, J.H. and M. Kaviany, *Effective diffusivity and water-saturation distribution in single- and two-layer PEMFC diffusion medium.* International Journal of Heat and Mass Transfer, 2003. **46**(24): p. 4595-4611.
93. Pasaogullari, U. and C.-Y. Wang, *Two-phase transport and the role of micro-porous layer in polymer electrolyte fuel cells.* Electrochimica Acta, 2004. **49**(25): p. 4359-4369.

94. Kang, K. and H. Ju, *Numerical modeling and analysis of micro-porous layer effects in polymer electrolyte fuel cells.* Journal of Power Sources, 2009. **194**(2): p. 763-773.
95. Cheddie, D. and N. Munroe, *Parametric model of an intermediate temperature PEMFC.* Journal of Power Sources, 2006. **156**(2): p. 414-423.
96. Cheddie, D.F. and N.D.H. Munroe, *Three dimensional modeling of high temperature PEM fuel cells.* Journal of Power Sources, 2006. **160**(1): p. 215-223.
97. Ubong, E.U., Z. Shi, and X. Wang, *Three-Dimensional Modeling and Experimental Study of a High Temperature PBI-Based PEM Fuel Cell.* Journal of the Electrochemical Society, 2009. **156**(10): p. B1276-B1282.
98. Peng, J. and S.J. Lee, *Numerical simulation of proton exchange membrane fuel cells at high operating temperature.* Journal of Power Sources, 2006. **162**(2): p. 1182-1191.
99. Peng, J., J.Y. Shin, and T.W. Song, *Transient response of high temperature PEM fuel cell.* Journal of Power Sources, 2008. **179**(1): p. 220-231.
100. Sousa, T., M. Mamlouk, and K. Scott, *An isothermal model of a laboratory intermediate temperature fuel cell using PBI doped phosphoric acid membranes.* Chemical Engineering Science, 2010. **65**(8): p. 2513-2530.
101. Sousa, T., M. Mamlouk, and K. Scott, *A dynamic non-isothermal model of a laboratory intermediate temperature fuel cell using PBI doped phosphoric acid membranes.* International Journal of Hydrogen Energy, 2010. **In Press, Corrected Proof**.
102. Jiao, K. and X. Li, *A Three-Dimensional Non-isothermal Model of High Temperature Proton Exchange Membrane Fuel Cells with Phosphoric Acid Doped Polybenzimidazole Membranes.* Fuel Cells, 2010. **10**(3): p. 351-362.
103. Bergmann, A., D. Gerteisen, and T. Kurz, *Modelling of CO Poisoning and its Dynamics in HTPEM Fuel Cells.* Fuel Cells, 2010. **10**(2): p. 278-287.
104. Jiao, K., I.E. Alaefour, and X. Li, *Three-dimensional non-isothermal modeling of carbon monoxide poisoning in high temperature proton exchange membrane fuel cells with phosphoric acid doped polybenzimidazole membranes.* Fuel, 2011. **90**(2): p. 568-582.
105. Newman, J. and W. Tiedemann, *Porous-electrode theory with battery applications.* AIChE Journal, 1975. **21**(1): p. 25-41.
106. Jiao, K. and X. Li, *Water transport in polymer electrolyte membrane fuel cells.* Progress in Energy and Combustion Science, 2010. **In Press, Corrected Proof**.
107. Zawodzinski, T.A., Jr., et al., *Water uptake by and transport through Nafion(R) 117 membranes.* Journal of the Electrochemical Society, 1993. **140**(4): p. 1041-1047.
108. Zawodzinski, T.A., Jr., et al., *Comparative study of water uptake by and transport through ionomeric fuel cell membranes.* Journal of the Electrochemical Society, 1993. **140**(7): p. 1981-1985.

109. Fuller, T.F. and J. Newman, *Experimental Determination of the Transport Number of Water in Nafion 117 Membrane.* Journal of The Electrochemical Society, 1992. **139**(5): p. 1332-1337.
110. Newman, T.F.F.a.J., *Experimental Determination of the Transport Number of Water*
in Nation 117 Membrane. J. Electrochem. Soc, 1992. **139**.
111. Weber, A.Z. and J. Newman, *Modeling gas-phase flow in porous media.* International Communications in Heat and Mass Transfer, 2005. **32**(7): p. 855-860.
112. Fritz, D.L. and J.S. Allen, *Evaporation Modeling for Proton Exchange Membrane Fuel Cells.* ECS Transactions, 2009. **25**(1): p. 49-58.
113. Gostick, J.T., et al., *Direct measurement of the capillary pressure characteristics of water-air-gas diffusion layer systems for PEM fuel cells.* Electrochemistry Communications, 2008. **10**(10): p. 1520-1523.
114. Leverett, M.C., *Capillary behavior in porous solids.* Trans. AIME (Am. Inst. Min. Metall. Eng.), 1941. **142**: p. 152–169.
115. Kulikovsky, A.A., *Quasi-3D Modeling of Water Transport in Polymer Electrolyte Fuel Cells.* Journal of The Electrochemical Society, 2003. **150**(11): p. A1432-A1439.
116. Ge, S., et al., *Absorption, desorption, and transport of water in polymer electrolyte membranes for fuel cells.* Journal of the Electrochemical Society, 2005. **152**(6): p. A1149-A1157.
117. Berning, T., D.M. Lu, and N. Djilali, *Three-dimensional computational analysis of transport phenomena in a PEM fuel cell.* Journal of Power Sources, 2002. **106**(1-2): p. 284-294.
118. Wu, H., X. Li, and P. Berg, *On the modeling of water transport in polymer electrolyte membrane fuel cells.* Electrochimica Acta, 2009. **54**(27): p. 6913-6927.
119. Weber, A.Z. and J. Newman. *Modeling gas-phase transport in polymer-electrolyte fuel cells*. 2006. Los Angeles, United States: Electrochemical Society Inc., Pennington, NJ 08534-2896, United States.
120. Owejan, J.P., et al., *Water Transport Mechanisms in PEMFC Gas Diffusion Layers.* Journal of the Electrochemical Society, 2010. **157**(10): p. B1456-B1464.
121. Sinha, P.K. and C.-Y. Wang, *Liquid water transport in a mixed-wet gas diffusion layer of a polymer electrolyte fuel cell.* Chemical Engineering Science, 2008. **63**(4): p. 1081-1091.
122. Scott, K. and M. Mamlouk, *A cell voltage equation for an intermediate temperature proton exchange membrane fuel cell.* International Journal of Hydrogen Energy, 2009. **34**(22): p. 9195-9202.
123. Davey, J., et al., *Water Dynamics in a PEM Fuel Cell: Effect of Current and Humidity Transients.* ECS Transactions, 2008. **16**(2): p. 329-340.
124. Liu, J., et al., *Transport phenomena within the porous cathode for a PEM fuel cell.* Journal of Power Sources, 2010. **In Press, Accepted Manuscript**.